

# Experimental Investigation of a Laminar Separation Bubble Subjected to Wing Structural Motion



Adrián Grille Guerra



# Experimental Investigation of a Laminar Separation Bubble Subjected to Wing Structural Motion

by

Adrián Grille Guerra

to obtain the degree of Master of Science  
at the Delft University of Technology,  
to be defended publicly on Tuesday April 26, 2022 at 4:00 PM.

Student number: 4924649  
Project duration: September 1, 2020 – April 26, 2022  
Thesis committee: Dr. ir. B. W. van Oudheusden, TU Delft, chair of assessment committee  
Dr. ir. J. Little, The University of Arizona  
Ir. C. Mertens, TU Delft  
Dr. ir. F. Avallone, TU Delft

An electronic version of this thesis is available at <http://repository.tudelft.nl/>.



# Preface

This document puts an end to the most exciting adventure of my life, which involved four different countries with totally different lifestyles in a period of three and a half years. On this page, I welcome the reader to learn a bit about the people that made it possible and shared the thrilling adventure.

The journey started in September 2018, when I joined TU Delft to pursue an MSc in Aerospace Engineering. During that first year in Delft, I must highlight the importance of *Javier Lobato Pérez*. It was a big pleasure working with you and learning so much about how to write a decent report. I hope this document proves I was paying attention. More importantly, thanks for showing me that an outstanding engineer may come from anywhere.

I have to admit that I spend many nights dreaming about working in Formula 1 when I suddenly wake up and realize I made this dream come true during my internship. Thanks to everyone in the Renault F1 Team for making the experience way better than it was in my dreams. Among all of them, the giant figure of Dr. *Robbie Stevens* deserves special treatment. You changed my life forever with a single decision. I am only looking forward to the time we can work together again. I would probably need more than one life to pay you back, but please be sure I will make everything I can in this one.

The end to this dream hit hard in the shape of a pandemic. That brought me back home, where I regained the energy I needed for my little one-year trip to Tucson. From my stay there, I would like to thank *David Borgmann* and Dr. *Ashish Singh* for their continuous support and for making me feel like being at home from the very first day. Regarding the people who contributed most to this work, a special thank goes to *Michael Meersman* for building the beautiful wind tunnel model. I also wish to thank Dr. *S. Craig* for the use of the infrared camera and the AFOSR for their generous support. A very special thank goes to Dr. *Jesse Little*, the person who gave me this amazing opportunity. Thanks for your trust, your patience and for giving me the flexibility I always wanted.

From the Delft side of this project, I would like to thank my daily supervisor, *Christoph Mertens*. Thanks for your valuable pieces of advice, for encouraging me to keep pushing when things were not going as planned in the tunnel and for being so close even from across the ocean. I would also like to take the chance and state my most profound admiration for the work and figure of my supervisor, Dr.ir. *B.W. van Oudheusden*. What a bright light to guide the path of a young aerodynamicist.

This adventure would not have been possible without the support and understanding of my friends and family. Thanks for encouraging me to search and travel for the best opportunities but at the same time begging me to come back home. Your love means everything to me. Bridging the gap between friends and family, I would like to thank *Dolores Lestón Cambeiro* for the help with the cover for the thesis.

Grazas a *Luz*, por camiña-la vida ao meu carón. Paseniño, cun sorriso nos beizos e sempre collidos da man.

*Adicado á memoria de Santiago Pena Boado*

*Adrián Grille Guerra*  
*Delft, March 2022*



# Abstract

Unmanned aerial vehicles have proliferated in the last few decades, with applications that include military, commercial and recreational. Their size and typical flight velocities are characterized by moderate Reynolds numbers  $O(10^4 - 10^5)$ . For such conditions, boundary layers can remain laminar and therefore are highly susceptible to separation and the generation of laminar separation bubbles (LSBs), when compared to more conventional aircraft. Extensive research has been done to study the influence of Reynolds number, angle of attack, sweep angle or freestream turbulence level on the nature of LSBs. However, the study of LSBs subject to unsteadiness is rather limited. This is especially relevant for small aircraft that typically fly in gusty environments such as cities. The problem is aggravated by the recent shift toward composite manufacturing, which allows more efficient high-aspect-ratio configurations, but that deform considerably more when subjected to unsteady loads.

The LSB that forms on the suction side of a modified NACA 64<sub>3</sub> – 618 airfoil at a chord-based Reynolds number of  $Re = 200k$  is studied in a series of wind tunnel experiments conducted at The University of Arizona. Three different flow measurement techniques are considered in the experiments to identify the bubble: surface pressure measurements, Particle Image Velocimetry and Infrared Thermography. The capabilities of the three techniques are first explored in a static characterization of the LSB over a range of angles of attack. For the conditions tested, excellent agreement between the techniques is obtained, showing an upstream shift of the bubble with increasing incidence. For the study of static LSBs, the infrared approach is superior, given its higher spatial resolution and experimental simplicity.

The complexity is then increased to study the influence of aerodynamic unsteadiness on the bubble. For this purpose, two different types of structural motion are imposed on the wind tunnel model. A first experiment considers a pitching-type motion, with reduced frequencies up to  $k = 0.25$ . While surface pressure measurements and PIV are not heavily affected by the change in experimental conditions, the infrared approach becomes limited by the thermal response of the surface. To overcome this limitation, an extension of the recently proposed Differential Infrared Thermography (DIT) method is considered. Even so, the unsteady behaviour of the bubble can be only partially detected with this method. All-three techniques considered indicate a hysteresis in bubble location between the pitch up and pitch down parts of the motion, caused by the effect of the aerodynamic unsteadiness on the adverse pressure gradient.

The second type of structural motion studied consists of a sinusoidal plunge, with an amplitude of  $h = 6\%$  of the airfoil chord and a reduced frequency of  $k = 0.67$ . The surface pressure measurements and PIV still capture a hysteresis in bubble location along the cycle, expressed in terms of the effective angle of attack induced by the plunging motion. However, due to the increased frequency of the motion, the thermal response of the surface reduces and the infrared approach fails to detect the unsteady bubble.



# Contents

<b>List of Figures</b>	<b>ix</b>
<b>List of Tables</b>	<b>xiii</b>
<b>Nomenclature</b>	<b>xv</b>
<b>1 Introduction</b>	<b>1</b>
1.1 Research objective and Outline . . . . .	4
<b>2 Unsteady Laminar Separation Bubbles</b>	<b>7</b>
2.1 Linear unsteady aerodynamics: Theodorsen's theory . . . . .	7
2.2 Experimental measurements of unsteady LSBs . . . . .	9
<b>3 Infrared Thermography for Unsteady Boundary Layer Diagnostics</b>	<b>11</b>
3.1 Convective heat transfer and the Reynolds analogy . . . . .	11
3.2 Radiative heat transfer and infrared scanners . . . . .	13
3.3 Unsteady BL transition detection using IT . . . . .	15
<b>4 Experimental Setup</b>	<b>19</b>
4.1 Wind tunnel facility . . . . .	19
4.2 Wing section . . . . .	20
4.2.1 Pitching mechanism . . . . .	20
4.2.2 Plunging mechanism . . . . .	21
4.3 Surface pressure measurements . . . . .	23
4.4 Particle Image Velocimetry . . . . .	23
4.5 Infrared Thermography . . . . .	24
<b>5 Methodology</b>	<b>27</b>
5.1 LSB detection from surface pressure taps . . . . .	27
5.2 LSB detection from PIV . . . . .	28
5.3 LSB detection from IT . . . . .	30
5.3.1 Marker tracking and image dewarping . . . . .	30
5.3.2 LSB location from temperature distributions. . . . .	32
5.3.3 Differential Infrared Thermography approach . . . . .	35
5.3.4 Thermal response of an unsteady airfoil . . . . .	37
<b>6 Results</b>	<b>45</b>
6.1 Static LSB characterization . . . . .	45
6.1.1 Surface pressure measurements. . . . .	46
6.1.2 Particle Image Velocimetry. . . . .	47
6.1.3 Infrared Thermography . . . . .	49
6.1.4 Comparison of experimental techniques . . . . .	50
6.2 Pitching investigation . . . . .	51
6.2.1 Surface pressure measurements. . . . .	52
6.2.2 Phase-averaged PIV measurements . . . . .	53
6.2.3 Infrared Thermography . . . . .	54
6.2.4 Comparison of experimental techniques . . . . .	60

---

6.3	Plunging investigation . . . . .	62
6.3.1	Surface pressure measurements. . . . .	62
6.3.2	Phase-averaged PIV measurements. . . . .	64
6.3.3	Differential Infrared Thermography. . . . .	67
<b>7</b>	<b>Conclusion</b>	<b>71</b>
7.1	Static characterization of a LSB . . . . .	72
7.2	Unsteady behaviour of a LSB subjected to wing structural motion. . . . .	72
7.3	Recommendations for future work . . . . .	73
	<b>Bibliography</b>	<b>75</b>

# List of Figures

1.1	(left) Sketch of a LSB forming over an airfoil. Reproduced from Uranga et al. [74] (right) Aeromot AMT-200 Super Ximango motor glider. . . . .	1
1.2	Time-averaged flowfield around a SD7003 airfoil at $\alpha = 4^\circ$ . LSB characteristic locations indicated by red dots. Reproduced from Nati et al. [52]. . . . .	2
1.3	(left) Static pressure coefficient distribution over a NACA 0018 airfoil, for $Re = 160k$ and $\alpha = 10^\circ$ . Reproduced from Gerakopoulos et al. [24]. (right) Temperature fields over a NACA 0015 hydrofoil at two different angles of attack, obtained using temperature-sensitive paints. Reproduced from Miozzi et al. [50]. . . . .	3
2.1	(left) Oscillatory motion contributions in Theodorsen's theory. Pitching (top) and plunging (bottom). Reproduced from Leishman [44]. (right) Circulatory part of the unsteady lift response for a sinusoidal variation in $\alpha$ . Reproduced from [44]. . . . .	8
2.2	LSB characteristic locations for static (dotted line) and unsteady pitching (dashed line) SD7003 airfoil. (a) Laminar separation location. (b) Transition location. Reproduced from Nati et al. [52]. . . . .	10
3.1	Theoretical trend and experimental measurements of the skin friction coefficient $C_f$ over a flat plate at zero incidence. Reproduced from Schlichting and Gersten [67]. . .	12
3.2	(left) Sketch illustrating the absorption, reflection and transmission of irradiation by a body. Reproduced from Astarita and Carlomagno [3]. (right) Atmospheric transmittance in the infrared band. Reproduced from [3]. . . . .	14
3.3	Instantaneous infrared images A and B, with $\alpha_A > \alpha_B$ . Correspondent DIT image on the right. Results reproduced from Raffel et al. [61]. . . . .	16
3.4	Effect of image time separation on the transition location measured with DIT. (left) DIT signal obtained with different time separations. (right) Signal strength and delay normalized with the time separation used in the experiments by Richter et al. [65]. Results reproduced from Gardner et al. [18]. . . . .	17
4.1	Plan view of the Arizona Low Speed Wind Tunnel. Reproduced from Borgmann et al. [7]. . . . .	20
4.2	Distribution of pressure taps at mid-span and pressure transducer at 65% of the chord.	20
4.3	Mechanisms employed to impose the desired structural motions on the wing. (left) Pitching. (right) Plunging. . . . .	21
4.4	Wing's vertical position and effective angle of attack through the plunging cycle, in terms of the phase angle of the motion. . . . .	22
4.5	Sketch of the experimental setup in the Arizona Low-Speed Wind Tunnel. 1- Halogen lamp; 2- Infrared camera; 3- Ceiling aperture for infrared access; 4- PIV camera; 5- Laser head; 6- Mid-span pressure taps; 7- Region of interest for IT; 8a- Plunging mechanism; 8b- Pitching mechanism. . . . .	24
4.6	Infrared Thermography setup in the Arizona Low-Speed Wind Tunnel. . . . .	25
5.1	Static pressure coefficient distribution for the static wing at $\alpha = 5^\circ$ . Linear fits illustrating the methodology to detect the LSB characteristic locations. . . . .	28

5.2	Contours of time-averaged velocity magnitude for the static wing at $\alpha = 2^\circ$ . (a) With added streamlines. (b) With dividing streamline included. . . . .	29
5.3	(a) BL characteristics for the static wing at $\alpha = 2^\circ$ . (b) Contours of time-averaged velocity magnitude with streamwise velocity BL profiles for the static wing at $\alpha = 2^\circ$ . . .	30
5.4	Infrared images containing the detected markers for image dewarping. (a) Raw image. (b) Transformed image, showing the rectangular region of interest. . . . .	31
5.5	Wing position along the plunging cycle obtained from the location of a fiducial marker during 1 s of acquisition. . . . .	32
5.6	Heat transfer processes considered for the thermal modelling of an unsteady airfoil. .	33
5.7	Evolution of skin friction, Stanton number and BL shape factor in the presence of a LSB. Results adapted from Spalart and Strelets [70]. . . . .	34
5.8	Contours of time-averaged infrared intensity (top) and spanwise-averaged infrared intensity and intensity gradient distributions along the chord (bottom) for the static wing at $\alpha = 2^\circ$ . . . . .	35
5.9	Contours of the difference in infrared intensity between $\alpha_1 = 1.5^\circ$ and $\alpha_2 = 2.5^\circ$ (top) and spanwise-averaged infrared intensity and DIT distributions along the chord (bottom). . . . .	36
5.10	Skin friction coefficient distributions on the suction side of a DSA-9A airfoil at two different incidence angles. Results reproduced from Gardner et al. [18]. . . . .	38
5.11	Distributions considered for the unsteady thermal model, following DLR results from Gardner et al. [18] and experiments conducted at UA. (a) Surface temperature. (b) Convective heat transfer coefficient. . . . .	38
5.12	<i>DIT signal</i> obtained from the thermal model, for both the DLR and UA situations. (a) For a simulation time of $t = 10^{-2}$ s. (b) For a simulation time of $t = 10^{-1}$ s. The dashed blue lines represent the thermal sensitivity of typical modern infrared cameras. . . . .	40
5.13	<i>DIT signal</i> obtained from the thermal model for the case of a LSB, for pitch up and pitch down conditions. (a) For a simulation time of $t = 10^{-2}$ s. (b) For a simulation time of $t = 10^{-1}$ s. The dashed blue lines represent the thermal sensitivity of typical modern infrared cameras. . . . .	41
5.14	Comparison of the non-dimensional group $FoBi$ between the experiments of Richter et al. [65], Wolf et al. [84] and the ones at UA. . . . .	43
6.1	(a) $c_p$ distributions for the static wing at $\alpha = 0^\circ, 2^\circ, 4^\circ$ and $6^\circ$ . (b) Frequency-premultiplied non-dimensional Power Spectral Density (PSD) of pressure fluctuations at $x/c = 0.65$ at the same angles of attack. . . . .	46
6.2	LSB characteristic locations estimated from $c_p$ distributions, for the static wing at (a) $\alpha = -5^\circ, 0^\circ$ and $7^\circ$ . (b) $-5^\circ \leq \alpha \leq 7^\circ$ . . . . .	47
6.3	Contours of time-averaged velocity magnitude from PIV measurements, for the static wing at (a) $\alpha = 0^\circ$ and (b) $\alpha = 7^\circ$ . . . . .	48
6.4	(a) Evolution of the BL shape factor inside the LSB, for the static wing at $\alpha = -5^\circ, 0^\circ$ and $7^\circ$ . (b) LSB characteristic locations extracted from the PIV measurements. . . . .	48
6.5	LSB characteristic locations estimated from time- and spanwise-averaged infrared intensity distributions, for the static wing at (a) $\alpha = -5^\circ, 0^\circ$ and $7^\circ$ . (b) $-5^\circ \leq \alpha \leq 7^\circ$ . . . . .	49
6.6	(a) LSB characteristic locations estimated from the static DIT method, for the static wing at $\alpha = -4.5^\circ, 0.5^\circ$ and $6.5^\circ$ . (b) Comparison between the LSB characteristic locations measured with the static IT and DIT approaches. . . . .	50
6.7	Comparison of the LSB characteristic locations obtained for the static wing using three different flow measurement techniques. . . . .	51
6.8	Unsteady lift coefficient for the pitching wing, with: (a) $k = 0.05$ and (b) $k = 0.15$ . . . . .	52

6.9	Phase-averaged $c_p$ distributions for the pitching wing at $\alpha = 2^\circ$ , both for pitch up and pitch down, with: (a) $k = 0.05$ and (b) $k = 0.15$ . . . . .	53
6.10	Phase-averaged velocity magnitude for the pitching wing at $\alpha = 2^\circ$ , with $k = 0.05$ , during (a) pitch up (b) pitch down. . . . .	54
6.11	Phase-averaged velocity magnitude for the pitching wing at $\alpha = 2^\circ$ , with $k = 0.15$ , during (a) pitch up (b) pitch down. . . . .	54
6.12	(a) DIT curves at $\alpha = 2^\circ$ for the quasi-steady pitching wing, using various separations between infrared frames, $\Delta\alpha$ . (b) LSB characteristic locations for the quasi-steady pitching wing, obtained from the static IT and DIT methods. . . . .	55
6.13	DIT curves for the pitching wing at $\alpha = 2^\circ$ , with $k = 0.05$ , during (a) pitch up (b) pitch down. . . . .	56
6.14	(a) Surface temperature distributions and transition location before the start of the pitching motion. (b) Unsteady transition location for the pitching wing, obtained from DIT, with $k = 0.05$ , compared to static and quasi-steady situations. . . . .	57
6.15	DIT curves for the pitching wing at $\alpha = 2^\circ$ , for $k = 0.15$ , during (a) pitch up (b) pitch down. . . . .	58
6.16	Unsteady transition location for the pitching wing, obtained from DIT, with $k = 0.15$ , compared to static and quasi-steady situations. . . . .	59
6.17	DIT curves for the pitching wing at $\alpha = 2^\circ$ , for various motion reduced frequencies and using a time separation between DIT frames of $\Delta\alpha = \pm 1^\circ$ , during (a) pitch up (b) pitch down. . . . .	59
6.18	Unsteady transition location for the pitching wing, obtained from DIT, for every reduced frequency measured, both for pitch up and pitch down. . . . .	60
6.19	Hysteresis in transition location with respect to the static value obtained from the three experimental techniques for various pitching motion reduced frequencies. Theoretical prediction extracted from linear unsteady theory included for further comparison. . . . .	61
6.20	(a) Lift coefficient evolution along the plunging cycle, written in terms of the effective angle of attack of the wing. Comparison between experiments and Theodorsen's theory. (b) Phase-averaged power spectrum of the CWT of pressure fluctuations captured with the high-bandwidth pressure transducer at $x/c = 0.65$ . . . . .	63
6.21	(a) Phase-averaged $c_p$ distributions over the suction side of the wing at four phases along the sinusoidal plunging cycle. (b) LSB characteristic locations along the plunging cycle, extracted from the phase-averaged $c_p$ distributions, compared to the static situation. . . . .	64
6.22	Contours of phase-averaged velocity magnitude with streamwise velocity boundary layer profiles (a), and visualization of coherent structures using the $\Gamma_2$ vortex identification criterion (b), for four phases along the plunging cycle. . . . .	65
6.23	LSB characteristic locations along the sinusoidal plunging cycle extracted from phase-averaged PIV measurements, compared with the static characterization. . . . .	66
6.24	LSB characteristic locations along the sinusoidal plunging cycle extracted from phase-averaged PIV measurements, $c_p$ distributions and theoretical prediction from linear unsteady theory. . . . .	66
6.25	Phase-averaged infrared intensity distributions for the plunging wing at four phases along the cycle. . . . .	67
6.26	DIT curves for the plunging wing at: (a) $\phi/\pi = 0$ , (b) $\phi/\pi = 0.5$ , (c) $\phi/\pi = 1$ and (d) $\phi/\pi = 1.5$ . . . . .	68



# List of Tables

4.1	Pitching experiment test matrix . . . . .	21
4.2	Static pressure taps parameters . . . . .	23
4.3	PIV parameters . . . . .	24
4.4	IT parameters . . . . .	26
5.1	Simulation parameters from Gardner et al. [18] . . . . .	37



# Nomenclature

## Latin Symbols

$a$	Pitch axis location relative to mid-chord
$Bi$	Biot number
$c$	Airfoil chord length
$C(k)$	Theodorsen's function
$C_1, C_2$	Auxiliary constants
$C_f$	Skin friction coefficient
$c_l$	Lift coefficient
$C_m$	Heat capacity of the material
$C_p$	Fluid's heat capacity at constant pressure
$c_p$	Static pressure coefficient
$f$	Frequency
$Fo$	Fourier number
$H$	Boundary layer shape factor
$h$	Plunging motion non-dimensional amplitude
$h_c$	Characteristic change of convective heat transfer
$h_s$	Convective heat transfer coefficient
$H_v^{(2)}$	Hankel function
$i$	Imaginary unit
$k$	Reduced frequency
$k_m$	Thermal conductivity of the material
$L$	Thickness of perfect insulator
$L_c$	Characteristic length scale
$N$	Critical $N$ -factor
$q_\infty$	Freestream dynamic pressure
$q_{cond}$	Conductive heat flux
$q_{conv}$	Convective heat flux

$q_{irr}$	Heat flux from the external irradiative source
$q_{rad}$	Radiative heat flux
$Re$	Reynolds number
$St$	Stanton number
$T$	Temperature
$t$	Time
$T_c$	Characteristic temperature
$t_c$	Characteristic time scale
$T_s$	Surface temperature
$T_\infty$	Freestream temperature
$Tu$	Turbulence intensity
$u$	Tangential component of velocity
$u_e$	Edge velocity
$U_\infty$	Freestream speed
$x$	Streamwise coordinate
$y$	Wall-normal coordinate
$y_w$	Wing's vertical position
$z$	Spanwise coordinate
$\bar{U}$	Velocity magnitude

### **Greek Symbols**

$\alpha$	Angle of attack
$\alpha_1, \alpha_2$	Auxiliary angles of attack
$\alpha_m$	Thermal diffusivity
$\alpha_r$	Absorptivity coefficient
$\alpha_{eff}$	Effective angle of attack
$\alpha_{nom}$	Nominal angle of attack
$\delta$	Boundary layer thickness
$\delta^*$	Boundary layer displacement thickness
$\epsilon$	Emissivity coefficient
$\Gamma_2$	Vortex identification scheme

$\mu$	Dynamic viscosity of the fluid
$\phi$	Phase angle of the plunging motion
$\rho$	Density of the fluid
$\rho_m$	Density of the material
$\rho_r$	Reflectivity coefficient
$\sigma$	Stefan-Boltzmann constant
$\tau_r$	Transmissivity coefficient
$\tau_w$	Wall shear stress
$\theta, \theta'$	Auxiliary integration variables
$\theta^*$	Boundary layer momentum thickness

### Abbreviations

AFC	Active Flow Control
AFOSR	Air Force Office of Scientific Research
ALSWT	Arizona Low-Speed Wind Tunnel
BL	Boundary Layer
CFD	Computational Fluid Dynamics
CWT	Continuous Wavelet Transform
DIT	Differential Infrared Thermography
DLR	German Aerospace Center
DNS	Direct Numerical Simulation
FPA	Focal Plane Array
IT	Infrared Thermography
LSB	Laminar Separation Bubble
LWIR	Longwave Infrared
MWIR	Midwave Infrared
NETD	Noise Equivalent Temperature Difference
PIV	Particle Image Velocimetry
PSD	Power Spectral Density
UA	The University of Arizona
WT	Wind Tunnel



# 1

## Introduction

In a continuous search for energetic efficiency, the aeronautical industry has recently shifted towards the use of composite materials wherever possible. This search, mainly driven by the limited availability and subsequent costs of fuel, creates some of the most beautiful engineering challenges. From an aerodynamic perspective, the use of composites (lighter than conventional materials) does not only allow to reduce lift and therefore drag, but also offers the possibility of using more efficient high-aspect-ratio wings. When subjected to aerodynamic loading, these will deform considerably more than traditional lower-aspect-ratio structures manufactured with conventional materials. This fact is clearly visible in modern aircraft, as for example the Boeing 787 *Dreamliner*. In a gusty environment, the unsteady aerodynamic loading will have a greater effect on these more flexible wings. This can reduce the aerodynamic performance, diminish the capability of maintaining vehicle control and ultimately cause structural failure. While the latter two are out of the scope of this thesis, understating the effect that structural motion has on the aerodynamic performance of a wing is a key part of the project.

In general, gusts have more dramatic effects on smaller and slower aerial vehicles. Besides, these are more likely closer to the earth's surface, which is the typical flight environment of small aerodynamic devices. The size and flight velocity may be characterized using the chord-based Reynolds number,  $Re$ . In a moderate  $Re$  regime,  $O(10^4 - 10^5)$ , the boundary layer (BL) developing on the suction side of an airfoil often remains laminar beyond the point of minimum pressure. In the adverse pressure gradient region, the laminar BL can separate, forming a shear layer. Under certain conditions, a laminar-to-turbulent transition process may occur in the separated shear layer and cause the reattachment of a turbulent BL. This flow feature, enclosed by the shear layer, is called *laminar separation bubble* (LSB). This description is reproduced in Fig. 1.1 (left).

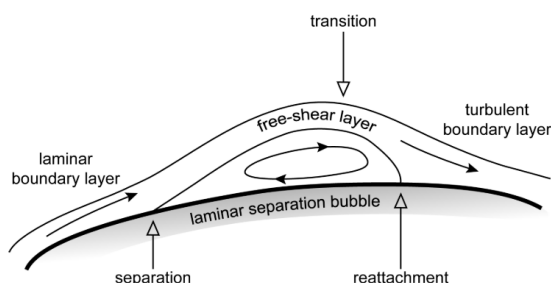


Figure 1.1: (left) Sketch of a LSB forming over an airfoil. Reproduced from Uranga et al. [74] (right) Aeromot AMT-200 Super Ximango motor glider.

LSBs are therefore often present in a variety of applications such as unmanned aerial vehicles,

wind turbines or gliders. A meaningful example for this thesis is the Ximango motor glider shown in Fig. 1.1 (right), as the airfoil considered in the current investigation is extracted from this aircraft. Gaster [23] and Horton [31] were among the first to study LSBs, investigating the effect of pressure gradient and Reynolds number on the nature and size of the bubble. They defined the characteristic features of LSBs, including separation of the laminar boundary layer due to the adverse pressure gradient, transition to turbulence in the separated shear layer that encloses the bubble and reattachment of a turbulent boundary layer. Early studies also tried to classify LSBs based on their size relative to BL parameters (Owen and Klanfer [55]) or effect on the static pressure distribution (Tani [72]).

Advances in experiments and computations have made it possible to study the aerodynamic problem in detail. The transition process in the separated shear layer is of particular interest for both basic and applied research purposes. The experiments of Watmuff [80] and Lang et al. [42], among others, have shown that amplification of the Kelvin-Helmholtz instability in the shear layer is a common feature of LSBs, leading to the roll-up and shedding of spanwise coherent vortices at the rear part of the bubble. Simulations from Visbal et al. [76], among others, showed that this effect compensates for the adverse pressure gradient, leading to a highly unsteady reattachment process associated with a turbulent boundary layer. Under particular circumstances, such as high turbulence levels or strong three-dimensionality, other instabilities can govern the transition process (Kurelek et al. [41]) but are out of the scope of the present investigation.

Extensive research has been done to study the influence of Reynolds number (Burgmann and Schöder [11]), angle of attack,  $\alpha$  (Yarusevych et al. [87]), sweep angle (Hetsch and Rist [29] & Hosseinverdi and Fasel [32]), and freestream turbulence level (Balzer and Fasel [4] & Hosseinverdi and Fasel [34, 36, 33]) on the topology of LSBs. An increase in  $Re$ , angle of attack or freestream turbulence typically causes an upstream movement and size reduction of the bubble.

Over the years, various flow measurement techniques have been considered to identify the mean topology of LSBs in experiments. Some measure the velocity field in the region of the bubble and others analyze the effect of the LSB at the wall, in terms of static pressure, skin friction or convective heat transfer. The most popular technique for velocity measurements is nowadays Particle Image Velocimetry (PIV), and many studies have used it to detect LSBs and investigate the transition process occurring in the separated shear layer. An example of a PIV measurement in the presence of a LSB is shown in Fig. 1.2. This result, reproduced from Nati et al. [52], shows the LSB developing on the suction side of a SD7003 airfoil at  $\alpha = 4^\circ$ . The depicted streamlines illustrate the presence of a LSB on the rear part of the airfoil and show a recirculation region prior to the turbulent BL reattachment.

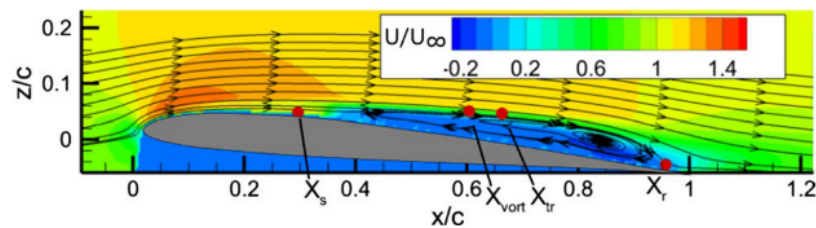


Figure 1.2: Time-averaged flowfield around a SD7003 airfoil at  $\alpha = 4^\circ$ . LSB characteristic locations indicated by red dots. Reproduced from Nati et al. [52].

Although PIV provides a complete description of the LSB, the technique typically suffers from higher uncertainty close to the walls. The laser sheet used to illuminate the seeding particles reflects at the surface corrupting the measurements. This makes it difficult to detect the exact laminar separation and turbulent reattachment locations. To overcome this limitation, flow measurement techniques that provide direct wall measurements may be used. The most common example, widely

present in experimental aerodynamics, is the use of static pressure taps at the wall. An example of a static pressure coefficient ( $c_p$ ) distribution for the case of a LSB is shown in Fig. 1.3 (left). This result, reproduced from Gerakopoulos et al. [24], shows the  $c_p$  distribution over a NACA 0018 airfoil at  $\alpha = 10^\circ$ , for  $Re = 160k$ . The presence of the LSB is indicated by the pressure plateau that forms after flow separation, followed by a region of fast pressure recovery due to flow reattachment (O’Meara and Mueller [53]).

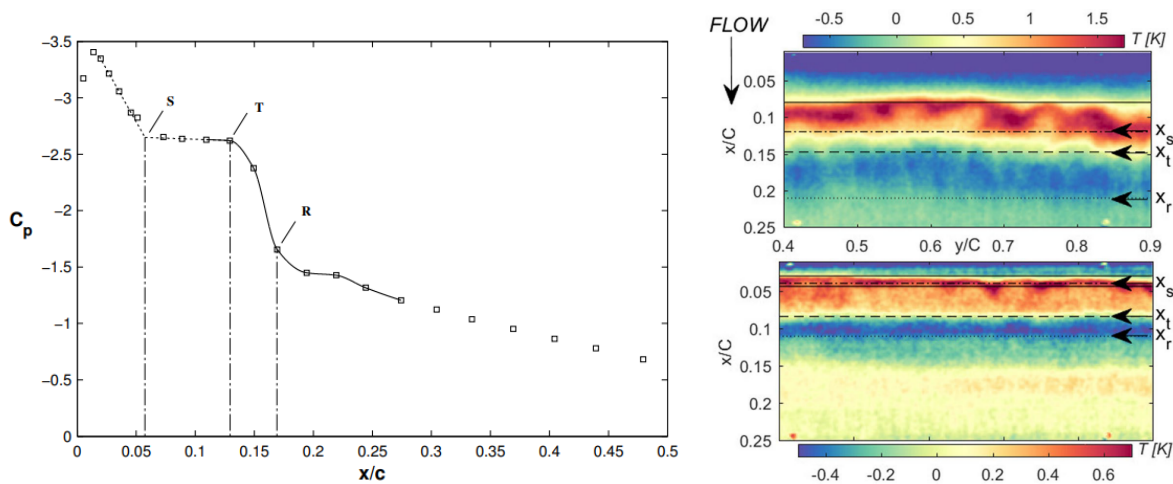


Figure 1.3: (left) Static pressure coefficient distribution over a NACA 0018 airfoil, for  $Re = 160k$  and  $\alpha = 10^\circ$ . Reproduced from Gerakopoulos et al. [24]. (right) Temperature fields over a NACA 0015 hydrofoil at two different angles of attack, obtained using temperature-sensitive paints. Reproduced from Miozzi et al. [50].

Even if the bubble has a strong impact on the pressure distribution, the accurate location of it is strongly limited by the spatial resolution of the taps. A similar issue is found when using hot-film anemometry, successfully applied by Rudmin et al. [66] to detect the LSB forming over a NACA 0012 airfoil. The problem can be avoided by switching to optical techniques. These can be used to measure different BL parameters, such as surface pressure, skin friction or surface temperature. Fujisawa et al. [16] and Zhong [88] considered shear-sensitive liquid crystals to perform quantitative measurements of the wall shear stress on a NACA 0018 and 66(1)-012 respectively, visualizing the locations of laminar separation and turbulent reattachment. Miozzi et al. [50] used temperature-sensitive paints to study the LSB developing on the suction side of a NACA 0015 hydrofoil. From the temperature measurements, skin-friction vector fields were extracted by means of an optical-flow-based algorithm. An example of the temperature fields measured for the hydrofoil at two different angles of attack is given in Fig. 1.3 (right). Although these techniques can be used to detect regions of separated flow, they involve a complex model preparation before every experiment.

A non-intrusive optical technique has gained recent attention in subsonic aerodynamic testing. This is Infrared Thermography (IT), which uses a camera sensitive in the infrared band of the electromagnetic spectrum to measure surface temperature. This can be linked to the convective heat transfer between the surface and the flow thus providing information about the BL state. Some studies have already used IT to detect LSBs. Ricci and Montelpare [63] employed this technique to detect the bubble on a Eppler-387 airfoil. They estimated convective heat transfer from the measured temperatures using a numerical approach. More recently, Wynnychuk and Yarusevych [86] detected the LSB over a NACA 0018 solely from temperature distributions, showing good agreement with PIV results.

Not all of the flow measurement techniques mentioned so far are suitable for unsteady situations. Some lack the temporal resolution and for others there is simply not a lot of research conducted yet. This project tackles the experimental investigation of an unsteady LSB using some of

these techniques. In the case of IT, recent advances in infrared cameras have increased their temporal resolution sharply, thus making it possible to consider the technique for unsteady subsonic investigations.

### 1.1. Research objective and Outline

This research project is a collaboration between TU Delft and The University of Arizona. All the experimental work discussed in the thesis was conducted at The University of Arizona. This was part of a broader project supported by the Air Force Office of Scientific Research (AFOSR), with Dr. Gregg Abate serving as the program manager. The goal of the project is to study the effects of wing structural motion on a laminar airfoil in a low Reynolds number environment. In the context of this thesis, a wing section undergoing structural motion is studied in a wind tunnel (WT) experiment, and the conditions are such that a LSB forms on the wing surface. The bubble is studied in detail considering various flow measurement techniques. This sets the research objective of the thesis:

“Investigate the strengths and weaknesses of three different flow measurement techniques—surface pressure measurements, Particle Image Velocimetry and Infrared Thermography—to detect the location of an unsteady Laminar Separation Bubble”.

The study of LSBs subjected to unsteadiness is rather limited. In chapter 2, some results extracted from the literature will be discussed. Also, some results from linear unsteady airfoil theory will be introduced. These, written in terms of unsteady lift response, will serve as a reference for the experimental surface pressure measurements.

As IT constitutes the novel approach towards unsteady LSB identification, the technique will be explained in greater detail in chapter 3. This involves the description of the heat transfer process at the surface and finding a relation between surface temperature and the BL state. While this is generally described for static conditions, the approach will be extended to an unsteady situation, discussing some existing results from the literature.

The experimental setup considered in the WT campaigns at The University of Arizona will be discussed in chapter 4. This will include a description of the WT facility, the wing section used and its internal instrumentation, and also an explanation of the flow measurement techniques considered in the experiments. The mechanisms used to impose the structural motion to the wing will be illustrated as this constitutes an important part of the project.

Chapter 5 will be dedicated to discussing the methodology employed to detect the LSB from the experimental measurements. This includes the methodology for the surface pressure taps, PIV and IT. For IT, the approach for a static situation will be first discussed, as this is in agreement with some existing publications. Then, a novel approach will be presented to study the case of an unsteady LSB. This will be accompanied by the implementation of an analytical thermal model that simulates the unsteady heat transfer process at the wing surface. This will be used to characterize the unsteady situation and later compared to the actual experimental results.

The first experimental investigation conducted in this project consisted of a static characterization of a LSB using the three techniques mentioned above. Then, two different types of structural motion were imposed to the wing section. The simpler case was a pitching motion (pure  $\alpha$  change). The frequency of this motion was changed to study from quasi-steady situations to fully unsteady ones. Then, the complexity was increased to study a plunging condition. The experimental results obtained from the three investigations (static, pitching and plunging) will be discussed in chapter 6. Finally, the conclusions derived from this investigation will be discussed in chapter 7. This will include a review of the research objective and some recommendations for future work.

The research project conducted at The University of Arizona combines flight tests, wind tunnel experiments and high-fidelity numerical simulations. Only the wind tunnel part of the project will

be discussed here. The comparison between wind tunnel experiments and the numerical simulations can be found in Grille Guerra et al. [27, 28]. One of the topics of the research project is to explore the use of Active Flow Control (AFC) combined with the unsteady regime. This part of the project is also excluded from the thesis document. The interested reader is referred to Hosseinverdi et al. [37] for a comparison between experiments and simulations on the use of AFC for a static situation.



# 2

## Unsteady Laminar Separation Bubbles

Unsteady aerodynamic effects appear in various flow situations, such as gust encounters, manoeuvres or transient flows. To understand the effect of the aerodynamic unsteadiness on a full aircraft wing or helicopter rotor, the problem can be first simplified by studying the case of a two-dimensional airfoil. The challenging mathematical modelling of unsteady airfoil behaviour received great attention since the 20th century. As an extension of steady thin-airfoil theory, authors like Von Karman and Sears [79] or Theodorsen [73] studied the airfoil response to gusting or structural motion. The presence of a LSB violates the modeling assumption of inviscid flow, but the results from these methods can still be compared to the experimental results in this case. A review of Theodorsen's theory is given in §2.1, focusing on the unsteady lift response of an airfoil subjected to structural motion.

More recent research on the effects of aerodynamic unsteadiness does incorporate the role of viscosity. A lot of effort has been dedicated to investigating phenomena such as unsteady BL transition (Gardner et al. [20]) or dynamic stall (McCroskey [47]). Both of these can still occur under the presence of a LSB, but the study of this topic is rather limited. Some existing results are reviewed in §2.2, as these constitute the closest link to the investigation conducted in this thesis.

### 2.1. Linear unsteady aerodynamics: Theodorsen's theory

Theodorsen's theory gives a solution to the unsteady aerodynamic loads on a two-dimensional harmonically oscillated airfoil in inviscid, incompressible flow. A vortex sheet is used to represent the airfoil and its wake. By imposing the Kutta condition at the trailing edge and circulation conservation, the vortex model gives the bound circulation under harmonic forcing conditions. The solution represents a transfer function between the forcing (structural motion) and the aerodynamic response (lift and pitching moment). The oscillatory motion of the airfoil can include both plunging and pitching contributions. These are represented in Fig. 2.1(left), as reproduced from Leishman [44]. A pitching motion includes contributions from  $\alpha$  variations and pitch rate ( $\dot{\alpha}$ ), whereas a plunging motion induces  $\alpha$  changes and is characterized by the motion amplitude  $h$ , typically made non-dimensional using the airfoil chord length  $c$ .

For an oscillatory motion that includes both pitching and plunging contributions, in a flow of steady velocity  $U_\infty$ , the unsteady lift coefficient ( $c_l$ ) response given by Theodorsen can be written as:

$$c_l = \pi \frac{c}{2} \left[ \frac{\dot{\alpha}}{U_\infty} + \frac{\ddot{h}}{U_\infty^2} - \frac{ca\ddot{\alpha}}{2U_\infty^2} \right] + 2\pi C(k) \left[ \frac{\dot{h}}{U_\infty} + \alpha + \frac{c}{2} \left( \frac{1}{2} - a \right) \frac{\dot{\alpha}}{U_\infty} \right], \quad (2.1)$$

where  $a$  is the pitch axis location relative to the mid-chord of the airfoil and is measured in semi-chords. The first set of terms in equation (2.1) results from flow acceleration effects (usually called

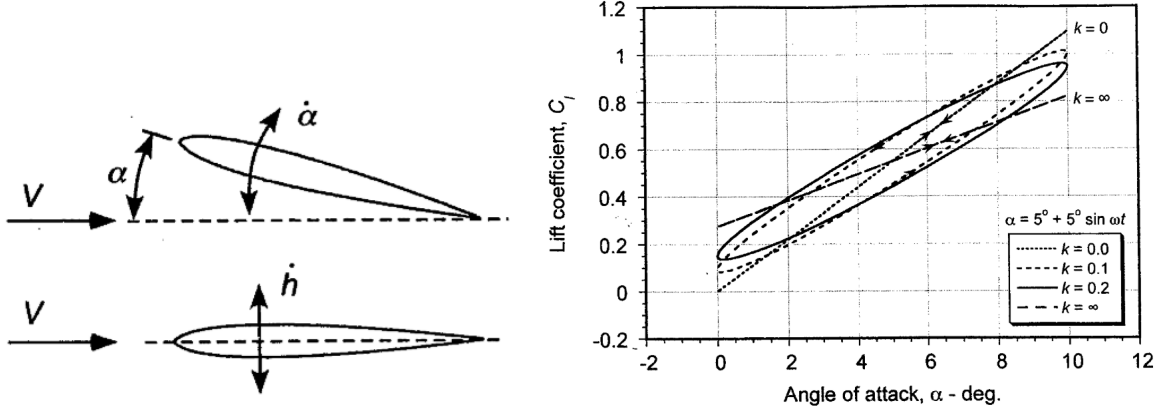


Figure 2.1: (left) Oscillatory motion contributions in Theodorsen's theory. Pitching (top) and plunging (bottom). Reproduced from Leishman [44]. (right) Circulatory part of the unsteady lift response for a sinusoidal variation in  $\alpha$ . Reproduced from [44].

apparent or added mass effects), whereas the second arises from the creation of bound circulation about the airfoil (therefore called circulatory terms). One of the circulatory terms,  $C(k)$ , known as Theodorsen's function, accounts for the effects of the shed wake on the unsteady loads. This complex transfer function can be expressed as:

$$C(k) = \frac{H_1^{(2)}(k)}{H_1^{(2)}(k) + iH_0^{(2)}(k)}, \quad (2.2)$$

where  $i$  is the imaginary unit and  $H_v^{(2)}$  is a Hankel function, which can be expressed in terms of Bessel functions of the first and second kind. The argument of Theodorsen's function,  $k$ , is the reduced frequency of the oscillatory motion. This parameter characterizes the degree of unsteadiness of the motion and appears when non-dimensionalizing the Navier-Stokes equations. It depends on the motion oscillating frequency  $f$ , and can be written as:

$$k = \frac{\pi f c}{U_\infty}. \quad (2.3)$$

Theodorsen's function introduces an amplitude reduction and phase lag effect on the circulatory part of the unsteady lift response, compared to a quasi-steady motion. This effect is represented in Fig. 2.1 (right), where the circulatory part of the lift response to a sinusoidal variation in  $\alpha$  is shown for various  $k$ . This result is reproduced from [44]. It shows the steady-state situation ( $k = 0$ , linear relation between  $\alpha$  and  $c_l$ , with a slope equal to  $2\pi$ ) and three unsteady conditions ( $k > 0$ ). As  $k$  increases, a hysteresis loop is observed (phase lag), such that lift is lower than the steady value when  $\alpha$  is increasing and higher when it is decreasing. The amplitude of the response also decreases with increasing  $k$ . In the limit where  $k$  tends to infinity, the amplitude is half of the steady value and there is no phase lag.

In this project, the two types of oscillatory motions discussed here (pitching and plunging) are studied separately. The experimental measurements of unsteady lift obtained in the WT are compared with those from equation (2.1) considering only the terms that apply to each situation. The deviation from the linear  $2\pi$  slope described by the theory will also be used to construct a theoretical prediction of the LSB behaviour for unsteady conditions, so that it can be compared with the experimental measurements. The unsteady lift can be related to a different static angle of attack, and the LSB location at that static condition may be compared to the unsteady results.

## 2.2. Experimental measurements of unsteady LSBs

As mentioned above, one of the most relevant unsteady aerodynamics phenomena is dynamic stall. For the case of a LSB, this is closely linked to the so-called *bubble bursting* phenomenon. Extensively studied by Gaster [23], bubble bursting is observed to occur when the adverse pressure gradient on a wing's surface reaches a point beyond which the free shear layer that normally encloses the bubble can no longer reattach. This results in an detached free shear layer and comes with a sharp decrease in lift and drag increase. If this occurs due to unsteady aerodynamics, then it holds close relation with the dynamic stall phenomenon and has similar consequences on airfoil behaviour.

Previous WT experiments conducted at The University of Arizona, see Agate et al. [1], have studied the occurrence of bubble bursting for an X-56A airfoil undergoing plunging structural motion. Qualitative behaviour of the LSB forming on the suction side of the wing was observed from surface static pressure measurements and vorticity fields extracted from planar phase-averaged PIV measurements. For situations that did not cause bubble bursting, good agreement was found between the unsteady lift measured in the experiments and Theodorsen's theory. This suggests the suitability of the theory even for the presence of a LSB in the absence of massive flow separation.

This type of experimental investigation has received greater attention for the case of pitching structural motion. Pascazio et al. [56] and Lee and Basu [43] studied the LSB that formed on the suction side of a sinusoidally pitching NACA 0012 airfoil. While the former used an embedded laser velocimetry technique to obtain BL profiles, the latter considered an array of multiple hot-films to link the observed changes in convective heat transfer to the BL state. Both techniques, even being time-consuming and requiring plenty of instrumentation, offer the temporal response needed to study unsteady phenomena. In this case, this worked especially well to study the unsteady transition phenomenon on the separated shear layer from statistical analysis of the measured signals. These two studies considered pitching motions such that bubble bursting occurred during the cycle. For the part of the cycle where the LSB stayed attached, both found a hysteresis in transition location during pitch up and pitch down. It was found that, during pitch up, transition happened downstream of the location measured for the same static  $\alpha$ . The opposite was observed to occur during pitch down. An increased hysteresis was measured for increased reduced frequency of the imposed motion. This behaviour was later observed for the same airfoil by Kim and Chang [40], using surface-mounted hot-wire probes and smoke flow visualization. The qualitative BL transition behaviour is not that different from that of a situation without the presence of a LSB, and can be explained from the unsteady version of Bernoulli's equation, as discussed by Ericsson and Reding [15].

More recently, Nati et al. [52] employed stereoscopic PIV measurements to study the evolution of the LSB that formed on the suction side of a SD7003 airfoil when subjected to a sinusoidal pitching motion. The parameters of the motion imposed were such that no bubble bursting was observed during the cycle. From the phase-averaged PIV measurements, the locations of laminar separation and transition during the cycle were obtained as for a static case, proving the validity of PIV for unsteady LSB investigations. The obtained results are reproduced in Figs. 2.2(a) and 2.2(b) respectively. It can be seen that the pitching motion introduces a hysteresis behaviour of both measured locations. As for previous studies, the pitch down is seen to promote the occurrence of transition to turbulence when compared to the static situation. Again, this can be attributed to the effect that the unsteady motion has on the pressure gradient acting on the wing. During pitch down, the adverse pressure gradient is enhanced, thus causing an earlier separation of the laminar BL and transition to turbulence in the separated shear layer.

This review of existing experiments involving unsteady LSBs reveals the existence of some gaps in the knowledge. Most of the investigations only provide qualitative existence of a LSB during an unsteady cycle, and those giving quantitative information miss some of the characteristic locations that define the position of the bubble. The effect that motion amplitude and reduced frequency

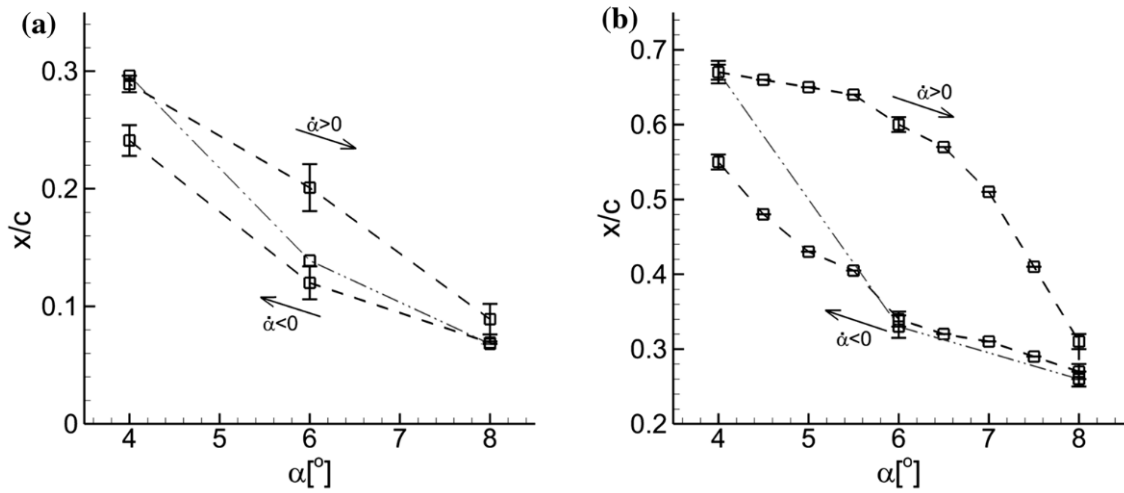


Figure 2.2: LSB characteristic locations for static (dotted line) and unsteady pitching (dashed line) SD7003 airfoil. (a) Laminar separation location. (b) Transition location. Reproduced from Nati et al. [52].

have on the bubble evolution have barely been tackled. Regarding the flow measurement techniques considered so far for this type of experimental investigation, PIV arises as a strong candidate being able of providing quantitative information about the LSB location. Other velocimetry techniques, providing pointwise measurements, involve much more instrumentation and have a lower spatial resolution. The other technique that can provide quantitative information is the use of multiple hot-film sensors. These complicate the experimental setup and may perturb the LSB development, given their extreme sensitivity to surface roughness (Borgmann et al. [8]). So far, the use of an optical, non-intrusive technique, capable of providing direct measurements at the surface and coping with an unsteady situation is still to be made. Here, Infrared Thermography is postulated as a potential alternative, given the recent advances in hardware and data processing that will be detailed in the next chapter.

# 3

## Infrared Thermography for Unsteady Boundary Layer Diagnostics

Infrared Thermography is an optical measurement technique. This means that the measurements are performed with a camera. An infrared camera collects radiation in the infrared band of the electromagnetic spectrum that can be related to the temperature of the object viewed. In the context of this thesis, a relation between the surface temperature of a wing exposed to the flow and the BL state needs to be made. When speaking about BLs, typically the momentum BL is addressed. This refers to the fluid being retarded by the viscous forces near a solid wall. Similarly, a thermal BL will form if there is a temperature difference between the surface and the flow. The link between the momentum and thermal BLs is detailed in §3.1, while §3.2 covers a description of infrared cameras and their measurement principle.

The use of IT for experimental aerodynamics started approximately 50 years ago. The evolution of infrared cameras during this time made it possible to tackle new regimes. The most recent advance in the design and fabrication of infrared cameras is the improvement of acquisition frequency. State-of-the-art infrared cameras can operate even in the kHz regime, which enables them to study unsteady aerodynamic problems. Some limitations still exist, mainly linked to the thermal response of aerodynamic surfaces, which may be overcome using improved data processing techniques. In this regard, the Deutsches Zentrum für Luft- und Raumfahrt (DLR, German Aerospace Center) has made great progress during the last decade, studying phenomena such as unsteady BL transition or dynamic stall in a subsonic environment. The details of their proposed approach are discussed in §3.3, as this is relevant for the purpose of this thesis.

### 3.1. Convective heat transfer and the Reynolds analogy

The concept of momentum BL was introduced by Prandtl in 1904 [58], as a thin region of the flow close to a wall (in this case the surface of a wing) in which viscosity plays a relevant role. Outside of this thin region, the flow may be treated as inviscid. In typical aircraft aerodynamics, with Reynolds numbers in the order of  $10^6$  and higher, the laminar BL developing on the wings transforms into a turbulent BL by a process called laminar-to-turbulent transition. Even if this differs from the LSB case treated in this project, it serves to illustrate some of the key differences between laminar and turbulent BLs. The two types of BLs develop different velocity profiles. At the wall, they also present a different velocity gradient. This is related to the wall shear stress,  $\tau_w$ , through the dynamic viscosity of the fluid,  $\mu$ , as:

$$\tau_w = \mu \left. \frac{\partial u}{\partial y} \right|_{y=0}, \quad (3.1)$$

where  $u$  is the tangential component of the flow velocity and  $y$  is the wall-normal coordinate. The wall shear stress is typically made non-dimensional using the freestream dynamic pressure,  $q_\infty = \frac{1}{2}\rho U_\infty^2$ , creating the skin friction coefficient,  $C_f$ , as:

$$C_f = \frac{\tau_w}{\frac{1}{2}\rho U_\infty^2}, \quad (3.2)$$

where  $\rho$  is the fluid's density. This non-dimensional number represents the friction drag and is therefore a key aspect of airfoil design. Close to the leading edge of the airfoil, a thin laminar BL develops. This will have a high velocity gradient at the wall and thus the skin friction coefficient will be large. As the BL gets thicker along the chord, the gradient reduces as does the friction coefficient. However, due to the shape of the velocity profile of a turbulent BL, a bigger velocity gradient at the wall is present, increasing the friction coefficient. For the BL over a flat plate at zero incidence, which constitutes the Blasius [6] BL profile, this behaviour has been measured experimentally, as is reproduced in Fig. 3.1.

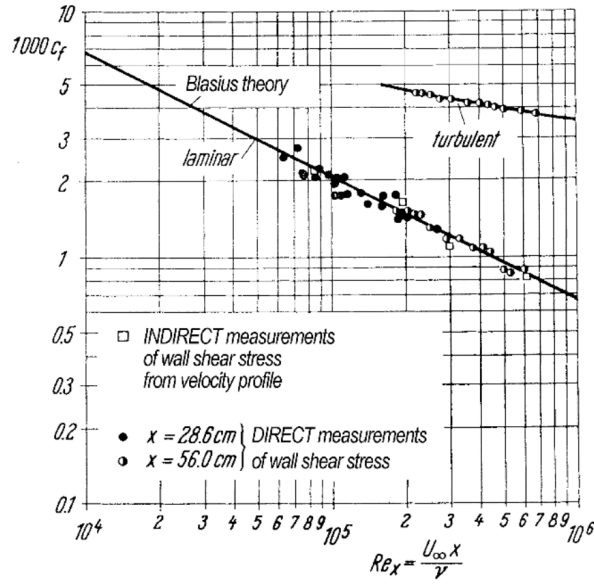


Figure 3.1: Theoretical trend and experimental measurements of the skin friction coefficient  $C_f$  over a flat plate at zero incidence. Reproduced from Schlichting and Gersten [67].

The skin friction coefficient associated with a turbulent BL is typically an order of magnitude higher than the respective laminar BL. This difference allows distinguishing between BL states by measuring the friction coefficient or a related quantity experimentally. The use of IT for experimental BL diagnostics is linked to this concept indirectly. If a temperature difference exists between the surface and the flow, heat exchange between the two will appear. This process will be dominated by convective heat transfer, described by Newton's law of cooling. For a surface at temperature  $T_s$  and neglecting compressibility effects, a convective heat flux  $q_{conv}$  may be described as proportional to the difference in temperature with respect to the flow, which is at temperature  $T_\infty$ . The proportionality parameter is the convective heat transfer coefficient,  $h_s$ . This relationship may be written as:

$$q_{conv} = h_s (T_s - T_\infty). \quad (3.3)$$

A non-dimensional number may be constructed using the heat transfer coefficient. This is the Stanton number,  $St$ , which relates the convective heat transfer with the fluid's thermal capacity,  $\rho C_p$ . It can be expressed as:

$$St = \frac{h_s}{U_\infty \rho C_p}, \quad (3.4)$$

where  $C_p$  is the heat capacity of the fluid. Similarly to the momentum BL described earlier, another BL is formed as a result of the heat transfer between the surface and the flow. This is called the thermal BL, and describes the temperature profile close to the wall due to the heat transfer process. Both BLs are analogous under certain circumstances, which means that there is a physical relationship between them. This is called the Reynolds analogy. For typical airfoil aerodynamics, this relationship may be simply expressed as:

$$C_f = 2St, \quad (3.5)$$

which relates the skin friction with the convective heat transfer. This powerful tool allows to extract information about the friction drag based on the analysis of the convective heat transfer. This is widely used in experimental aerodynamics. In the case of IT, surface temperature measurements can be used to obtain information about the convective heat transfer coefficient and link that to the momentum BL state. A more detailed explanation of the validity of this analogy is given by Schlichting and Gersten [67]. It is important to note that this is only valid for attached flow conditions, both for laminar and turbulent BLs. For a LSB, the assumptions break in the separated region that defines the bubble and no analytical relationship between skin friction and convective heat transfer may be found. In this situation, the relation between surface temperature and the BL state needs to be drawn from computations or experiments involving some other flow measurement technique, as will be discussed later in this thesis.

### 3.2. Radiative heat transfer and infrared scanners

Even if convection is the dominating heat transfer process in most aerodynamic applications, IT makes use of another process: heat transfer by radiation. Radiation is energy transport by electromagnetic waves. All materials (at a temperature above absolute zero) emit energy by means of thermal radiation. As the amount of energy will depend on the body temperature (among other parameters), this may be collected with a scanner to get an estimate of it.

As all materials emit radiation, a body will receive incident radiation (irradiation) from neighbouring bodies. Depending on the body's nature, incoming energy will be partially absorbed, reflected and transmitted by it. This situation is described by Astarita and Carlomagno [3] and reproduced in Fig. 3.2(left). Energy conservation imposes:

$$\alpha_r + \rho_r + \tau_r = 1, \quad (3.6)$$

where  $\alpha_r$ ,  $\rho_r$  and  $\tau_r$  are the dimensionless absorptivity, reflectivity and transmissivity coefficients respectively. Radiative heat transfer theory is derived for a particular situation where  $\alpha_r = 1$ . Bodies fulfilling this condition are called black bodies. These are perfect emitters, which means that they emit the maximum amount of energy possible, at a given temperature, and uniformly in all possible directions. The total energy flux emitted by a black body is described by the Stefan-Boltzmann law, which is just a function of its temperature.

Real bodies emit only a fraction of the energy heat flux emitted by a black body at the same temperature. This fraction is described by the emissivity coefficient,  $\epsilon$ . Generally, this coefficient will be a function of the angle between the direction normal to the body and the direction of emitted radiation, and also of the wavelength. When these dependencies do not occur, bodies are called diffuse emitters and grey bodies respectively. Under these assumptions, Kirchhoff's law states that the emissivity coefficient is equal to the absorptivity coefficient ( $\epsilon = \alpha_r$ ). Many materials, such as those generally used for IT measurements, are opaque in the infrared spectrum, meaning that  $\tau_r = 0$  and therefore the radiation process can be considered as a surface phenomenon. For these bodies, Kirchhoff's law can be expressed as:

$$\epsilon + \rho_r = 1. \quad (3.7)$$

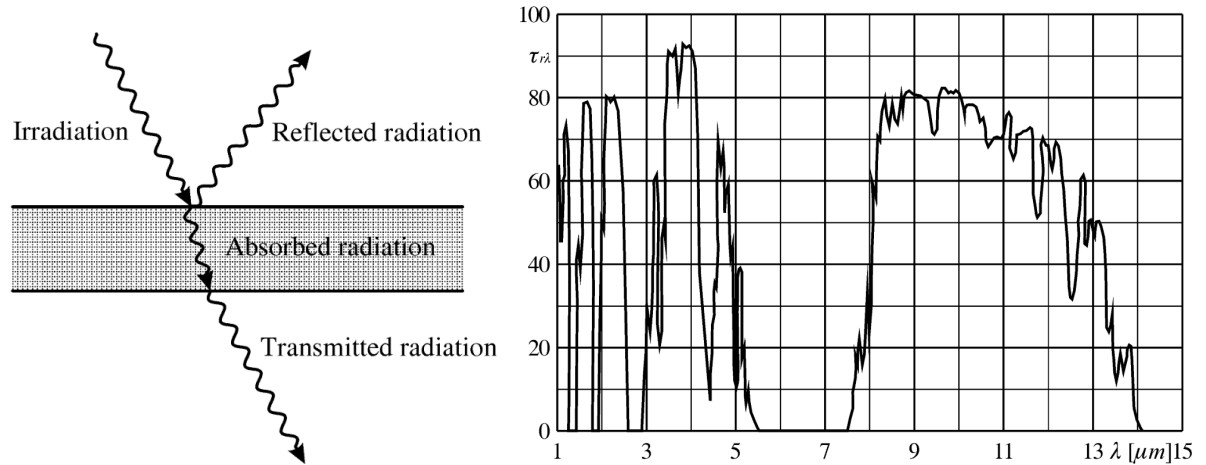


Figure 3.2: (left) Sketch illustrating the absorption, reflection and transmission of irradiation by a body. Reproduced from Astarita and Carlomagno [3]. (right) Atmospheric transmittance in the infrared band. Reproduced from [3].

Materials with low emissivity (as shiny metallic surfaces) not only emit less energy but also reflect a lot of irradiation. These should not be employed in IT applications. For this technique, high emissivity materials are ideal, as they maximize the amount of energy that can be collected with an infrared scanner and also minimize reflections. For a real surface at temperature  $T_s$ , the total energy flux emitted by radiation ( $q_{rad}$ ), using the Stefan-Boltzmann law, may be written as:

$$q_{rad} = \epsilon \sigma T_s^4, \quad (3.8)$$

where  $\sigma$  is the Stefan-Boltzmann constant. Typically, infrared scanners capture only a limited band of the infrared spectrum. Mainly, in the so-called midwave infrared (MWIR) and longwave infrared (LWIR). For common WT experiments, the infrared scanner normally views the model through air, which is not fully transparent (it absorbs part of the energy emitted by the body) in this band of the spectrum. The atmospheric transmittance in this region is reproduced in Fig. 3.2(right). Two so-called atmospheric windows appear, which justify the adopted MWIR and LWIR bands. The significant absorptions are essentially linked to the presence of water vapour and carbon dioxide in the air.

Infrared scanners have evolved significantly since their first appearance in the 1960s as offshoots of military programs. While initially restricted to being point-sensing detectors, the introduction of Focal Plane Array (FPA) detectors in the 1980s changed this to effective two-dimensional transducers containing an array of sensible elements (pixels). The performance of an infrared scanner is typically described by its spatial resolution, acquisition frequency and thermal sensitivity. The spatial resolution is given by the number of pixels in the FPA. The acquisition frequency is mainly connected with the detector response time. This increases for cooled detectors and can go up to the kHz regime for small windows in modern cameras. The thermal sensitivity is expressed in terms of mean noise equivalent temperature difference (NETD). This is defined as the time standard deviation of the background noise averaged over all pixels of a black body. This is normally provided by the manufacturer at ambient temperature and can be as low as 10mK for modern cooled detectors.

The output signal of an infrared scanner is a map of the radiation energy emitted by a surface. In order to convert this into a temperature map, a calibration of the camera is required. For qualitative BL diagnostics, this calibration is not required, and the information of the BL state can be directly inferred from the radiation energy map. This simplifies the process and makes IT a simple technique suitable for BL diagnostics.

### 3.3. Unsteady BL transition detection using IT

The first infrared cameras, pointwise detectors, were developed in the 60s. Their sensitivity limited aerospace applications to study hypersonic phenomena, such as atmospheric re-entry (Stallings and Carver [71]). This was followed by supersonic transition studies in the 70s (Peake et al. [57]). The improvement of infrared cameras during the last two decades of the XXth century made it possible to extend the technique to the subsonic regime, with lower heat transfer values than for supersonic conditions. Different means of introducing temperature differences between aerodynamic surfaces and the flow were discussed during this period, as for example making use of WT cooling (Quast [59]) or heating by Joule effect (de Luca et al. [13]). Besides, IT was also considered to detect BL transition on free-flight experiments (Brandon et al. [10], Horstmann et al. [30]). A more detailed review of aerodynamic research involving IT during this period was written by Gartenberg and Roberts [22]. More recent experiments have focused on studying complex phenomena (Dollinger et al. [14], Richter et al. [64], Overmeyer and Martin [54], Gardner et al. [19], Zuccher and Saric [89]) or comparing results extracted from IT with those from other flow measurement techniques (Joseph et al. [39]). In this regard, some studies have tackled the presence of static LSBs (Ricci and Montelpare [63], Ghorbanishohrat and Johnson [25], Wynnichuk and Yarusevych [86]) and compared the infrared approach with measurements from experimental techniques such as PIV, showing promising results.

State-of-the-art infrared cameras, with high acquisition frequencies and short exposure times, can be used to capture unsteady temperature distributions. This opens the possibility of studying unsteady flow phenomena. In the example of a pitching airfoil, an aerodynamic hysteresis between the instantaneous angle of attack and the lift force has been observed experimentally, which can also be explained from an inviscid perspective using Theodorsen's theory as discussed in §2.1. The aerodynamic hysteresis will be also linked to a hysteresis of the transition location over the airfoil. This creates an unsteady distribution of the convective heat transfer between the surface and the flow. However, the unsteady temperature distribution of the model surface is also influenced by other types of heat transfer processes and the ability of the surface material to react to temperature changes, which is characterized by thermal diffusivity ( $\alpha_m$ ). If the aerodynamic unsteadiness of the problem is sufficiently slower than the thermal responsiveness, the infrared images will capture the unsteady behaviour accurately. However, typically this is not the case. When the aerodynamic unsteadiness is faster, unsteady thermograms will not be representative of the true unsteady situation of the airfoil. A research group from DLR Göttingen has been studying new evaluation methods for IT that can be used to extract aerodynamic information in these situations. Some of the advances of this group will be reviewed in the following, but a more detailed version was given by Wolf et al. [85].

This problem was considered initially by Raffel and Merz [60]. Experiments were carried out on the suction side of a NACA 0012 airfoil, at a Reynolds number of approximately  $Re = 1 \cdot 10^6$ . A sinusoidal pitching motion was imposed on the airfoil to generate an unsteady situation. The airfoil was radiatively heated to increase the signal-to-noise ratio and infrared images were taken at an acquisition frequency of  $f = 210$  Hz. A new evaluation method was introduced, called Differential Infrared Thermography (DIT). As the name suggests, the method consists of subtracting two thermograms from different stages of the pitching cycle. Areas where the flow remains similar will return a zero differential signal. Instead, if the transition location moves between images, a peak will be observed in the DIT image. The complexity of the experiment was later increased to study a pitching rotor blade, as discussed by Raffel et al. [61]. Rectangular untwisted blades with a NACA 0015 were considered, while a sinusoidal cyclic pitch was imposed on the blades. In Fig. 3.3, two infrared images obtained at different instantaneous pitch angles are reproduced, together with their correspondent DIT result.

The infrared image on the left (A) was measured at a higher pitch angle than the one in the

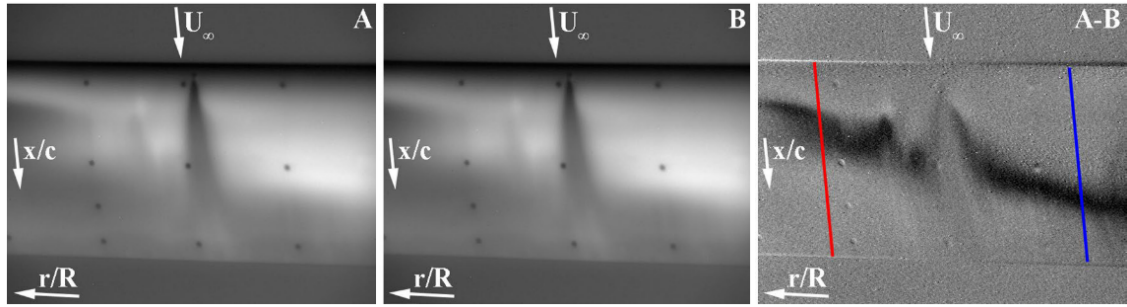


Figure 3.3: Instantaneous infrared images A and B, with  $\alpha_A > \alpha_B$ . Correspondent DIT image on the right. Results reproduced from Raffel et al. [61].

middle (B). As a consequence, it is expected that the transition front moves downstream from A to B. In the images, due to the heated blade, laminar regions appear warmer than turbulent ones. In the DIT image (right) obtained by subtracting A-B, regions where the flow remains almost constant are represented in grey. However, a darker region is observed. This is a result of the transition front moving downstream from A to B. This location was argued to be representative of the transition location at a pitch angle in between the ones for A and B. With this procedure, the transition location could be measured through the pitching cycle except for close to the reversal points. In these regions of the cycle, the transition front moves little and the signal-to-noise ratio of the DIT image drops.

DIT was compared against well-established techniques for unsteady BL transition measurements by Richter et al. [65]. Together with DIT, Hot-film Anemometry and surface pressure measurements were used. A sinusoidally pitching DSA-9A airfoil at  $Re = 1.6 \cdot 10^6$  was considered. Various pitching frequencies were tested in the comparison between techniques. It was also confirmed that the external heating introduced to increase the signal-to-noise ratio of the DIT images had no influence on the transition location. In general, good agreement was found between techniques for all conditions tested. The visible hysteresis in the transition location was observed to increase with increasing pitching frequency. However, the comparison of the transition hysteresis indicated a higher value for DIT. This was assumed to be caused by an additional thermal hysteresis of the model surface. This means that, when using DIT for unsteady transition detection, not only the aerodynamic hysteresis is observed in the temperature distribution but also an undesirable thermal lag effect.

To further investigate this behaviour, the experiment was reproduced numerically by Gardner et al. [18]. A CFD solution for the pitching airfoil was used to obtain the unsteady skin friction coefficient distribution along the chord. From this, the convective heat transfer coefficient was estimated using the Reynolds analogy discussed in §3.1. Then, a one-dimensional thermal model was built to compute the unsteady surface temperature distributions. A finite-difference<sup>6</sup> scheme was designed to solve the unsteady heat equation inside the airfoil. Modelling the material properties of the airfoil used in the experiment, good agreement was found between the model and the experiment in terms of DIT peak location and strength. Transition location was estimated from DIT as in the experiment, but also from the skin friction coefficient CFD solution. This revealed a delay in the DIT peak, thus confirming the effect of an additional thermal hysteresis in the results. After correctly reproducing the experiment, parameters governing the solution such as the airfoil's material or the image time separation were changed to investigate their effect in the DIT measurements. Material properties such as thermal conductivity, heat capacity and density were extracted from various different materials. Improved signal strength was obtained using materials with lower conductivity and heat capacity, but this had no significant effect on the time delay observed for DIT. The effect of the image time separation is reproduced in Fig. 3.4(left). The black line indicating the true transition location is extracted from the skin friction coefficient. It can be observed that increasing the time separation

moves the DIT peak further away from the correct position. In Fig. 3.4(right), the signal strength (DIT peak) and delay (with respect to the skin friction coefficient solution) are normalized using the time separation considered in the experiment. The results indicate that a bigger time separation between images is desirable to obtain higher signal-to-noise ratios, but at the cost of introducing a greater delay and therefore an error in the solution. This shows that the best approach is to reduce the image time separation as long as the signal strength is still acceptable.

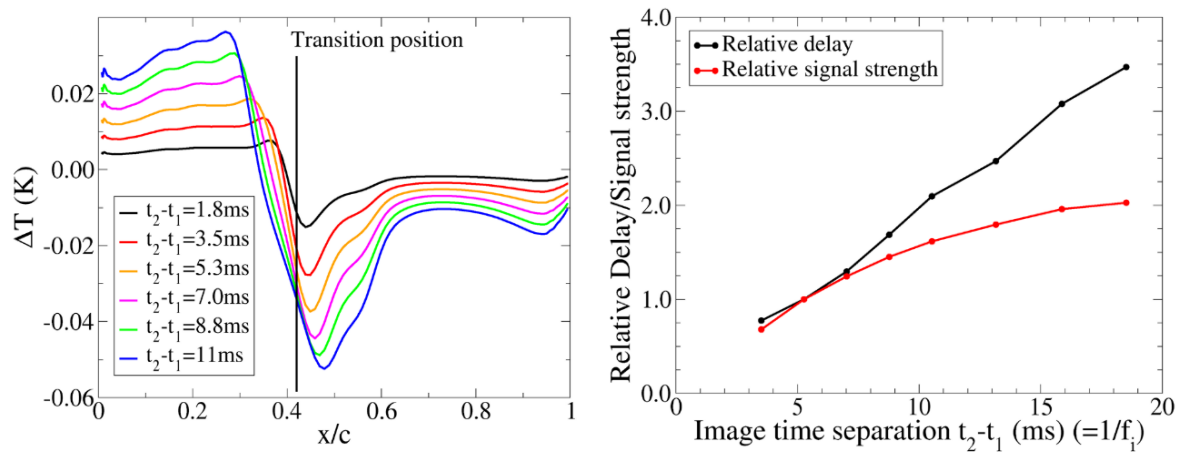


Figure 3.4: Effect of image time separation on the transition location measured with DIT. (left) DIT signal obtained with different time separations. (right) Signal strength and delay normalized with the time separation used in the experiments by Richter et al. [65]. Results reproduced from Gardner et al. [18].

After this, some studies have focused on trying to optimize the image time separation for best results (Wolf et al. [84], Mertens et al. [48]), while others have increased the experimental complexity. Weiss et al. [81] considered a helicopter rotor under cyclic pitching conditions and Gardner et al. [21] tested a full helicopter in forward flight. This same group also extended the capabilities of DIT to study the dynamic stall phenomenon. Gardner et al. [17] considered this approach for a pitching airfoil while Raffel et al. [62] extended it to the helicopter rotor.

From the DLR work, it is clear that the surface material selection and heating method plays a relevant role in unsteady IT measurements. Simon et al. [69] investigated the dynamic response of the surface temperature measured with IT on a flat plate. Transition was forced with a pulsed disturbance source to introduce a dynamic behaviour. Three heating techniques were considered in the experiment: an external heat lamp, an internal resistance heating foil and a conductive paint. For the external and internal heaters, the plate was covered with a thin layer of a low heat capacity and thermal diffusivity material. The results indicate that the external heater works better than the internal for disturbances in the order of 1 Hz and lower, due to the lower thermal capacity of the structure. The behaviour changed for higher frequencies. The conductive paint works slightly better than the other techniques, especially at higher frequencies. For all situations, a low conductivity material is desired at the surface for increased spatial resolution.



# 4

## Experimental Setup

All the experimental work involved in this project was conducted in the Arizona Low-Speed Wind Tunnel (ALSWT) situated in the Department of Aerospace and Mechanical Engineering at The University of Arizona (UA). The facility is described in detail in §4.1. The two-dimensional wing studied consists of a modified NACA 64<sub>3</sub> – 618 airfoil of the Aeromot 200S Super Ximango motor glider (the modified airfoil has a higher maximum lift coefficient than the original NACA 64<sub>3</sub> – 618), which was shown in Fig. 1.1(right). The project focuses on the LSB that forms on the suction side of the airfoil at a chord-based Reynolds number of  $Re = 200k$ . Apart from a static characterization of it over a range of angles of attack, two types of structural motion were imposed on the wing. The instrumentation contained in the wing and the mechanisms used to impose the structural motion are introduced in §4.2.

The remaining sections in this chapter describe the different flow measurement techniques employed to detect and characterize the LSB in the experiments. §4.3 covers the surface pressure measurements, §4.4 the PIV setup and data reduction and finally a deeper description of the IT approach is given in §4.5.

### 4.1. Wind tunnel facility

The ALSWT is a versatile, closed-loop, low turbulence wind tunnel. A plan view of the facility is shown in Fig. 4.1. Please note that the flow in the test section is from right to left in the figure. In the remainder of this document, flow can be assumed from left to right unless elsewhere stated. The facility is primarily constructed of a composite lamination of fibreglass reinforced plastic with a rigid, balsa wood core. This produces a stiff, lightweight structure with a natural frequency higher than the fan *rpm* to avoid vibration-induced turbulence in the freestream. The tunnel has a test section of 0.91 m x 1.22 m x 3.66 m (height x width x length). The test section walls consist of acrylic panels allowing for optical access. The maximum flow speed in the test section is 80 m/s. Uniformity of the mean flow over the test section is at or better than 0.5 % and turbulence intensity ( $Tu$ ) is less than  $Tu \leq 0.035\%$  in the range of 1 Hz to 10 kHz for the conditions considered here (see Borgmann et al. [7]). The temperature inside the tunnel is regulated by a heat exchanger with a chilled water supply. Throughout the experiments, temperature is held within the range of 0.55 °C of 22.2 °C. A Pitot tube is mounted 0.4 m downstream of the test section entry at the tunnel sidewall reaching into the free stream to acquire total and static pressures to determine the flow speed and as a reference for static pressure measurements. The suitability of ALSWT for boundary layer stability and transition research was demonstrated by [7].

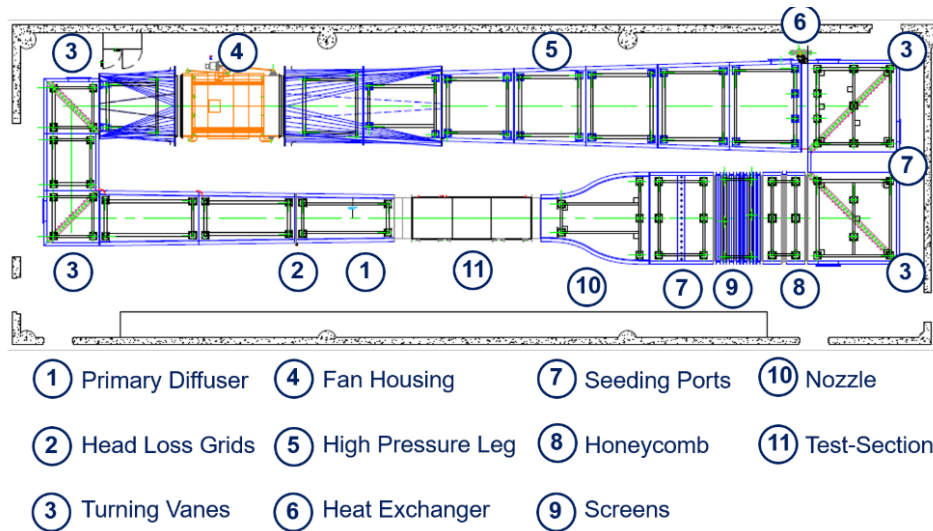


Figure 4.1: Plan view of the Arizona Low Speed Wind Tunnel. Reproduced from Borgmann et al. [7].

## 4.2. Wing section

A modified NACA 64<sub>3</sub> – 618 airfoil was employed in the current investigation. The instrumented wind tunnel model made of carbon fiber was constructed in-house at UA. The chord length is 1 ft (304.8 mm) and the span is 4 ft (1219.2 mm). Instrumentation includes 60 static pressure taps and a high bandwidth piezoresistive pressure transducer. The taps are drilled with a 15° angle with respect to the chord to prevent undesired BL modification influences. 36 of the pressure taps are located along the chord at mid-span, whereas the remaining 24 are located at 1/4 and 3/4 span, to investigate the three-dimensionality of the flow. For the range of angles of attack investigated, a two-dimensional behaviour was consistently observed, and therefore only the results at mid-span will be discussed here. The distribution of the mid-span taps is shown in Fig. 4.2, together with the pressure transducer located at 65% of the chord.

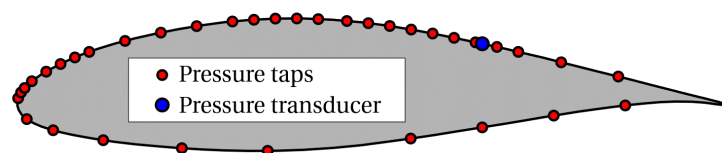


Figure 4.2: Distribution of pressure taps at mid-span and pressure transducer at 65% of the chord.

A higher distribution of pressure taps is present close to the leading edge of the wing, to capture the suction peak for accurate lift coefficient estimations. Similarly, resolution was increased on the rear part of the suction side to capture the LSB better.

### 4.2.1. Pitching mechanism

A VELMEX BiSlide stepping motor was connected to the wing spar at 40% of the chord using a simple wheel-crank mechanism to change the angle of attack. A picture of the mechanism, connected to the wing inside the test section, is shown in Fig. 4.3(left). This creates a constant pitching motion. The pitching rate can be easily adjusted by setting the *rpm* of the stepping motor. The motor is controlled using a VELMEX VXM-1 controller, which can simultaneously output a trigger signal at desired locations of the motion. This signal is used for phase-averaging of the static pressure measurements and triggering of the PIV acquisition system. In this investigation, the wing is pitched

between  $-3$  and  $7$  degrees  $\alpha$  (5 degrees amplitude), both up and down. At  $\alpha = 2^\circ$  (middle of the motion), the aerodynamic pitching moment is zero at the location of the pitching axis (40% chord). This creates symmetric motion around that point and minimizes the aerodynamic loading on the pitching mechanism.

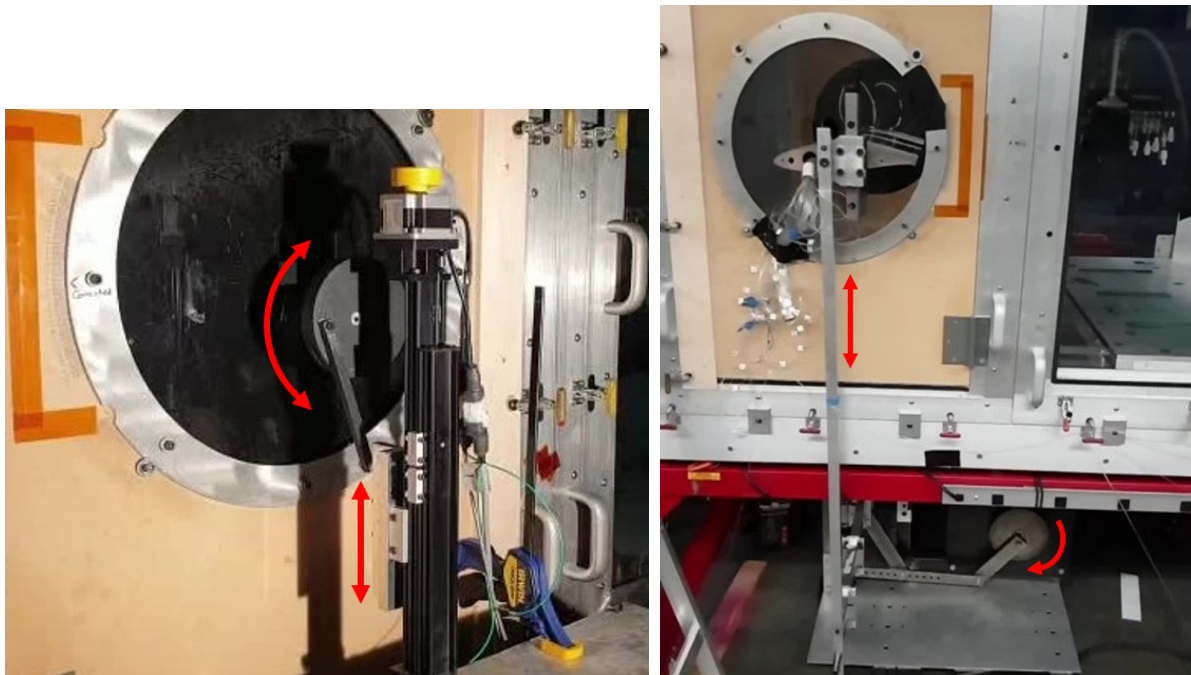


Figure 4.3: Mechanisms employed to impose the desired structural motions on the wing. (left) Pitching. (right) Plunging.

In the experiments, the imposed motion amplitude was slightly above 5 degrees to ensure that the motor reached a constant speed in the desired range. The time that it takes to travel the full pitching ramp (from  $-3$  to  $7$  degrees  $\alpha$  or vice versa) is used to define a motion period (as double that time) and from there a reduced frequency  $k$  that characterizes the unsteadiness of the motion. Various reduced frequencies have been tested to increase the complexity of the motion from a quasi-steady situation ( $k \ll 1$ ) to a fully unsteady case. The reduced frequencies tested are summarized in Table 4.1, together with the dimensional frequency of the motion and the constant pitching rates used for each case. While every setpoint was measured with the pressure taps and the infrared camera, only  $k = 0.05$  and  $k = 0.15$  were considered with PIV to simplify the experimental campaign.

Table 4.1: Pitching experiment test matrix

Pitching rate, $\dot{\alpha}$ [deg/s]	0.045	1.128	2.256	11.279	22.558	33.837	45.115	56.394
Motion frequency, $f$ [Hz]	0.002	0.056	0.113	0.564	1.128	1.692	2.256	2.820
Reduced frequency, $k$	0.0002	0.005	0.010	0.050	0.100	0.150	0.200	0.250

#### 4.2.2. Plunging mechanism

The plunging structural motion was imposed with an oscillatory plunging mechanism, driven by a frequency-controlled AC motor, designed and manufactured in-house at UA. It introduces a sinusoidal plunging motion to the model. This mechanism is an adaptation of the one previously employed by Agate et al. [1]. It allows for variation in the oscillation frequency of 3-8 Hz, and amplitude of 10-20 mm (approximately 3-6% of the chord) while wind tunnel plugs allow for variation in the nominal angle of attack ( $\alpha_{nom}$ ). A u-shaped frame supports both ends of the model to eliminate

whiplash effects associated with a one-sided forcing. The mechanism, connected to the wing, is shown in Fig. 4.3(right). The plunging configuration discussed in this thesis consists of a reduced frequency of  $k = 0.67$  and a non-dimensional motion amplitude of  $h = 6\%$ , with  $\alpha_{nom} = 0^\circ$ .

The vertical position of the wing ( $y_w$ ) through the plunging cycle can be described using the motion amplitude and phase angle ( $\phi$ ), as:

$$y_w = h \sin(\phi), \quad (4.1)$$

where both length scales have been non-dimensionalized using the airfoil chord. Alternatively, the phase angle can be described in terms of the motion frequency and time, or using the reduced frequency of the motion. This allows rewriting equation (4.1) as:

$$y_w = h \sin(\phi) = h \sin(2\pi f t) = h \sin\left(2k \frac{U_\infty}{c} t\right). \quad (4.2)$$

The time derivative of this expression describes the vertical velocity of the wing ( $\dot{y}_w$ ) during the plunging cycle, non-dimensionalized using  $U_\infty$ . This may be expressed as:

$$\dot{y}_w = 2kh \cos \phi. \quad (4.3)$$

The vertical velocity can be used to extract the angle of attack induced by the plunging motion, which in combination with  $\alpha_{nom}$  defines the effective angle of attack ( $\alpha_{eff}$ ) through the cycle. This can be written as:

$$\alpha_{eff} = \alpha_{nom} - \tan^{-1}(\dot{y}_w) = \alpha_{nom} - \tan^{-1}(2kh \cos \phi). \quad (4.4)$$

The motion starts ( $\phi = 0$ ) at the mid-upstroke of the cycle, when the wing is moving up with maximum vertical velocity. The description of the vertical position and effective angle of attack through the cycle is represented in Fig. 4.4 in terms of the phase angle, as described with equations (4.1) and (4.4) respectively, after introducing the values discussed above.

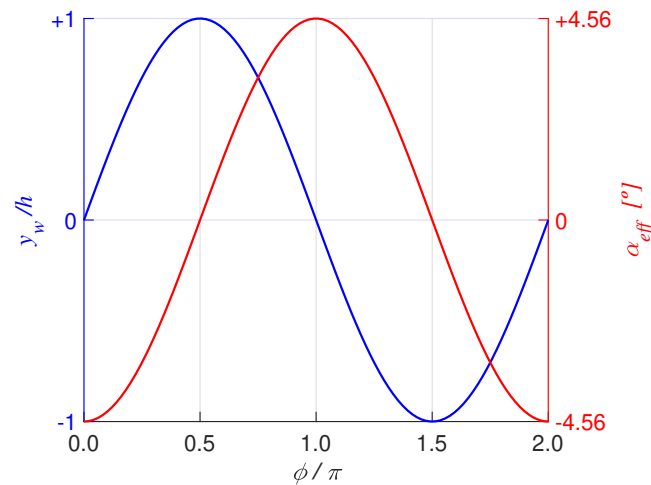


Figure 4.4: Wing's vertical position and effective angle of attack through the plunging cycle, in terms of the phase angle of the motion.

To track the motion, a Hall effect sensor was used, as described by Agate et al. [2]. A magnet was placed at the mechanism's vertical sting, which moves relative to the sensor, fixed to the wind tunnel. The signal increases when magnet and sensor get closer to each other. This is used to extract the motion frequency and for phase-averaging of the flow measurement techniques.

### 4.3. Surface pressure measurements

Two different types of surface pressure measurements were acquired in the experiments. Static pressure coefficient distributions were obtained from the pressure taps, while the nature of the transition process occurring in the separated shear layer was studied from the pressure fluctuations extracted from the high-bandwidth transducer at 65% of the chord. Scanivalve ZOC33 pressure scanners in combination with an ERAD Remote A/D module, with a range of 10 inH<sub>2</sub>O (2490 Pa) were used to record static pressure. The system was sampled at 504 Hz, during approximately 2 s for static situations (for time-averaging) and 100 motion cycles for unsteady investigations (both pitching and plunging). Phase-averaging of the pitching data is accomplished by simultaneously acquiring a trigger signal from the stepping motor controller sent at 1 degree  $\alpha$  increments. Phase-averaging of the plunging data is accomplished by simultaneously acquiring the signal of a Hall effect sensor, as described above. The accuracy of the system is given as  $\pm 0.1\%$  of the measurement range. The uncertainty of the mean pressure measurements is estimated (with a 95% confidence interval, and following the description of Moffat [51]) to be less than 4% of the freestream dynamic pressure ( $q_\infty$ ) for static configurations, while this value increases up to 7% for the unsteady situations. Uncertainty representation is omitted in the  $c_p$  results for improved visualization. The uncertainty is then propagated to lift coefficient using a stochastic approach, assuming that all variables involved follow a normal distribution. This is indicated by error bars in the results. The parameters of the pressure taps setup are summarized in Table 4.2.

Table 4.2: Static pressure taps parameters

	Static	Unsteady
Sampling rate	504 Hz	
Number of samples	1000	100 cycles
Uncertainty	<4%	<7%

A high bandwidth Endevco 8507C-1 pressure transducer is installed on the wing's surface, at  $x/c = 0.65$ . The sensor has a range of 1 psi (6895 Pa) and a resonance frequency of 55 kHz. The sensor was sampled at  $2^{15} = 32768$  Hz and acquired during 10 s for static configurations or 100 motion cycles for the plunging case. The signal was then lowpass filtered at 10 kHz. For the static case, spectral analysis of the pressure fluctuations is conducted using Welch's method, using Hamming windows of length  $2^{12}$  and 50% overlap. This results in a frequency resolution of 8 Hz. For the plunging configuration, the pressure signal is transformed using a Continuous Wavelet Transform (CWT) using an analytic Morse wavelet with a symmetry parameter of 3 and a time-bandwidth product of 60, as described by Lilly [45]. The transformed signal is then phase-averaged to the imposed motion using the Hall sensor signal.

### 4.4. Particle Image Velocimetry

Planar, 2D PIV was used to analyze the evolution of the LSB developing on the suction side of the airfoil. Submicron seed particles (DEHS) were illuminated with a Quantel Evergreen dual head laser. Images were acquired, in double-frame mode, with a LaVision sCMOS camera. The camera had to be slightly tilted for optical access and was therefore equipped with a Scheimpflug adapter to maintain the full field of view in focus. Processing of the images was performed with the LaVision DaVis 8.3 software. All particle images were preprocessed using a temporal sliding minimum subtraction to minimize reflections at the model surface. The main processing stage consisted of a multi-pass cross-correlation algorithm. Uncertainty of the mean velocity magnitude was estimated following the description of Wieneke [83], and given as a percentage of the freestream speed using a 95% confidence interval. For the static characterization of the LSB, 800 images were acquired at 14 Hz for time-averaging. 400 phase-locked PIV images were acquired for the pitching and plunging scenar-

ios using a programmable timing unit from the LaVision system that was coupled with the trigger signal from the stepping motor controller and Hall sensor respectively. The main parameters of the PIV setup are summarized in Table 4.3.

Table 4.3: PIV parameters

	Static	Unsteady
Number of images	800	400
Sampling rate	14 Hz	phase-locked to the motion
Frame separation		30 $\mu$ s
Lens focal length		50 mm
$f_{\#}$		4
Sensor resolution		2560 $\times$ 2160 px
Final pass window size		16 $\times$ 16 px
Final pass overlap		75%
Vector pitch		0.25 mm ( $8.2 \times 10^{-4} \cdot c$ )
Uncertainty	<2%	<5%

In the pitching investigation, for each reduced frequency tested, measurements were conducted for 1 degree increments in  $\alpha$ . This creates 22 phases in total (11 for pitch up and 11 for pitch down). For the plunging case studied, 16 equally spaced phases were measured along the sinusoidal cycle.

The PIV setup in the ALSWT is sketched in Fig. 4.5, which does also include the other measurement techniques considered and the two types of unsteady mechanisms.

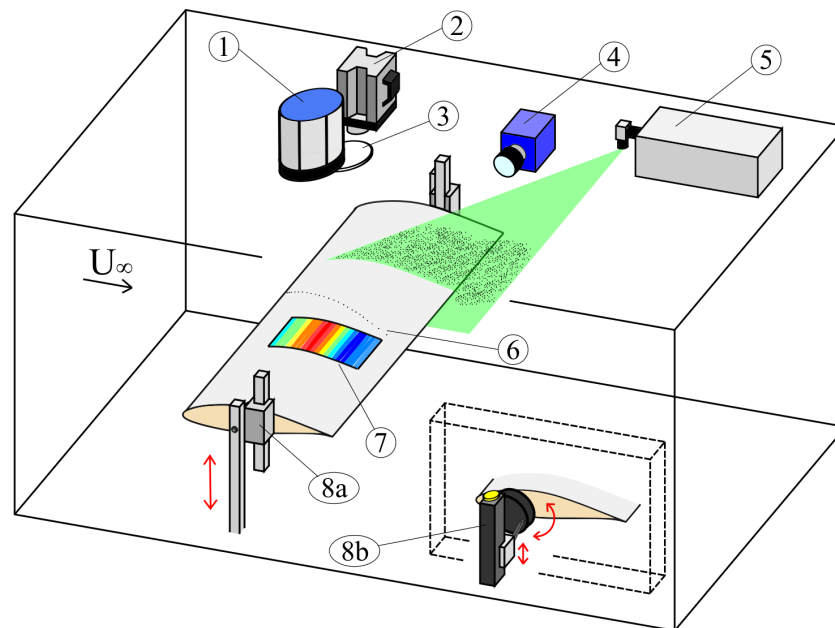


Figure 4.5: Sketch of the experimental setup in the Arizona Low-Speed Wind Tunnel. 1- Halogen lamp; 2- Infrared camera; 3- Ceiling aperture for infrared access; 4- PIV camera; 5- Laser head; 6- Mid-span pressure taps; 7- Region of interest for IT; 8a- Plunging mechanism; 8b- Pitching mechanism.

#### 4.5. Infrared Thermography

Surface temperature on the suction side of the wing was measured using a state-of-the-art infrared camera sensitive in the MWIR band. Due to camera availability, a slightly different camera was used for the pitching investigation (FLIR X6903sc) compared to the static and plunging ones (FLIR

X8501sc). In Fig. 4.6, the experimental setup for the IT configuration is described. This shows the wing installed in the test section. In the region of interest, a thin film with low thermal conductivity was added to the airfoil skin, to increase surface emissivity and reduce conduction effects at the surface and into the wing inner structure. This same material was also added to the PIV region to reduce laser reflections at the surface. Copper tape fiducial markers (reflective in the infrared band) were placed at known locations on the surface, to transform the infrared images onto the wing coordinate system using a projective transformation. The wing was heated externally using a 1 kW halogen lamp placed above the WT test section, to enhance convection between the surface and the flow. For infrared optical access, a small orifice was made in the acrylic ceiling. Additional PIV measurements were conducted on the heated surface to ensure that the increased surface temperature did not have any considerable effect on the BL development.

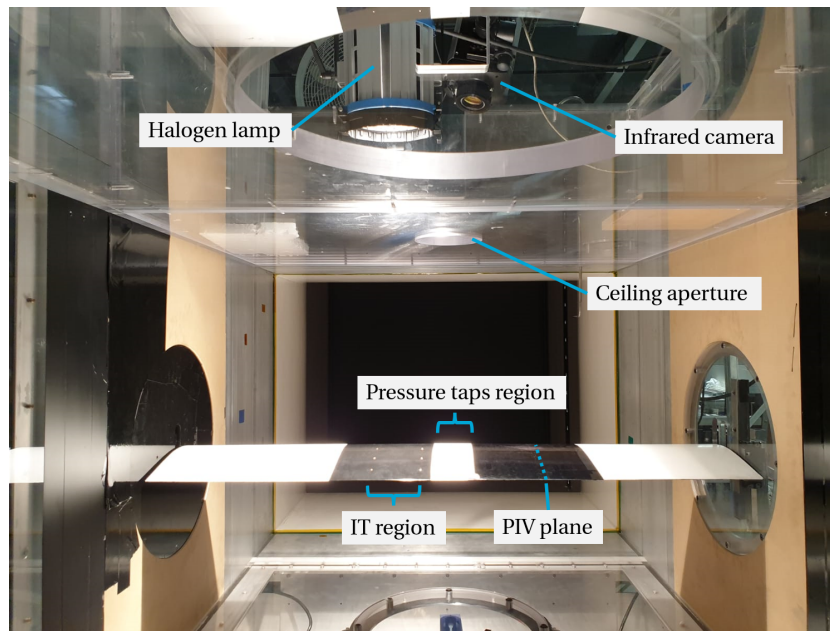


Figure 4.6: Infrared Thermography setup in the Arizona Low-Speed Wind Tunnel.

For static measurements, the surface was first heated to around 10 K above ambient in quiescent conditions, and the WT was then started with the halogen lamp still turned on. When a steady-state temperature distribution was achieved (approximately 1 minute after the WT speed settled), 500 images were sampled at 50 Hz for time-averaging.

In the pitching investigation, pitch up and pitch down were studied separately. For a pitch up case, the wing was first moved to an angle of attack below the minimum of the motion of interest ( $\alpha = 2^\circ \pm 5^\circ$ ) until a steady-state was reached. The pitch up motion was then started and the infrared camera was triggered by the stepping motor controller when  $\alpha$  reached the beginning of the constant pitch ramp ( $\alpha = -3^\circ$ ). From there, the camera sampled at 180 Hz until  $\alpha = 7^\circ$  was reached. This way, the LSB is expected to move only in one direction during the acquisition (upstream for a pitch up case), simplifying the analysis of the thermal response of the surface. An analogous procedure was used to study the pitch down configuration.

The infrared camera was not triggered for the plunging investigation. Here, steady-state was reached at the nominal angle of attack ( $\alpha_{nom} = 0^\circ$ ). Then, the plunging was started. When the motor achieved a smooth operation, the infrared camera started sampling at 180 Hz and collected 5000 samples. The position of the wing along the plunging cycle was directly identified from the infrared images, as will be detailed in the following chapter. The main parameters of the IT setup are summarized in Table 4.4.

Table 4.4: IT parameters

	Static	Pitching	Plunging
Camera model	FLIR X8501sc	FLIR X6903sc	FLIR X8501sc
Spectral range	3 - 5 $\mu\text{m}$	3 - 5 $\mu\text{m}$	3 - 5 $\mu\text{m}$
Thermal sensitivity (NETD)	<30 mK	<20 mK	<30 mK
Sampling rate	50 Hz	180 Hz	180 Hz
Number of images	500	variable	5000
Integration time	0.5 ms	2.8 ms	0.5ms
Lens focal length	50 mm	25 mm	50 mm
Sensor resolution	1280 $\times$ 1024 px	640 $\times$ 512 px	1280 $\times$ 1024 px
$f\#$	2.5	4	2.5

The infrared camera was not specifically temperature calibrated for this experiment. The factory calibration was used to get a rough estimate of the global temperature of the heated surface, but in the image processing stage only the infrared intensity measured directly by the sensor was considered. For the small temperature changes considered here, the calibration is quasi-linear and therefore the intensity distribution resembles well that of the temperature.

# 5

## Methodology

In this project, the location of the LSB that forms on the suction side of a modified NACA 6-series airfoil, at a chord-based Reynolds number of  $Re = 200k$ , is measured using three different experimental techniques. The full description is defined by the characteristic locations of the bubble: separation of the laminar BL, transition to turbulence occurring in the separated shear layer and finally reattachment of the turbulent BL. These are estimated from static pressure coefficient distributions, velocity fields (from PIV) and surface temperature (from IT). All the discussion described here refers to the location of a two-dimensional bubble in a time-averaged sense. This is especially relevant for the reattachment process, which is typically highly unsteady, involving the shedding and advection of vortical structures (see for example Burgmann et al. [12]). Similarly, the transition process is simplified to occur at a particular location rather than a finite region.

The detection of the LSB from the pressure taps is detailed in §5.1. A robust approach, based on literature, is applied to improve the spatial resolution of the technique. Next, the approach for the two-dimensional velocity fields obtained from the PIV measurements is covered in §5.2. While the methodology applied for the pressure taps and PIV works equally for static and unsteady investigations, a different approach is needed for the case of IT. The thermal response of the surface influences the temperature measured with the infrared camera, which does not resemble the instantaneous BL state. This means that a detection method based only on surface temperature will fail for an unsteady situation. A variation of the Differential Infrared Thermography approach is introduced here to detect an unsteady LSB. The full methodology linked to the processing of infrared images can be found in §5.3. This includes the transformation of raw images to a known coordinate system, the detection of a static LSB from steady-state temperature distributions and the novel DIT approach for unsteady situations. The chapter concludes with the discussion of an analytical thermal model for a simplified unsteady situation. This approach is used to compare the experimental measurements with existing DIT research and will later serve to explain the results presented in chapter 6.

### 5.1. LSB detection from surface pressure taps

Surface pressure taps are one of the most common flow measurement techniques employed in WT testing. They are widely used to obtain static pressure coefficient distributions. From those, lift and pitching moment coefficients can be easily obtained, applying a numerical integration of the pressure measurements. The presence of a LSB, typical of low Reynolds number environments, can have a significant effect on the  $c_p$  distribution. The curve deviates from the inviscid solution as an effect of the flow separation and reattachment processes.

As described by O'Meara and Mueller [53], flow separation causes the formation of a pressure plateau, which ends when transition to turbulence occurs. This is followed by a quick pressure

recovery, linked to the reattachment process, after which the curve returns back to the inviscid solution. In a WT experiment, the discrete distribution of pressure taps complicates the accurate location of these features. To overcome this spatial limitation, some studies have proposed the use of data fitting techniques to detect the characteristic locations of the bubble. For example, Gerakopoulos et al. [24] used a shape-preserving polynomial, as was illustrated in Fig. 1.3(left).

A more robust approach, based solely on linear fits, was later proposed by Boutilier and Yarusvych [9]. This same technique was considered for all the experimental measurements covered in this thesis (both static and unsteady). The technique is illustrated using as an example the static pressure coefficient distribution obtained for the static wing at  $\alpha = 5^\circ$ . This is shown in Fig. 5.1.

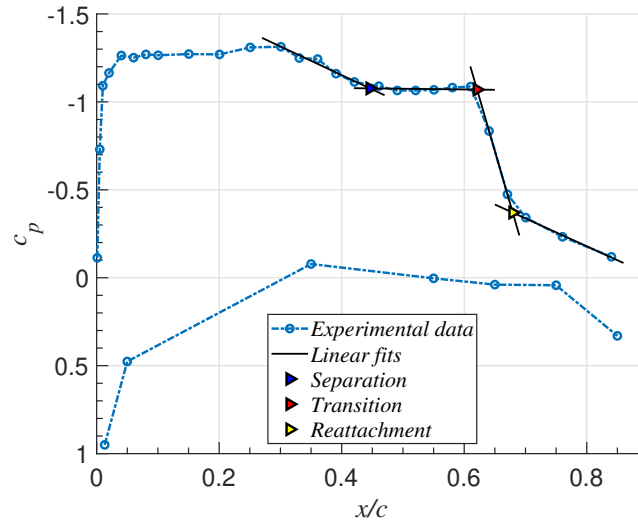


Figure 5.1: Static pressure coefficient distribution for the static wing at  $\alpha = 5^\circ$ . Linear fits illustrating the methodology to detect the LSB characteristic locations.

The pressure plateau that forms after flow separation, as described by [53], is visible on the suction side of the  $c_p$  distribution, approximately at  $0.45 \leq x/c \leq 0.60$ . The characteristic locations of the LSB, indicated by coloured triangles, are estimated from the intersection of four different linear fits applied to the experimental data. The first one is applied to the adverse pressure gradient region before the formation of the plateau, the second to the pressure plateau itself, the third to the quick pressure recovery region and a fourth one is constructed downstream of this region.

The technique requires a sufficient number of taps in each region to produce reliable fits. In the present investigation, the distribution of taps drops closer to the trailing edge, with the last one being at  $x/c = 0.84$ . This is not a problem for the case shown here, but complicates the analysis for lower incidences, as the bubble moves downstream. The technique fails to detect transition and reattachment for some of the angles of attack tested. This applies to the static characterization and the unsteady situations.

No automation of the technique was possible during the course of this project, making it more time-consuming than others discussed in this chapter. For every setpoint analyzed, the taps forming each of the four regions distinguished had to be chosen manually. This was again mainly caused by the uneven distribution of the pressure taps.

## 5.2. LSB detection from PIV

The characteristic locations of the LSB can be detected from the two-dimensional velocity fields obtained from the PIV measurements. The methodology explained here is applicable to both static and unsteady investigations. For a more clear description, a static example obtained at  $\alpha = 2^\circ$  is given

in Fig. 5.2(a). This shows contours of time-averaged velocity magnitude ( $\bar{U}$ ), non-dimensionalized using the freestream speed  $U_\infty$ . Streamlines are included to further visualize the LSB. From there, an iterative approach is followed to obtain the dividing streamline that encloses the bubble from the outer flow. Velocity vectors closest to the surface are omitted for this calculation, as they are prone to higher uncertainty due to laser reflections. The obtained streamline is then extrapolated until it intersects with the airfoil (Kurelek et al. [41]). The dividing streamline is used to define the laminar separation and turbulent reattachment locations. The obtained streamline and characteristic locations are shown in Fig. 5.2(b) for the example discussed here. In the plunging investigation, the vertical velocity of the wing (as described by equation (4.3)) needs to be subtracted from the measured one to correctly define the streamline in the frame of reference that moves with the wing.

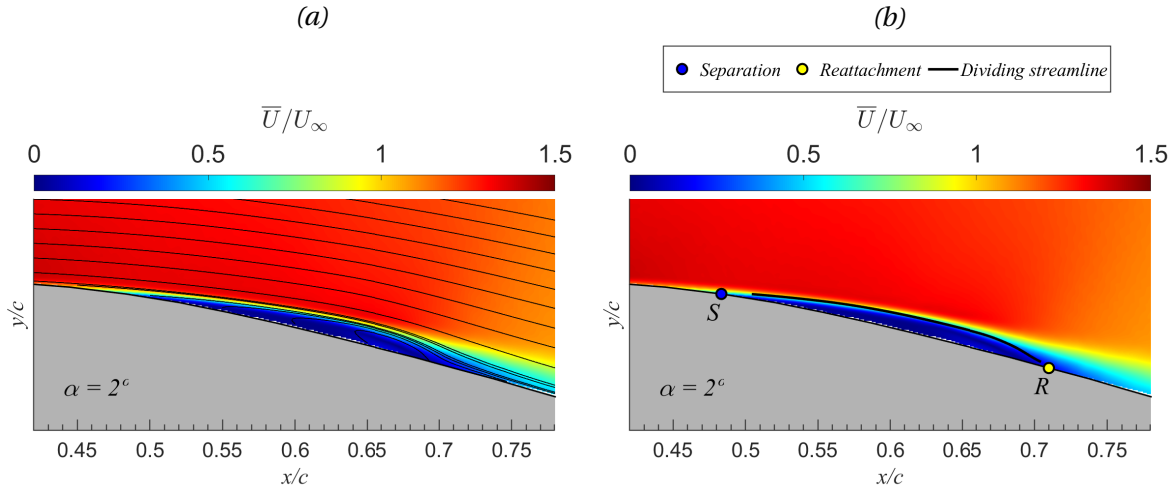


Figure 5.2: Contours of time-averaged velocity magnitude for the static wing at  $\alpha = 2^\circ$ . (a) With added streamlines. (b) With dividing streamline included.

The location of transition to turbulence occurring in the separated shear layer is estimated from the BL characteristics. First, the two-dimensional velocity field measured is transformed from a Cartesian coordinate system to a curvilinear one (as the one described by Hosseinverdi and Fasel [35]) using linear interpolation. The new coordinate system is vaguely defined by  $x-y$  for simplicity. Then, for every  $x$  location inside the bubble and following the line normal to the surface, the BL displacement ( $\delta^*$ ) and momentum ( $\theta^*$ ) thicknesses are obtained as:

$$\delta^*(x) = \int_0^{\delta(x)} \left(1 - \frac{u(x,y)}{u_e(x)}\right) dy, \quad (5.1a)$$

$$\theta^*(x) = \int_0^{\delta(x)} \frac{u(x,y)}{u_e(x)} \left(1 - \frac{u(x,y)}{u_e(x)}\right) dy, \quad (5.1b)$$

where  $u_e$  is the edge velocity and  $\delta$  is the BL thickness (where the edge velocity is first reached). For these calculations, an additional point is added at  $y = 0$  to enforce the no-slip condition at the wall, as  $u(x,0) = 0$ . From equation (5.1), the BL shape factor ( $H$ ) distribution can be simply obtained as:

$$H(x) = \frac{\delta^*(x)}{\theta^*(x)}. \quad (5.2)$$

These estimations are given for the example case in Fig. 5.3(a). Here, following the discussion of Michelis et al. [49], the transition location is estimated to happen where the BL shape factor reaches a maximum, as indicated by the coloured circle. This information is joined together with the dividing streamline to provide all-three characteristic locations of the LSB from the PIV measurements. The final version is shown in Fig. 5.3(b). This consists of the same example case discussed above,

now with all characteristic locations included as coloured dots. Streamwise velocity BL profiles are included for better representation of the LSB.

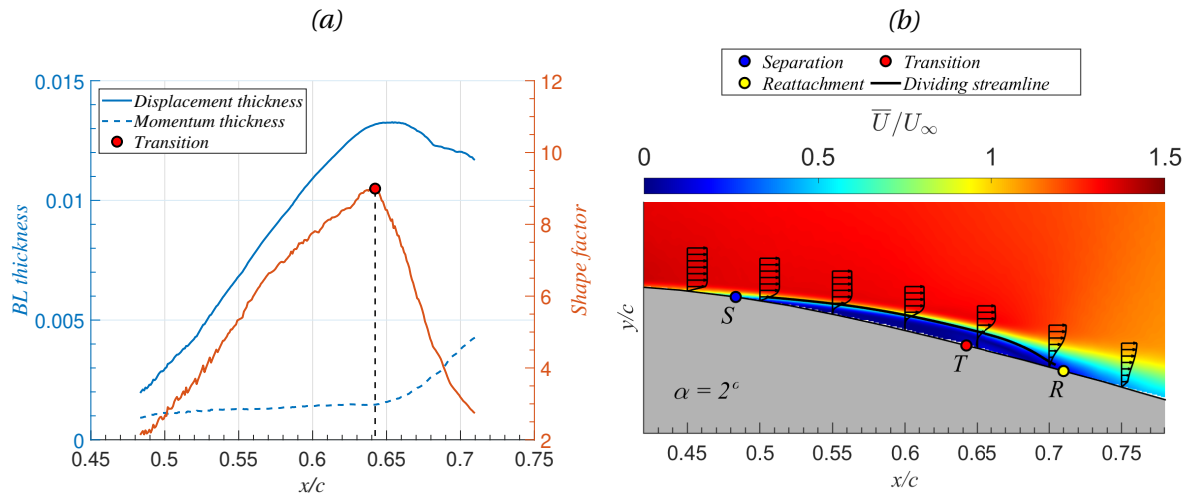


Figure 5.3: (a) BL characteristics for the static wing at  $\alpha = 2^\circ$ . (b) Contours of time-averaged velocity magnitude with streamwise velocity BL profiles for the static wing at  $\alpha = 2^\circ$ .

### 5.3. LSB detection from IT

The detection of the LSB from the infrared images is significantly more complex. In the case of PIV, state-of-the-art software simplifies the calibration and data processing stages. This had to be done manually for the infrared case. The main step consists of transforming the raw infrared images to a known coordinate system aligned with the flow, as described in §5.3.1. The dewarped images contain the distribution of infrared intensity captured by the camera. The conversion from infrared intensity (or intensity counts) to temperature is done by applying a calibration, which depends both on the surface emissivity and the infrared sensor (exposure time, aperture...). This stage was skipped in the present investigation due to the small range of temperatures measured. In this context, the qualitative infrared intensity distribution can be assumed to resemble well the temperature one. For the static case, the BL state can be inferred from the infrared intensity distribution, and the LSB can be detected as described in §5.3.2. As this is no longer the case for an unsteady situation, a new methodology is required. The one proposed in this thesis is detailed in §5.3.3, as an extension of the DIT method for the case of a LSB. The thermal response of the surface in an unsteady aerodynamic situation is further studied in §5.3.4. An analytical model is proposed to compare the current investigation, involving the presence of a LSB, with existing research on DIT, as reviewed in §3.3.

#### 5.3.1. Marker tracking and image dewarping

The raw infrared images are dewarped by applying an image transformation constructed with the known location of fiducial markers. Eight markers were placed on the suction side of the wing, using the pressure taps as reference locations. Two rows of squared markers, separated by 100 mm along the span of the wing, were placed at  $x/c = 0.33, 0.49, 0.67, 0.84$ . These were made from copper tape and glued directly to the surface. Copper, like many other metals, has a very low emissivity in the infrared band, thus appearing darker in the infrared images. A raw image example is shown in Fig. 5.4(a). In this image, flow is approximately (due to camera viewing angle) from top to bottom, as indicated by the cyan arrow. The fiducial markers, surrounded by red circles, appear as dark squares in the image.

For a static situation, the automated detection of markers is based on the MATLAB function `detectMinEigenFeatures`. This function is used to detect the four corners of each marker by us-

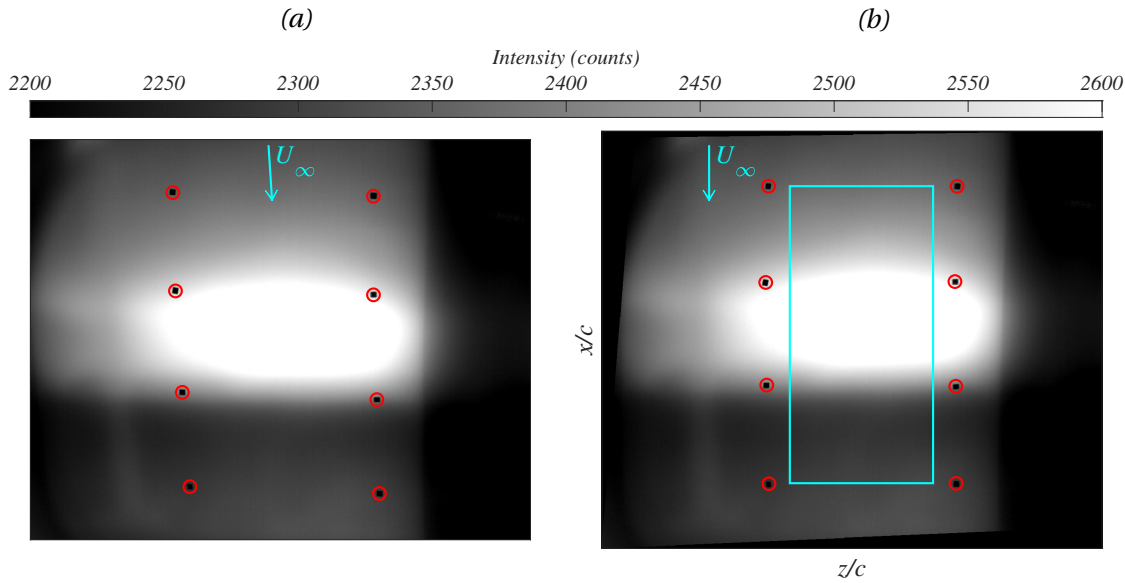


Figure 5.4: Infrared images containing the detected markers for image dewarping. (a) Raw image. (b) Transformed image, showing the rectangular region of interest.

ing the minimum eigenvalue algorithm, as introduced by Shi and Tomasi [68]. The centre of the square, obtained from the four detected corners, can be then used to define the marker location. The known and measured locations are used to construct a projective transformation using the function `fitgeotrans`. The application of the projective transformation, using the `imwarp` function, to the raw image example shown in Fig. 5.4(a) gives the dewarped image in Fig. 5.4(b). This image is now aligned with the flow in a coordinate system defined by the chord and spanwise directions ( $x - z$ ). The dewarped marker locations are used to define a rectangular region of interest (shown in cyan). This region, centred between the two rows of markers, has a width of 25% of the airfoil chord. The markers were placed such that the LSB is expected to always be inside this region. In the following, every infrared intensity distribution will be restricted to this region of interest.

The same projective transformation can be applied to all the images of a static acquisition. The obtained infrared intensity distributions are then time-averaged to reduce pixel noise. This simple approach is not applicable to an unsteady situation, where the wing moves relative to the infrared camera. For this type of acquisition, the first image of the set is manually supervised. When the marker detection is correct, the rest of the images are dewarped using the automated detection algorithm, allowing the markers to move a couple of pixels from frame to frame. A different projective transformation is constructed for each frame, but the rest of the process is analogous to the static situation.

In the pitching investigation, the infrared camera is triggered by the mechanism imposing the structural motion. This means that the first image of the acquisition already corresponds to the beginning of the constant pitching ramp. The motion frequency and acquisition frequency of the camera can be used to calculate the number of frames needed to capture the full ramp. The same information can be used to obtain the instantaneous angle of attack of each frame.

However, the infrared camera is not triggered for the plunging investigation. The acquisition is started manually after the oscillatory mechanism has achieved a constant operation, and therefore the location of the wing along the sinusoidal cycle is unknown. Due to the viewing angle of the infrared camera (to avoid self-reflection, see Fig. 4.6), the fiducial markers move from frame to frame in the raw images. The location of the markers can be linked to the phase angle of the wing along the cycle. Fig. 5.5 shows the wing position obtained from the location of one of the markers

during 1 s of acquisition. This illustrates the quality of the sinusoidal plunging motion and can be used to extract the motion frequency and assign a phase angle to each frame.

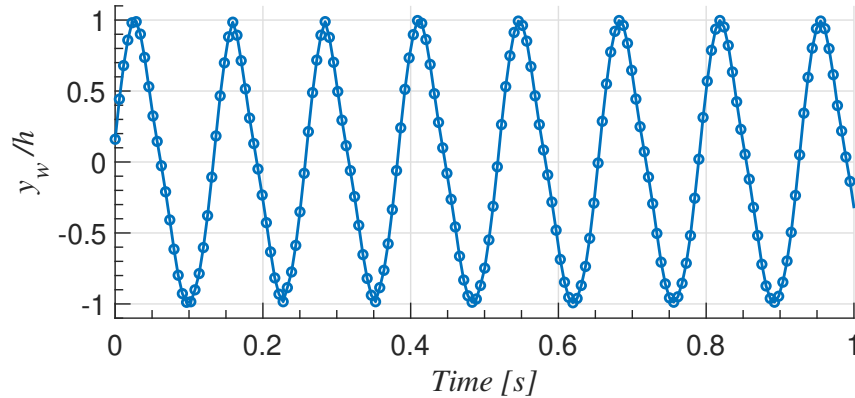


Figure 5.5: Wing position along the plunging cycle obtained from the location of a fiducial marker during 1 s of acquisition.

### 5.3.2. LSB location from temperature distributions

The detection of a LSB from steady-state temperature distributions (infrared intensity here) relies on some assumptions regarding the heat transfer processes involved. Two of these, convection with the flow and radiation exchange, have already been discussed and modelled by equations (3.3) and (3.8) respectively. There is a third relevant heat transfer source, which is conduction inside the wing structure. The heat flux by conduction ( $q_{cond}$ ) can be modelled using Fourier's law, as:

$$q_{cond} = -k_m \nabla T, \quad (5.3)$$

where  $k_m$  is the thermal conductivity of the wing's material and  $T$  is the temperature. In an unsteady situation, the temporal evolution of the temperature inside the wing can be obtained from solving the unsteady heat equation, written as:

$$\frac{\partial T}{\partial t} = \alpha_m \nabla^2 T, \quad (5.4)$$

where  $t$  is the time. To close the problem, the boundary condition at the surface (among other boundaries and an initial condition) needs to be imposed. This can be written as a balance between conduction into the structure, convection with the flow and radiation exchange with the environment (including possible external irradiation sources). This model is sketched Fig. 5.6. The unsteadiness of the heat transfer problem can be characterized by a Fourier number,  $Fo$ , expressed as:

$$Fo = \frac{\alpha_m t_c}{L_c^2}, \quad (5.5)$$

where  $t_c$  and  $L_c$  are characteristic time and length scales respectively. For a pitching or plunging wing situation, an appropriate time scale may be the time period of the motion (or inverse of the motion frequency), while the length scale represents the penetration depth of temperature changes.

In the present investigation, a simplification of the model is used. As for most aerodynamic problems, the surface exposed to the flow presents small resistance to convection and much higher resistance to conduction into the structure. This difference can be expressed using a Biot number,  $Bi$ , as:

$$Bi = \frac{h_s L_c}{k_m}. \quad (5.6)$$

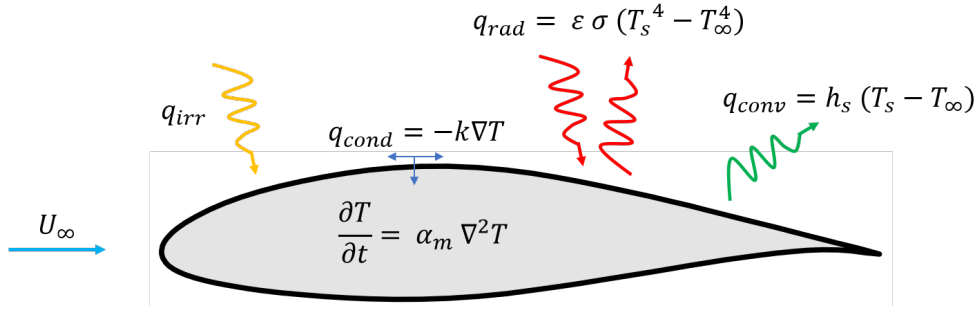


Figure 5.6: Heat transfer processes considered for the thermal modelling of an unsteady airfoil.

This means that  $Bi \gg 1$  usually holds for aerodynamic applications. This can be enhanced by choosing a material with low thermal conductivity (achieved here by adding a thin layer of thermal insulator at the surface). Under these circumstances, the effects of conduction can be neglected. This means that the airfoil surface behaves as a perfect insulator (Bergman and Lavine [5]) of thickness  $L$ . A second approximation considered here is to neglect the effect of radiation exchange. In the WT experiments, the surface is heated externally to increase its temperature with respect to the flow and thus enhance convection. However, this difference is kept small to prevent affecting the BL development. For small temperature differences, the radiation exchange between the surface and the outer environment mostly cancels out. In the end, the temperature of the perfect insulator is achieved from a balance between the incoming irradiation from the external heat source and convection with the flow, posting a similar thermal model as the one considered by von Hoesslin et al. [77, 78]. This can be written as:

$$\rho_m C_m L \frac{\partial T_s}{\partial t} = q_{irr} - h_s (T_s - T_\infty), \quad (5.7)$$

where  $\rho_m$  and  $C_m$  are the material density and heat capacity respectively. Here,  $q_{irr}$  represents the heat flux coming from the external irradiative source. For a steady-state situation, where  $\partial/\partial t = 0$ , equation (5.7) simplifies to:

$$T_s - T_\infty = \frac{q_{irr}}{h_s}. \quad (5.8)$$

For qualitative BL diagnostics, it is not necessary to obtain an estimation of the irradiation source. When the goal is to link the measured temperature distribution with convective heat transfer (or Stanton number, see equation (3.4)), equation (5.8) can be simplified to give a proportionality relation as:

$$St \propto \frac{1}{T_s - T_\infty}, \quad (5.9)$$

which indicates that changes in surface temperature are inversely proportional to those in Stanton number.

From this point, the thermal BL (characterized by  $St$ ) is usually linked to the momentum BL (characterized by skin friction) through the Reynolds analogy, as in equation (3.5). This can be used, for example, to detect the laminar-to-turbulent transition occurring over an aerodynamic surface. It is well-known that skin friction increases significantly due to the transition process (see for example White [82] or Fig. 3.1 for the case of a flat plate) and the Reynolds analogy predicts a similar increase in heat transfer. Thus, the effect of transition on surface temperature appears as a sharp temperature descent if the surface is warmer than the flow. Similarly, temperature is expected to continuously increase along with the streamwise direction for BL flows as this gets thicker.

However, the Reynolds analogy does not hold for separated flows. This means that no prior knowledge of the behaviour of heat transfer inside a LSB can be easily extracted from the theory.

As suggested by Wynnchuk and Yarusevych [86], the approach considered here is to follow the observations from Spalart and Strelets [70], who conducted a Direct Numerical Simulation (DNS) for the case of a LSB, showing the comparison between skin friction and Stanton number distributions. The evolution of skin friction ( $C_f$ ) and Stanton number ( $St$ ) along the streamwise direction is reproduced in Fig. 5.7. Also, the evolution of BL thicknesses (displacement and momentum) were extracted from the study and used to construct the BL shape factor ( $H$ ) following equation (5.2), as shown in the figure.

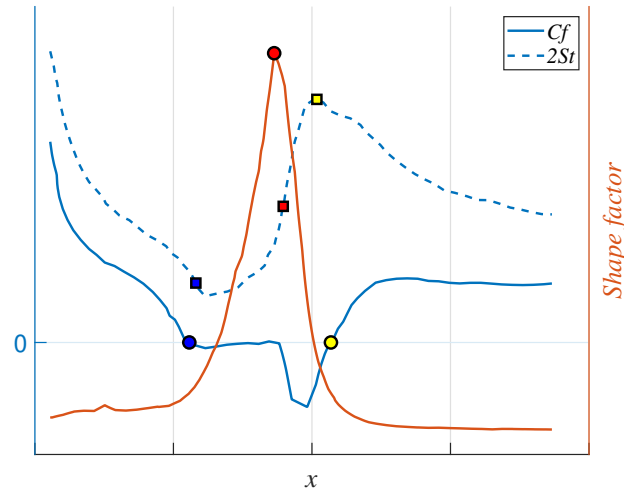


Figure 5.7: Evolution of skin friction, Stanton number and BL shape factor in the presence of a LSB. Results adapted from Spalart and Strelets [70].

The analysis of the momentum BL ( $C_f$  and  $H$ ) gives the description of the LSB. The location of laminar separation occurs where skin friction vanishes (blue circle in Fig. 5.7). Similarly, reattachment of the turbulent BL is found at the location where skin friction becomes positive again (yellow circle). The transition process is here estimated to occur at the location of maximum BL shape factor (red circle), as considered in the PIV analysis.

As expected, the evolution of the Stanton number shows a big discrepancy with respect to the prediction of the Reynolds analogy inside the bubble. It can be seen how  $St$  decreases as the initial laminar BL gets thicker and continues to decrease in the initial portion of the bubble. The location of flow separation coincides with the strongest decrease rate of Stanton number (blue square). The transition process in the separated shear layer induces near-wall velocity fluctuations and reverse flow, thus enhancing convection.  $St$  achieves a minimum inside the bubble and starts to increase by the effect of transition. The transition location coincides with the strongest increase rate in heat transfer (red square). This description is analogous to that of BL transition commonly used in IT investigations. The turbulent BL formed in the shear layer reattaches and then starts to grow downstream of the reattachment location. It can be seen how heat transfer reaches a maximum at this location (yellow square), followed by a shallow decrease as the BL gets thicker.

The behaviour of  $St$  can be linked to surface temperature through equation (5.9). This means that the laminar separation location is estimated to occur for maximum temperature increase, transition at the strongest temperature decay and turbulent reattachment where surface temperature reaches a local minimum. This confirms that, to detect a static LSB, it is sufficient to obtain the qualitative evolution of surface temperature. This simplifies the experimental setup, as no thermal calibration of the infrared camera is required as long as temperature changes are sufficiently small.

This approach is illustrated here for a static example, at  $\alpha = 2^\circ$ . The top part of Fig. 5.8 shows

contours of time-averaged infrared intensity inside the region of interest introduced above. Along the span, a circular pattern can be observed, which is caused by the uneven heating of the circular heat lamp (see Fig. 4.6). Along the chord of the airfoil, the temperature changes resemble well the expected behaviour from the simulations of Spalart and Strelets [70]. From left to right, temperature rises as the laminar BL gets thicker, reaching a maximum inside the bubble. Then, temperature starts to drop until the turbulent BL reattaches. Lastly, a slight increase is observed as the reattached BL evolves.

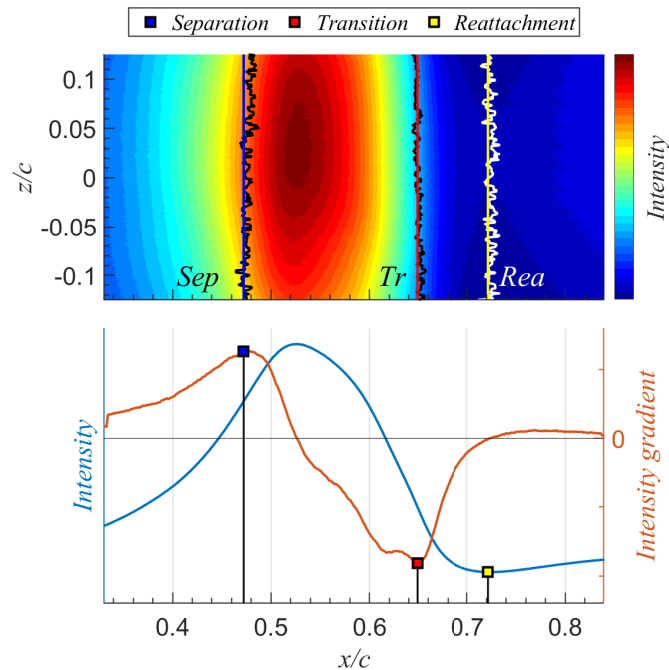


Figure 5.8: Contours of time-averaged infrared intensity (top) and spanwise-averaged infrared intensity and intensity gradient distributions along the chord (bottom) for the static wing at  $\alpha = 2^\circ$ .

The LSB characteristic locations (*Sep*, *Tr* and *Rea* in the figure), estimated as maximum increase rate, maximum decrease rate and local minimum respectively for every pixel row along the span, are indicated by black and white lines (colours changed for improved visualization). These indicate a two-dimensional LSB, with less than 1% of the chord scatter along the span in the region measured. This confirms that the uneven heating from the external lamp has very little effect on the detected locations, and serves only to enhance temperature changes along the chord.

The observed two-dimensionality of the flow motivates the spanwise-averaging of the infrared intensity distribution. The obtained curve along the chord of the airfoil is shown in the bottom part of Fig. 5.8. The numerical gradient of the intensity curve is also shown to better visualize the detection of the characteristic locations. The values obtained from the spanwise-averaged approach (indicated by coloured squares) are also included in the top part of the figure as coloured lines, showing good agreement with the previous version. Based on this result, the spanwise-averaged approach is the one considered in the remaining of the thesis to estimate the characteristic locations of the LSB for static situations.

### 5.3.3. Differential Infrared Thermography approach

Trying to detect the location of a LSB in an unsteady situation using the previous approach will fail for most situations. In general, the thermal response of the aerodynamic surface is much slower than the aerodynamic unsteadiness. This means that an instantaneous surface temperature distribution may not be representative of the actual BL state. Instead, it will be a combination of past

situations. To overcome this limitation, a Differential Infrared Thermography (DIT) approach will be used.

This procedure, introduced for unsteady conditions, can be also used to detect static transition, as shown by Wolf et al. [84]. Here, a static DIT example will be given for simplicity, but the approach would be analogous for an unsteady situation. The static DIT method consists of subtracting steady-state temperature distributions from the wing at two different angles of attack,  $\alpha_1$  and  $\alpha_2$ , to obtain information about the transition process at the intermediate incidence  $\alpha$ , as  $\alpha = (\alpha_1 + \alpha_2)/2$ . The values chosen for the example given here are  $\alpha_1 = 1.5^\circ$  and  $\alpha_2 = 2.5^\circ$ , so that  $\alpha = 2^\circ$ , the example shown earlier for the static IT approach. The top part of Fig. 5.9 shows contours of the difference in time-averaged infrared intensity between  $\alpha_1$  and  $\alpha_2$  (obtained as intensity at  $\alpha_2$  minus intensity at  $\alpha_1$ ). From the DIT method, transition at  $\alpha = 2^\circ$  is expected to occur when the difference achieves a peak. As the LSB moves upstream from  $\alpha_1$  to  $\alpha_2$ , a negative peak is to be expected. The local minimum obtained at each pixel row along the span is indicated in the figure by a white line.

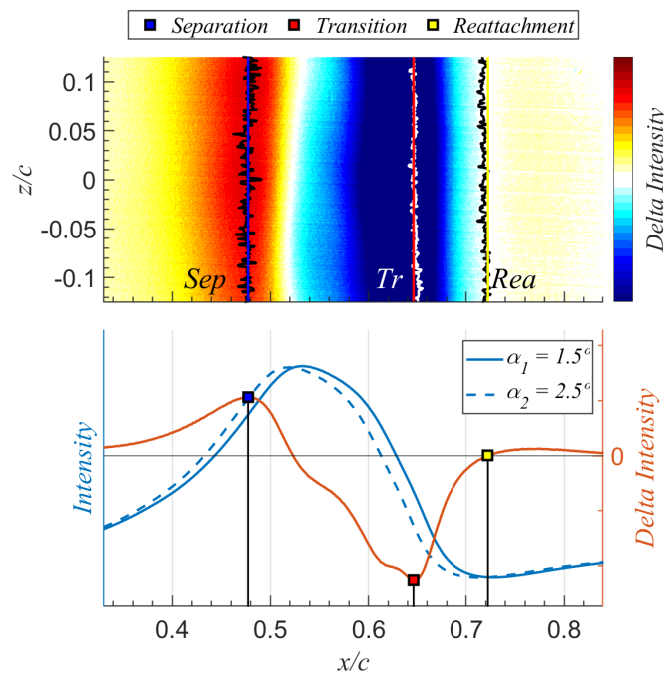


Figure 5.9: Contours of the difference in infrared intensity between  $\alpha_1 = 1.5^\circ$  and  $\alpha_2 = 2.5^\circ$  (top) and spanwise-averaged infrared intensity and DIT distributions along the chord (bottom).

The novel approach proposed in this thesis is to extend the DIT method not only to detect BL transition but also the locations of laminar separation and turbulent reattachment. For separation, the argument is analogous to that of transition, but the expected DIT peak will always be of the opposite sign. This means that, for a bubble moving upstream as in the example shown here, separation is expected to occur at the positive DIT peak. This location, obtained at each pixel row along the span, is shown in the top part of Fig. 5.9 with a black line.

As discussed in the previous section, the location of turbulent reattachment causes a local minimum in the temperature distribution. This means that the local minimum will also move upstream between  $\alpha_1$  and  $\alpha_2$ . The local minimum at  $\alpha = 2^\circ$  is expected to occur in between those two. For a small difference between  $\alpha_1$  and  $\alpha_2$ , this will be when those curves intersect. In other words, when the DIT signal between  $\alpha_1$  and  $\alpha_2$  is zero in this region. This estimation is also shown in the top part of Fig. 5.9 with a black line.

As for the static case, the three lines indicating the characteristic locations of the LSB represent a two-dimensional situation. This again justifies the spanwise-averaging of the measurements. The

spanwise-averaged infrared intensities measured at  $\alpha_1$  and  $\alpha_2$  are shown in the bottom part of Fig. 5.9. The DIT curve obtained from the subtraction of spanwise-averaged infrared intensities is also shown in the figure. The LSB characteristic locations, estimated from the positive peak, negative peak and zero value of the DIT signal are indicated by coloured squares. These locations are also shown in the top part of the figure as coloured lines and agree well with the solution obtained prior to the spanwise-averaging. As for the static IT case, the DIT curves shown in the thesis will use spanwise-averaging to reduce pixel noise.

There is a strong similarity between the DIT curve shown in Fig. 5.9 and the infrared intensity gradient shown in Fig. 5.8. This is precisely the purpose of DIT: recover information from the steady-state temperature distribution (in this case its gradient) when it cannot be measured due to the thermal lag of the surface. In an unsteady situation, like the ones that will be discussed in the next chapter, the DIT curve can be constructed in an analogous manner. All the information available will be unsteady infrared intensity distributions, and their subtraction will be used to generate DIT curves representative of the BL state at the intermediate angle of attack.

#### 5.3.4. Thermal response of an unsteady airfoil

So far, all of the DIT development has been made around the aerodynamic environment of a helicopter rotor, as presented in §3.3 from the DLR work. If the goal is to consider the technique for the case of a LSB, seems reasonable to make a comparison between the two situations. The idea is to recreate an experimental DIT measurement from a numerical approach. A thermal model at the wing surface can be used to recreate the heat transfer processes involved and therefore simulate the surface temperature that can be measured with an infrared camera. The unsteady model considered is the one described by equation (5.7), which neglects the effects of conduction and radiation. The material properties considered in this study are extracted from the numerical DIT investigation conducted by Gardner et al. [18], representative of a carbon fiber-epoxy combination. These can be consulted in Table 5.1.

Table 5.1: Simulation parameters from Gardner et al. [18]

$U_\infty$	90 m/s
$C_m$	2300 J/Kg/K
$\rho_m$	1180 Kg/m <sup>3</sup>
$L$	0.2 mm

For a generic unsteady situation, where  $h_s$  is a function of time, no general analytical solution may be found for equation (5.7). To overcome this limitation, a simpler unsteady problem is considered. The thermal simulation starts from a steady-state condition, referred to as *initial*, followed by a sudden change in incidence to reach a *final* state. This causes an immediate change in the convective heat transfer distribution. The surface temperature does not respond instantaneously to this change, but follows the description of equation (5.7) where now  $h_s$  corresponds to the *final* state distribution. This means that  $T_s$  is the only function of time, simplifying the approach.

The next step is to find the surface temperature and convective heat transfer coefficient distributions along the chord of the airfoil (in the streamwise direction  $x$ ) for the *initial* and *final* states, both for the DLR and UA situations. For the DLR case, skin friction coefficient distributions at two different angles of attack are considered, as reproduced in Fig. 5.10. The red curve corresponds to the *initial* state while the green curve corresponds to the *final* one, as the increase in incidence causes an upstream movement of the transition location.

Stanton number distributions are obtained using the Reynolds analogy, equation (3.5). From there,  $h_s$  distributions can be obtained considering equation (3.4), air properties and freestream speed as listed in Table 5.1. A constant irradiation heat flux is considered to maintain the maximum

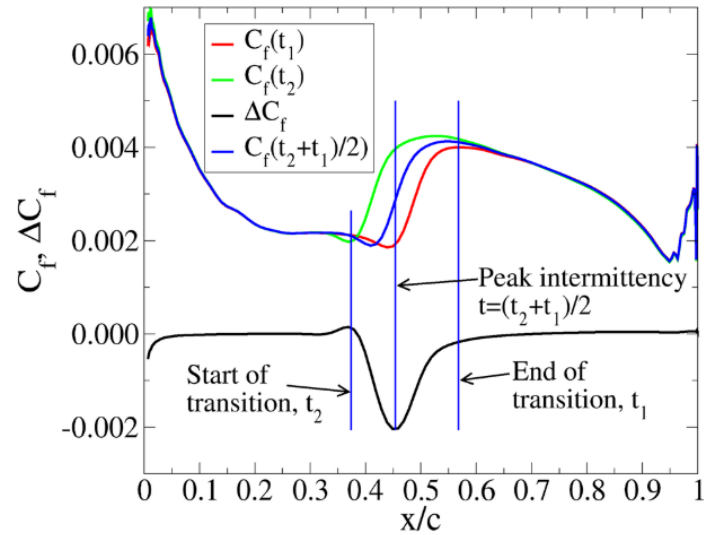


Figure 5.10: Skin friction coefficient distributions on the suction side of a DSA-9A airfoil at two different incidence angles. Results reproduced from Gardner et al. [18].

surface temperature below 10 K above ambient, as discussed in [18]. With that, the *initial* and *final* surface temperature distributions can be obtained from equation (5.8).

For the case of a LSB studied in the WT experiments at UA, the available information are surface temperature distributions measured with the infrared camera. Only for this investigation, the factory calibration of the camera was used to link infrared intensity to surface temperature. Similarly to the DLR case, two angles of attack are considered, with the incidence of the *final* state being higher than the one of the *initial* state. The surface temperature distributions (from time- and spanwise-averaged measurements for the UA case) considered for both situations and states may be consulted in Fig. 5.11 (a).

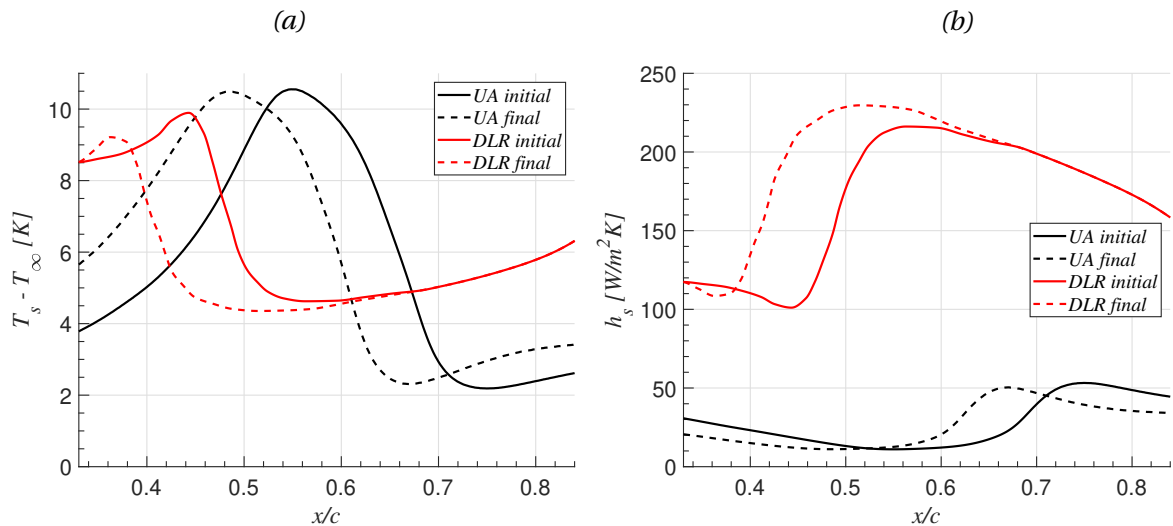


Figure 5.11: Distributions considered for the unsteady thermal model, following DLR results from Gardner et al. [18] and experiments conducted at UA. (a) Surface temperature. (b) Convective heat transfer coefficient.

Skin friction coefficient distributions are obtained for the UA case using XFOIL simulations at the known angles of attack. The viscous solution is obtained with the  $e^N$  method for transition prediction (Van Ingen [75]), using a critical  $N$ -factor of 10, according to the UA wind tunnel charac-

teristics (Borgmann et al. [7]). The Reynolds analogy can be applied to the laminar part of the flow close to the leading edge of the wing and find from there the constant irradiation heat flux that keeps the maximum temperature around 10 K above ambient. Finally,  $h_s$  distributions may be obtained after rearranging equation (5.8). The obtained results for both situations and states are shown in Fig. 5.11(b). The comparison between Figs. 5.11(a) and 5.11(b) illustrates a key difference between the DLR and UA situations. While the surface temperature values are comparable, convective heat transfer is an order of magnitude higher for the DLR case mainly due to the increased Reynolds number considered.

In order to solve equation (5.7), an initial condition (at  $t = 0$ ) is needed. This represents the surface temperature distribution in the *initial* state. On the other hand, the convective heat transfer coefficient distribution of the *final* state is considered, and equation (5.7) gives the evolution of surface temperature from the *initial* to the *final* state, achieved when  $t \rightarrow \infty$ . To integrate the equation in time, a change of variables is required. Introducing a temperature difference,  $\theta$ , as  $\theta = T_s - T_\infty$ , and noting that  $\partial\theta/\partial t = \partial T_s/\partial t$ , equation (5.7) reduces to:

$$\rho_m C_m L \frac{\partial\theta}{\partial t} = q_{irr} - h_s \theta, \quad (5.10)$$

which can be rearranged as:

$$\frac{\partial\theta}{\partial t} + \frac{h_s}{\rho_m C_m L} \theta - \frac{q_{irr}}{\rho_m C_m L} = 0. \quad (5.11)$$

It is now helpful to define two auxiliary constants,  $C_1$  and  $C_2$ , as:

$$C_1 = \frac{h_s}{\rho_m C_m L}, \quad (5.12a)$$

$$C_2 = \frac{q_{irr}}{\rho_m C_m L}. \quad (5.12b)$$

Introducing these definitions, equation (5.11) simplifies to:

$$\frac{\partial\theta}{\partial t} + C_1 \theta - C_2 = 0, \quad (5.13)$$

which is a simple non-homogeneous first-order linear differential equation. One easy way of solving it is to make it homogeneous by introducing an auxiliary variable,  $\theta'$ , as  $\theta' = \theta - C_2/C_1$ . Noting that  $\partial\theta'/\partial t = \partial\theta/\partial t$ , equation (5.13) can be expressed as:

$$\frac{\partial\theta'}{\partial t} + C_1 \theta' = 0, \quad (5.14)$$

which can now be integrated in time by separation of variables, from  $t = 0$  to  $t$ , as:

$$\int_{t=0}^t \frac{d\theta'}{\theta'} = \int_{t=0}^t -C_1 dt, \quad (5.15a)$$

$$\frac{\theta'(t)}{\theta'(0)} = e^{-C_1 t}. \quad (5.15b)$$

Undoing the change of variables, this gives:

$$\frac{\theta(t) - C_2/C_1}{\theta(0) - C_2/C_1} = e^{-C_1 t}, \quad (5.16a)$$

$$\frac{T_s(t) - T_\infty - C_2/C_1}{T_s(0) - T_\infty - C_2/C_1} = e^{-C_1 t}. \quad (5.16b)$$

Finally, substituting equations (5.12a) and (5.12b) into equation (5.16b) gives:

$$T_s(t) - T_\infty = \frac{q_{irr}}{h_s} + e^{-\frac{h_s t}{\rho_m C_m L}} \left( T_s(0) - T_\infty - \frac{q_{irr}}{h_s} \right). \quad (5.17)$$

It can be easily checked that the initial surface temperature distribution is obtained when  $t = 0$ , while it reduces to equation (5.8) as  $t \rightarrow \infty$ , considering  $h_s$  to be the distribution of the *final* state.

The DIT method proposed by DLR consists of subtracting two surface temperature distributions shortly separated in time. In this numerical investigation, a *DIT signal* may be constructed from  $DIT\ signal = T_s(t) - T_s(0)$ , for  $t \ll 1$ . For small simulation times  $t$ , the exponential term inside equation (5.17) may be linearized as:

$$e^{-\frac{h_s t}{\rho_m C_m L}} = 1 - \frac{h_s t}{\rho_m C_m L} + O(t^2). \quad (5.18)$$

Inserting this approximation in equation (5.17) gives:

$$T_s(t) - T_\infty \approx T_s(0) - T_\infty - \frac{h_s t}{\rho_m C_m L} \left( T_s(0) - T_\infty - \frac{q_{irr}}{h_s} \right), \quad (5.19)$$

which can be rearranged to obtain the *DIT signal* as:

$$DIT\ signal = T_s(t) - T_s(0) \approx -\frac{h_s t}{\rho_m C_m L} \left( T_s(0) - T_\infty - \frac{q_{irr}}{h_s} \right). \quad (5.20)$$

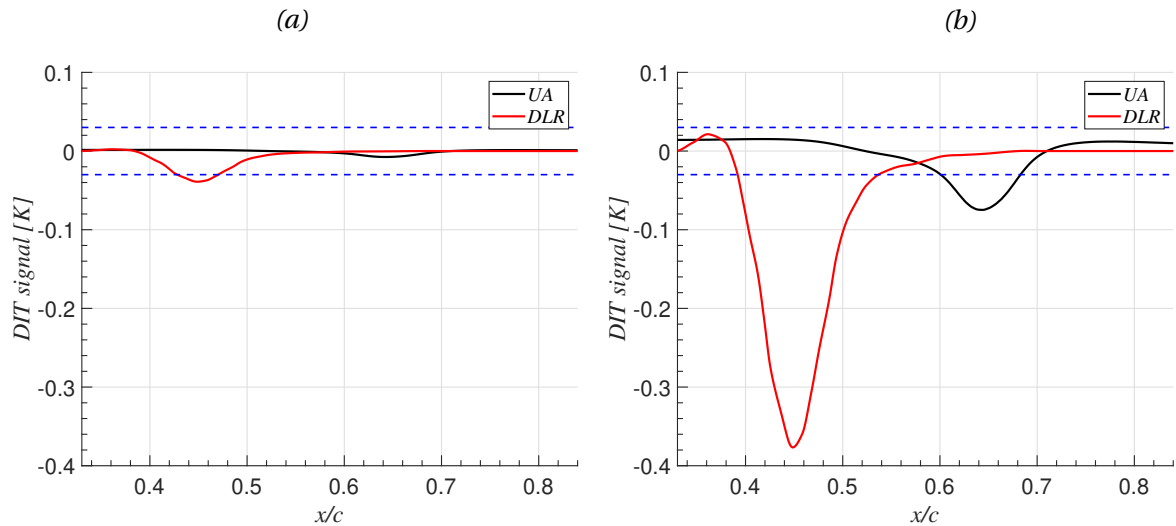


Figure 5.12: *DIT signal* obtained from the thermal model, for both the DLR and UA situations. (a) For a simulation time of  $t = 10^{-2}$  s. (b) For a simulation time of  $t = 10^{-1}$  s. The dashed blue lines represent the thermal sensitivity of typical modern infrared cameras.

The obtained signal is shown in Fig. 5.12 for both situations. The curves shown in Fig. 5.12(a) are obtained for  $t = 10^{-2}$  s, while the ones given in Fig. 5.12(b) are obtained for  $t = 10^{-1}$  s. Both figures include dashed blue lines at  $\pm 30$  mK, representative of the thermal sensitivity of state-of-the-art infrared cameras. This means that only the information outside of this band can be expected to be detectable in an experiment. All curves shown have a distinct negative peak, indicative of the BL transition location moving upstream from the *initial* to the *final* states. As discussed by DLR, the peak location corresponds to the transition location at an intermediate incidence. Even if this peak is visible for both situations, its strength is much stronger for the DLR case. Due to the reduced heat transfer, the surface reacts much slower for the case of a LSB. This means that a bigger time difference between thermograms will need to be used in the experiments in order to detect the

DIT peak, which can cause erroneous results as discussed by Gardner et al. [18]. For the LSB case, another DIT peak, of opposite sign, is expected to occur. This is linked to the laminar separation location, but the strength of it is much smaller, according to Fig. 5.12. Changes in heat transfer are weaker in this region (see Fig. 5.11(b)), further limiting the thermal response. Similarly, no information outside of the dashed blue lines is observed in the reattachment region. This analysis indicates that the detection of laminar separation and turbulent reattachment is expected to be significantly more challenging than that of transition from the experimental measurements.

A quick variation of the model can be done to study the difference between the existing increasing incidence simulation (representative of a pitch up situation), to the case where incidence reduces (pitch down). This can be done by changing the *initial* and *final* distributions introduced in equation (5.20). The comparison between both conditions can be found in Fig. 5.13. The curves shown in Fig. 5.13(a) are obtained for  $t = 10^{-2}$  s, while the ones given in Fig. 5.13(b) are obtained for  $t = 10^{-1}$  s. Again, the figures include dashed blue lines at  $\pm 30$  mK, representative of the thermal sensitivity of state-of-the-art infrared cameras. For the pitch down condition, the BL transition location moves downstream, thus appearing as a positive peak in the *DIT signal*. It is interesting to see that, for equal simulation times, the peak of the pitch up condition has more than double the strength of the pitch down one. This result is closely related to the  $h_s$  distributions shown in Fig. 5.11(b). At the intermediate transition location (DIT peak), the BL is initially laminar in the pitch up simulation. The sudden increase in incidence causes transition to move upstream, and therefore the BL becomes turbulent at the DIT peak location. The change from laminar to turbulent causes an increase in convective heat transfer, making the surface react faster. This indicates that a longer time separation between thermograms will be needed for a pitch down condition, again having detrimental effects on the results.

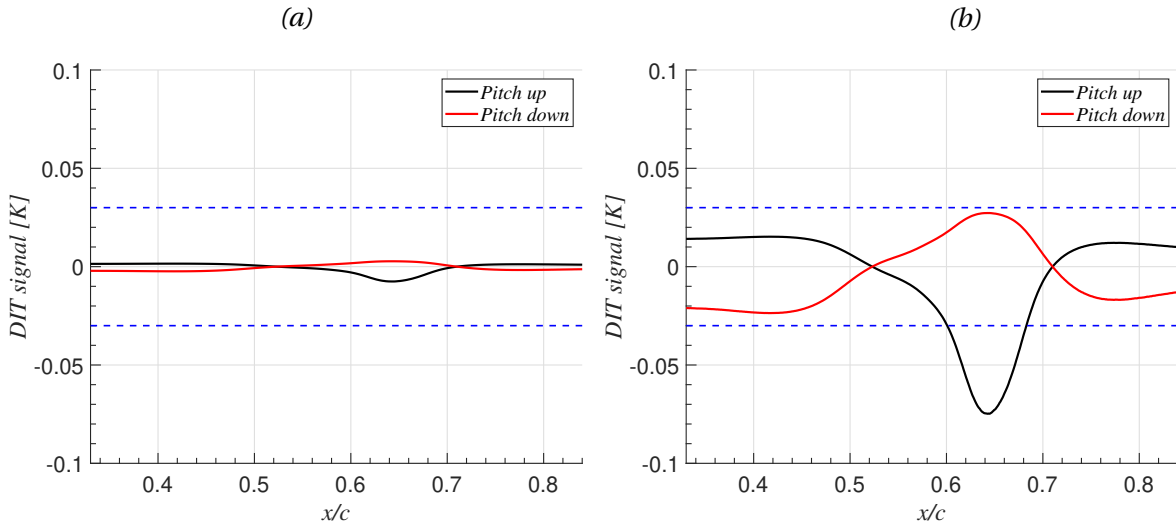


Figure 5.13: *DIT signal* obtained from the thermal model for the case of a LSB, for pitch up and pitch down conditions. (a) For a simulation time of  $t = 10^{-2}$  s. (b) For a simulation time of  $t = 10^{-1}$  s. The dashed blue lines represent the thermal sensitivity of typical modern infrared cameras.

A better characterization of the parameters governing the unsteady thermal response of the aerodynamic surface may be obtained from rearranging equation (5.20) into:

$$DIT\ signal = T_s(t) - T_s(0) \approx -\frac{h_s t}{\rho_m C_m L} (T_s(0) - T_\infty) + \frac{q_{irr} t}{\rho_m C_m L}. \quad (5.21)$$

It is important to recall that  $h_s$  refers here to the *final* state. On the other hand, the *initial* convective heat transfer distribution can be linked to the irradiative heat flux from the steady-state solution,

equation (5.8), as:

$$q_{irr} = h_s(\text{initial}) (T_s(0) - T_\infty). \quad (5.22)$$

Introducing this result in equation (5.21) gives:

$$DIT \text{ signal} \approx -\frac{h_s(\text{final}) t}{\rho_m C_m L} (T_s(0) - T_\infty) + \frac{h_s(\text{initial}) t}{\rho_m C_m L} (T_s(0) - T_\infty), \quad (5.23)$$

which can be rearranged into:

$$\frac{DIT \text{ signal}}{T_s(0) - T_\infty} \approx -\frac{t}{\rho_m C_m L} (h_s(\text{final}) - h_s(\text{initial})). \quad (5.24)$$

This relative signal achieves its peak at the location where convective heat transfer changes most between thermograms. In the problem of interest, this is caused by the change in heat transfer between laminar and turbulent BLs. For a more general situation, this characteristic change in heat transfer can be called  $h_c$ . Considering now an unsteady problem of characteristic time scale  $t_c$ , equation (5.24) establishes a balance as:

$$\frac{DIT \text{ signal}}{T_c - T_\infty} \sim \frac{t_c h_c}{\rho_m C_m L}, \quad (5.25)$$

where  $T_c$  is the characteristic temperature of the surface of interest. After some manipulation, this relation can be expressed in terms of two non-dimensional numbers discussed previously, as:

$$\frac{DIT \text{ signal}}{T_c - T_\infty} \sim \frac{t_c h_c}{\rho_m C_m L} = \frac{k_m}{\rho_m C_m} \frac{t_c h_c L}{L^2 k_m} = \alpha_m \frac{t_c}{L^2} Bi = Fo Bi, \quad (5.26)$$

where the thermal diffusivity has been expressed in terms of other material properties. Please note that the definition of the Biot number has changed slightly with respect to the one in equation (5.6). Now, the characteristic convective heat transfer coefficient refers to the change between laminar and turbulent BLs. In the current discussion, an estimate of it can be obtained from Fig. 5.11(b), by subtracting the maximum and minimum values observed for each of the situations. In this thesis, the unsteadiness of the motions explored are characterized by their frequency,  $f$ . This can be expressed as the inverse of the characteristic time scale. Introducing this modification in equation (5.26) finally gives:

$$\frac{DIT \text{ signal}}{T_c - T_\infty} \sim Fo Bi = \frac{h_c}{\rho_m C_m L f}. \quad (5.27)$$

For a final comparison between the unsteady situations explored by DLR and the case of a LSB tackled at UA, the governing non-dimensional group  $Fo Bi$  is obtained for both and shown together in Fig. 5.14. This includes results from two experiments conducted by the DLR group, as reported by Richter et al. [65] and Wolf et al. [84]. The dashed black line represents the minimum  $Fo Bi$  value for which the DIT approach has been shown to work. The curves corresponding to the experiments conducted at UA include the two types of motion that are considered in the thesis.

This comparison suggests that, due to the lower convective heat transfer levels for the case of a LSB, the maximum motion frequency could be limited to a value below the ones tested by DLR. All the experimental setpoints above the dashed black line are expected to be successful, while the ones below the line are unexplored territory. This procedure does not include the distinction between pitch up and pitch down investigations. That effect is included in the term  $T_c - T_\infty$  in equation (5.27) and can also have a significant effect as visualized in Fig. 5.13.

To isolate the effect that convective heat transfer will have on the LSB case, material properties have been kept constant through the analysis. However, the importance of choosing a suitable material must be highlighted. According to equation (5.27), material properties (density, heat capacity

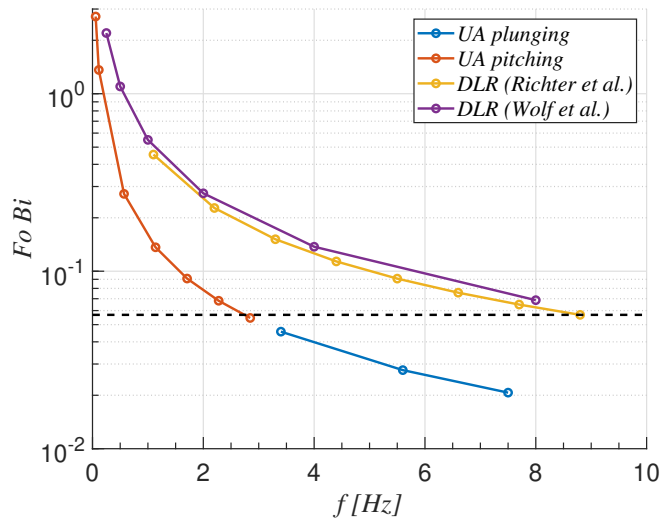


Figure 5.14: Comparison of the non-dimensional group  $FoBi$  between the experiments of Richter et al. [65], Wolf et al. [84] and the ones at UA.

and thickness) are as relevant as heat transfer changes or motion frequency, as all of them have a linear influence on the non-dimensional group that governs the unsteady response of the surface. By combining the three, a profound effect can be made. While the assumption of perfect insulation is still valid, this numerical approach indicates that a thin surface with low thermal capacity is the ideal choice for DIT applications.



# 6

## Results

The results presented in this chapter cover the experimental investigations on the modified NACA 64<sub>3</sub> – 618 airfoil at a chord-based Reynolds number of  $Re = 200,000$ . The LSB that forms on the suction side of the wing is studied using three different flow measurement techniques: surface pressure measurements (pressure taps and a pressure transducer), PIV and IT. The LSB may be detected from these experimental measurements employing the methods described in chapter 5. This chapter is divided into the three experiments conducted in the ALSWT: a static characterization of the wing over a range of angles of attack, a pitching unsteady motion and finally a plunging configuration.

The static results, discussed in §6.1, characterize the LSB at every incidence angle that will later appear in the unsteady situations. The pitching motion imposed consists of ramps of constant pitching rate, such that the incidence of the wing is of the form:  $\alpha = 2^\circ \pm 5^\circ$ . The pitching rate is varied to study different levels of unsteadiness, but the incidence is maintained. The plunging set-point discussed here, defined by  $h = 6\%$  and  $k = 0.67$ , induces a range of effective angles of attack between  $-4.56^\circ \leq \alpha_{eff} \leq 4.56^\circ$ . To cover both conditions, the static wing is studied, using one-degree increments, between  $-5^\circ \leq \alpha \leq 7^\circ$ .

The pitching experiment was designed to prove the capability of DIT to detect an unsteady LSB. The results, discussed in §6.2, are organized according to the three techniques available. The pitching rate of the motion is varied to study the effect that this has on the bubble but also to find the limitations of the DIT method. This includes from quasi-steady situations to more complex unsteady conditions. The effect that the unsteadiness has on the bubble and the infrared technique is illustrated by comparing key results from all frequencies tested.

The plunging experiment constitutes a more complex situation, especially for the infrared approach. A plunging-type motion cannot totally separate frequency from amplitude (in terms of effective angle of attack). To study a similar incidence range to the pitching case (approximately 9 degrees for the plunging case and 10 for the pitching one), a high frequency is needed, with the given motion amplitude that the plunging mechanism provides. This complicates the infrared approach, constituting a more challenging experiment. From the sinusoidal cycle, four phases are chosen to show the evolution of the LSB, as discussed in §6.3. This is again illustrated by showing results from the three techniques available.

### 6.1. Static LSB characterization

This section presents the results of the static characterization of the LSB on the suction side of the wing, covering a range of angles of attack from  $-5^\circ \leq \alpha \leq 7^\circ$ . First, in §6.1.1, the nature and the effect that incidence has on the bubble's size and location are discussed from the pressure transducer and pressure taps results respectively. Then, the static PIV measurements are presented in §6.1.2, while

§6.1.3 covers the infrared approach. For this technique, both the static IT and DIT methods are considered, as introduced in §5.3.2 and §5.3.3 respectively, to further motivate the exploration of DIT for the unsteady situations. Finally, the comparison between the three techniques, given in terms of bubble location, is discussed in §6.1.4.

### 6.1.1. Surface pressure measurements

Static pressure coefficient distributions already reveal the presence of a LSB on the suction side of the wing. Fig. 6.1(a) shows  $c_p$  distributions for the static wing at  $\alpha = 0^\circ, 2^\circ, 4^\circ$  and  $6^\circ$ . Together with the experimental results, XFOil predictions for the static airfoil are included for comparison. The viscous solution is obtained with the  $e^N$  method for transition prediction (Van Ingen [75]). The appropriate critical  $N$ -factor is obtained following the method of Mack [46], which relates the critical  $N$ -factor to the turbulence intensity in the wind tunnel by:

$$N = -8.43 - 2.4 \ln(Tu). \quad (6.1)$$

Using the known values for the ALSWT at the conditions considered here gives an approximate value of  $N = 10$ . The pressure coefficient reveals the presence of a LSB on the suction side of the airfoil within the region  $0.45 \lesssim x/c \lesssim 0.75$ , as indicated by the pressure plateau. The agreement between experiments and XFOil is excellent except in the reattachment region. XFOil predicts a slightly shorter bubble, which could be due to a mismatch in the freestream turbulence levels. The LSB is observed to move upstream with increasing  $\alpha$ , which is in agreement with the general trends found in the literature. The stronger adverse pressure gradient causes an earlier separation of the laminar BL, while the size of the bubble is mainly driven by the stability of the shear layer.

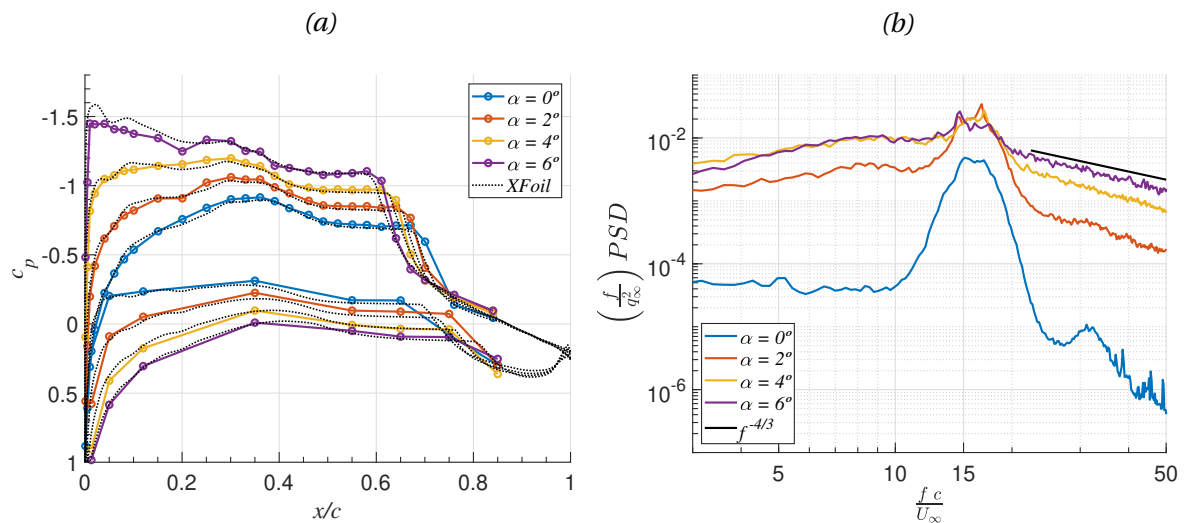


Figure 6.1: (a)  $c_p$  distributions for the static wing at  $\alpha = 0^\circ, 2^\circ, 4^\circ$  and  $6^\circ$ . (b) Frequency-premultiplied non-dimensional Power Spectral Density (PSD) of pressure fluctuations at  $x/c = 0.65$  at the same angles of attack.

The nature of the transition and subsequent reattachment processes is further studied with the high-bandwidth pressure transducer installed on the suction side of the airfoil at  $x/c = 0.65$ . Frequency-premultiplied Power Spectral Density (PSD) of the measured pressure fluctuations are shown in Fig. 6.1(b) for the same range of angles of attack. The spectra reveal the amplification of disturbances in the separated shear layer, within a band of frequencies centred at a chord-based Strouhal number of  $f c / U_\infty \approx 15$ . An inviscid Kelvin-Helmholtz instability is argued to be responsible for the disturbance amplification (Watmuff [80]). This was confirmed by comparison with the high-fidelity simulations described by Hosseinverdi and Fasel [35], as discussed in Grille Guerra et al. [28]. The upstream movement of the LSB with increasing  $\alpha$  means that the sensor location

moves from the transition region at  $\alpha = 0^\circ$  to the reattached turbulent boundary layer at  $\alpha = 6^\circ$ , which explains the general increase in PSD level (Yarusevych et al. [87]). The agreement with the theoretical turbulent decay (-4/3 slope in frequency-premultiplied form for pressure) improves as the sensor moves into the turbulent boundary layer.

The characteristic locations of the LSB (laminar separation, transition and turbulent reattachment) can be estimated from the  $c_p$  distributions following the methodology described in §5.1. This consists of creating linear fits from certain parts of the  $c_p$  distribution and finding the desired locations from the intersection of those, to try and improve the spatial resolution of the technique. This is applied to  $\alpha = -5^\circ, 0^\circ$  and  $7^\circ$  as shown in Fig. 6.2(a). The same static angles of attack will be later considered for the other techniques (PIV and IT) for a direct comparison between them. For improved visualization, only the static pressure coefficient suction side distributions are shown in the figure. This indicates again the upstream shift of the bubble with increasing incidence, but also illustrates the limitation of the technique for negative  $\alpha$  due to the poor distribution of pressure taps closer to the trailing edge.

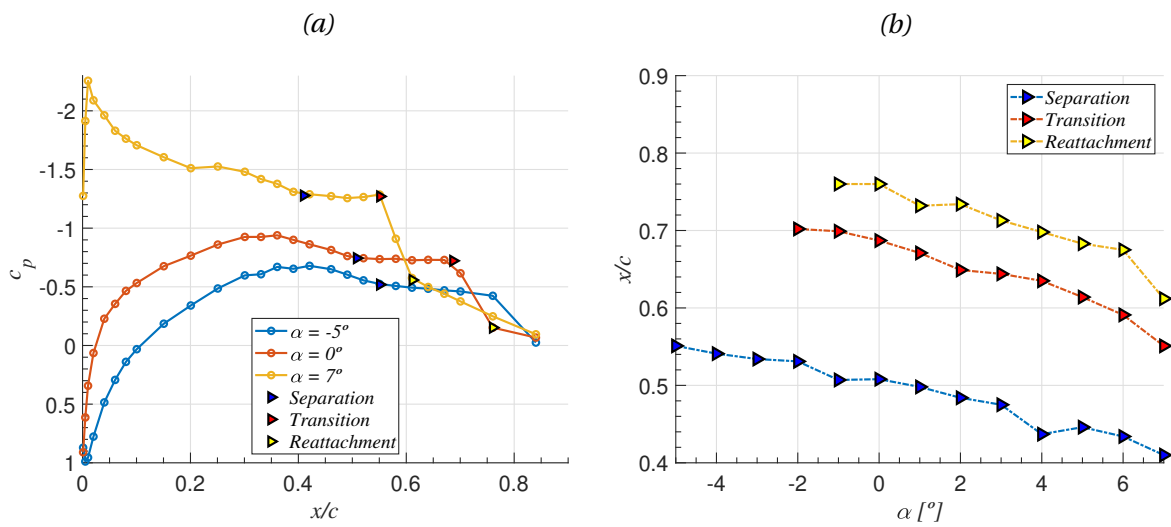


Figure 6.2: LSB characteristic locations estimated from  $c_p$  distributions, for the static wing at (a)  $\alpha = -5^\circ, 0^\circ$  and  $7^\circ$ . (b)  $-5^\circ \leq \alpha \leq 7^\circ$ .

The same methodology can be applied to all incidences tested. The obtained characteristic locations are shown in Fig. 6.2(b). The obtained trends indicate an approximately linear upstream movement of the bubble with increasing angle of attack, while the size remains nearly constant. Only a slight size reduction is observed to start for the highest incidences tested. Again, transition and reattachment estimation are missing for some negative  $\alpha$  due to the absence of pressure taps in that area.

### 6.1.2. Particle Image Velocimetry

The extent of the LSB is investigated in more detail using PIV. Contours of time-averaged velocity magnitude are shown in Fig. 6.3, together with streamwise velocity BL profiles at selected locations. A comparison between two different incidences is given in the figure, as Fig. 6.3(a) is obtained for the static wing at  $\alpha = 0^\circ$  while Fig. 6.3(b) represents the solution for  $\alpha = 7^\circ$ . As discussed in §5.2, the presence of the bubble is identified with the mean dividing streamline (black line) that encloses the bubble from the outer flow at the airfoil's surface. As for the pressure taps, PIV suggests an upstream shift and slight size reduction of the bubble for increasing incidence.

The location of transition to turbulence, occurring in the separated shear layer, is estimated at the point where the BL shape factor reaches a maximum inside the bubble. The evolution of  $H$

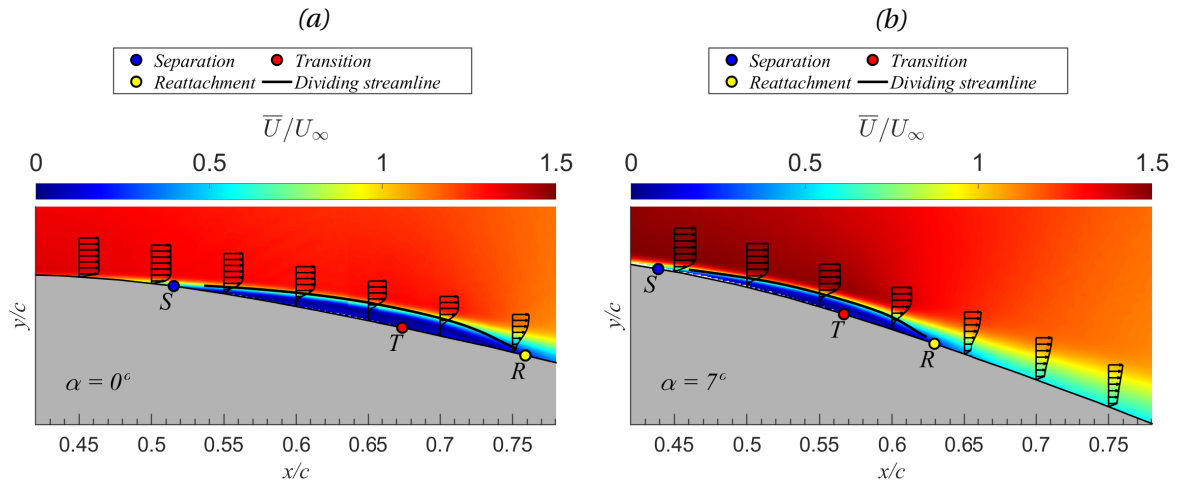


Figure 6.3: Contours of time-averaged velocity magnitude from PIV measurements, for the static wing at (a)  $\alpha = 0^\circ$  and (b)  $\alpha = 7^\circ$ .

inside the LSB is shown in Fig. 6.4(a) for the wing at  $\alpha = -5^\circ, 0^\circ$  and  $7^\circ$ . As expected, there is an upstream shift of transition for increasing incidence, while the shape of the  $H$  distribution remains similar.

The application of this methodology to every static angle of attack tested gives the characteristic locations shown in Fig. 6.4(b). To simplify the experimental campaign, no PIV measurements were conducted for  $\alpha = -4^\circ$  and  $\alpha = -2^\circ$ . The missing reattachment location for  $\alpha = -5^\circ$  was caused by the bubble being slightly downstream of the field of view of the PIV camera at that condition.

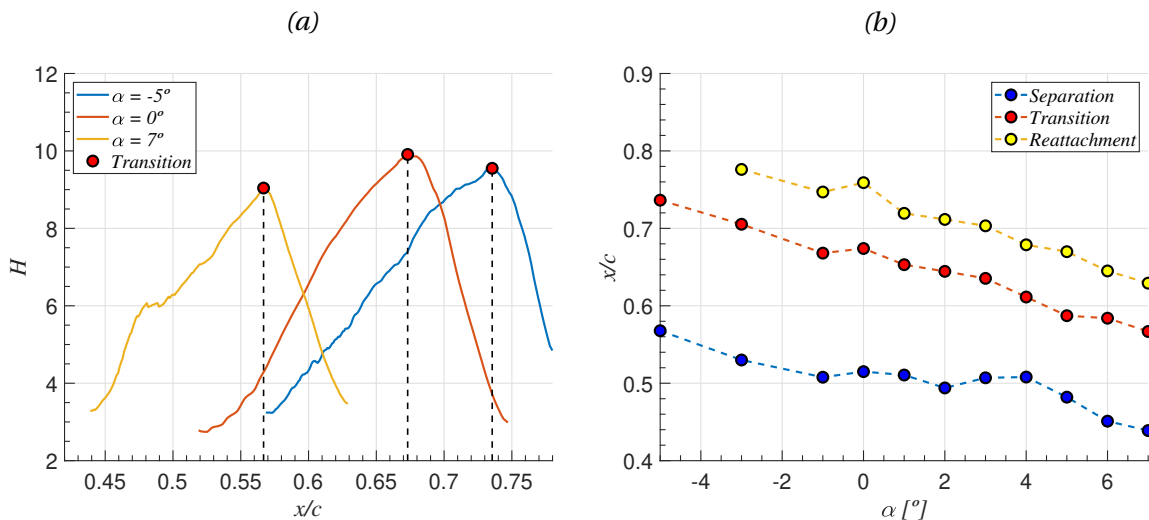


Figure 6.4: (a) Evolution of the BL shape factor inside the LSB, for the static wing at  $\alpha = -5^\circ, 0^\circ$  and  $7^\circ$ . (b) LSB characteristic locations extracted from the PIV measurements.

The obtained trends are similar to those discussed earlier for the pressure taps, showing a linear upstream shift of the bubble for increasing incidence. The detection of laminar separation shows more scatter than the others. This is mainly caused by the higher uncertainty of the PIV measurements in this region close to the surface and also the angle between the dividing streamline and the surface. Even if the uncertainty is higher also in the reattachment region (due to laser reflections at the surface), there is a bigger angle between the dividing streamline and the surface, thus reducing the error of extrapolating the streamline until it intersects with the wing.

### 6.1.3. Infrared Thermography

The objective of the static IT approach is to detect the characteristic locations of the LSB from the time- and spanwise-averaged infrared intensity distributions, without the need for a camera calibration to transform from the measured infrared intensity to surface temperature. The methodology applied follows the description of §5.3.2. Laminar separation is estimated to occur at the location of maximum increase rate of infrared intensity, transition at the maximum decrease rate and reattachment at the local minimum. Fig. 6.5(a) shows infrared intensity distributions for the static wing at  $\alpha = -5^\circ, 0^\circ$  and  $7^\circ$ . The LSB characteristic locations are indicated on top of the infrared intensity curves. These show a region of higher temperature inside the LSB, as heat transfer by convection is low in areas of separated flow. The strong temperature decrease linked to the transition process is followed by a slow rise as the turbulent BL thickens. The characteristic locations detected also indicate the upstream shift of the bubble with increasing incidence.

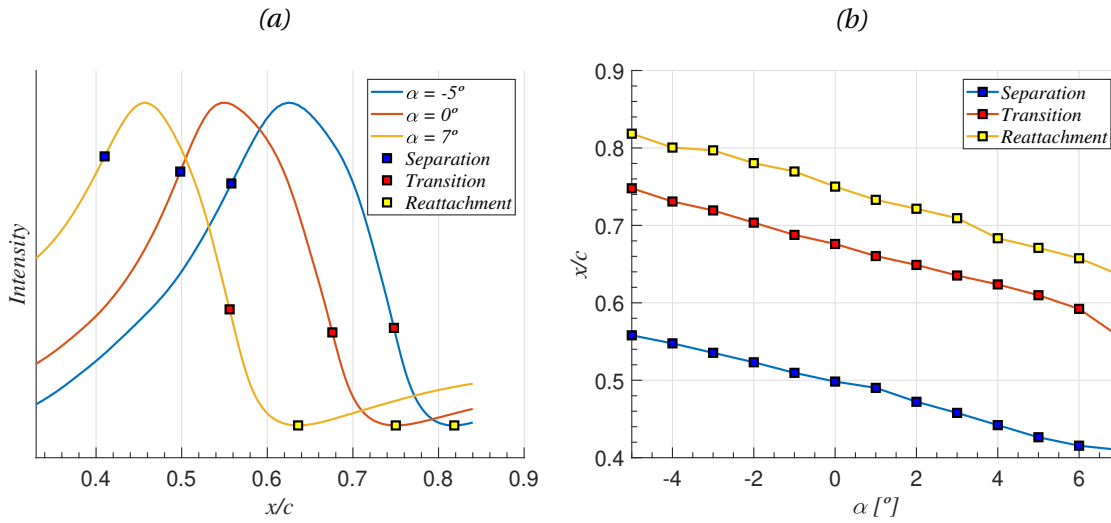


Figure 6.5: LSB characteristic locations estimated from time- and spanwise-averaged infrared intensity distributions, for the static wing at (a)  $\alpha = -5^\circ, 0^\circ$  and  $7^\circ$ . (b)  $-5^\circ \leq \alpha \leq 7^\circ$ .

Extending the approach to every angle of attack gives the LSB characteristic locations shown in Fig. 6.5(b). The linear upstream shift of the bubble with increasing incidence is clearly visible, as there is very little scatter for every location detected with IT.

The alternative approach studied here is to consider the static DIT method, as introduced in §5.3.3. The DIT technique requires the subtraction of two thermograms to provide information about the BL state at the intermediate incidence. The two distributions, at incidences  $\alpha_1$  and  $\alpha_2$ , need to be chosen according to:

$$\alpha = \frac{\alpha_1 + \alpha_2}{2}, \quad (6.2a)$$

$$\Delta\alpha = \alpha_2 - \alpha_1, \quad (6.2b)$$

where  $\Delta\alpha$  is the difference in incidence between the two thermograms. Small values of  $\Delta\alpha$  may not provide detectable DIT peaks, whereas high ones can cause erroneous results in their location. As the static infrared measurements were acquired at one-degree increments in angle of attack,  $\Delta\alpha = 1^\circ$  for this investigation. The LSB characteristic locations may be estimated from the DIT peaks (local maximum and minimum of the DIT distribution). However, the sign of the peaks depends on the choice of  $\Delta\alpha$ . For  $\Delta\alpha > 0$ , as considered here, the bubble is expected to move upstream from  $\alpha_1$  to  $\alpha_2$ . Thus, separation at the intermediate incidence  $\alpha$  appears as a positive DIT peak, whereas transition is linked to the negative one. For both situations, reattachment is estimated to occur when the DIT curve first reaches zero after transition.

Fig. 6.6(a) illustrates the approach for three different intermediate incidences. These are constructed as close as possible to the static angles of attack discussed earlier for previous techniques. Using  $\Delta\alpha = 1^\circ$ , the values considered are  $\alpha = -4.5^\circ, 0.5^\circ$  and  $6.5^\circ$ . The infrared intensity distributions employed to construct each DIT curve shown can be obtained by solving  $\alpha_1$  and  $\alpha_2$  from equations (6.2a) and (6.2b). The LSB characteristic locations, indicated on top of the DIT curves, still show the upstream shift of the bubble for increasing incidence. It can be also seen that the value of  $\Delta\alpha = 1^\circ$  is sufficient to obtain distinct peaks linked to the separation and transition processes.

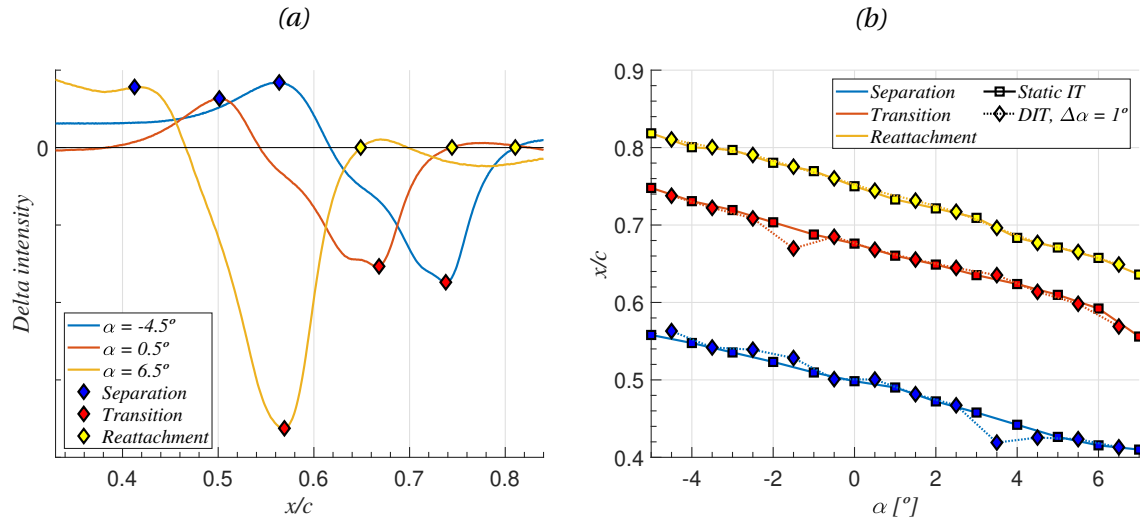


Figure 6.6: (a) LSB characteristic locations estimated from the static DIT method, for the static wing at  $\alpha = -4.5^\circ, 0.5^\circ$  and  $6.5^\circ$ . (b) Comparison between the LSB characteristic locations measured with the static IT and DIT approaches.

Following the same methodology, the LSB characteristic locations obtained from the static DIT method are compared in Fig. 6.6(b) with those shown earlier for the IT approach. Apart from a couple of isolated outliers, there is remarkable agreement between the two techniques. This confirms the validity of DIT to study the case of a LSB and motivates its exploration for the unsteady investigations.

#### 6.1.4. Comparison of experimental techniques

Three different flow measurement techniques have been used to characterize the static LSB. All of them can detect the characteristic locations of the bubble and find a similar effect of angle of attack on its size and location. The locations obtained from each of the techniques, shown in Fig. 6.2(b) for the static pressure taps, in Fig. 6.4(b) for PIV and in Fig. 6.5(b) for the static IT approach, are now put together for a more clear comparison between them. The obtained comparison is shown in Fig. 6.7. A first inspection of the figure indicates that there is good agreement between the techniques, showing typical differences in the detected locations of less than 2% of the airfoil chord. The agreement between PIV and IT is similar to that reported by Wynnuchuk and Yarusevych [86].

The biggest discrepancies occur for the PIV estimation of laminar separation at positive angles of attack. PIV gives a nice description of the flow topology in the region of the bubble but struggles to provide accurate estimations close to the surface due to the higher uncertainty mainly caused by reflections of the laser sheet after intersecting with the wing. It clearly provides more information than the other techniques about the transition process in the separated shear layer, but it is not the best choice for surface applications.

The static pressure taps are not only a simpler technique, but also provide direct information at the surface. However, a fine distribution of taps is needed in order to capture the LSB location accurately. If the resolution drops, no clear information can be retrieved from the static pressure

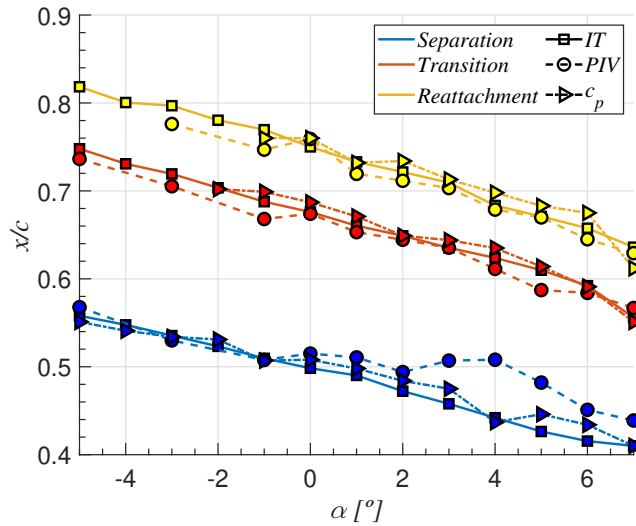


Figure 6.7: Comparison of the LSB characteristic locations obtained for the static wing using three different flow measurement techniques.

coefficient distribution, as is the case for some negative angles of attack in the current static investigation.

Infrared Thermography is able to detect similar locations. This is achieved directly from the time-averaged infrared intensity recorded with the infrared camera, without the need for temperature calibration. The experimental effort is reduced compared to PIV, and the results show less scatter. In this regard, IT is the ideal choice for static LSB characterization. It is perfect to detect surface heat transfer changes caused by the separation and reattachment of the BL, but can also identify the effect that transition has at the surface, thus providing information about the separated shear layer. In the present investigation, the infrared measurements indicate a strong two-dimensionality of the LSB, but the approach could be easily extended to study a three-dimensional situation. This would be extremely challenging for the static pressure taps and would also involve a more complex tomographic PIV setup.

## 6.2. Pitching investigation

This section presents the results of the pitching experiment, designed to explore the capabilities of DIT for the detection of an unsteady LSB. The motion imposed to the wing consists of pitch up and pitch down ramps at a constant pitch rate, between  $\alpha = -3^\circ$  and  $\alpha = 7^\circ$ . To test the performance of the technique, the complexity of the problem is increased by changing the pitch rate of the motion. As for the static characterization, the discussion in this section is organized in terms of the experimental techniques considered.

First, §6.2.1 covers the surface pressure measurements from the pressure taps. These are used for comparison with other techniques but also with unsteady linear theory. To simplify the experimental campaign, only two reduced frequencies,  $k = 0.05$  and  $k = 0.15$ , were considered for PIV measurements. These are discussed in §6.2.2. For both techniques, the discussion focuses on the two reduced frequencies mentioned above, by showing the differences between pitch up and pitch down at the mid-angle of the motion,  $\alpha = 2^\circ$ .

Then, §6.2.3 deals with the infrared measurements. This includes from quasi-steady motions ( $k = 0.0002$ ) up to  $k = 0.25$ , but focusing again on  $k = 0.05$  and  $k = 0.15$  for better comparison with the previous. The application of the DIT technique is discussed in detail, showing the effect of time separation between frames on the applicability of the method. Results are first presented at  $\alpha = 2^\circ$

and then extended to the full pitching ramps.

Finally, the comparison between the three techniques available is given in §6.2.4. This is shown in terms of the hysteresis in transition location obtained between pitch up and pitch down at  $\alpha = 2^\circ$ .

### 6.2.1. Surface pressure measurements

The static pressure taps are not only used here to detect the characteristic locations of the unsteady LSB, but also for comparison between the experiments and linear unsteady theory. The comparison with Theodorsen's theory, introduced in §2.1 and described by equation (2.1) in terms of unsteady lift coefficient, can be simplified when considering only the pitching contribution. While Theodorsen's theory is derived for sinusoidal pitching and plunging contributions, the motion studied here has a constant pitching rate. This mainly modifies the non-circulatory part of the unsteady lift response due to flow acceleration, which is small for the reduced frequencies considered here. The circulatory part of the response behaves similarly to that of a pure angle of attack change, as described by Leishman [44] and illustrated in Fig. 2.1(b), where lift shows a phase lag with respect to  $\alpha$ . This means that lift is lower than the static value for increasing incidence, while the opposite occurs for decreasing incidence. The amplitude of the response is adapted by including the constant pitching rate term, by simplifying equation (2.1) to:

$$c_l = \pi \frac{c}{2} \left[ \frac{\dot{\alpha}}{U_\infty} \right] + 2\pi C(k) \left[ \alpha + \frac{c}{2} \left( \frac{1}{2} - a \right) \frac{\dot{\alpha}}{U_\infty} \right], \quad (6.3)$$

where the only contributions are those caused by the change in angle of attack and the constant pitching rate. Please note that  $a = -0.2$  due to the wing pitching around its main spar located at 40% of the chord. Recall that the unsteady response used for the comparison with the experiments requires the addition of the phase lag, which virtually acts like changing the sign of some terms inside equation (6.3).

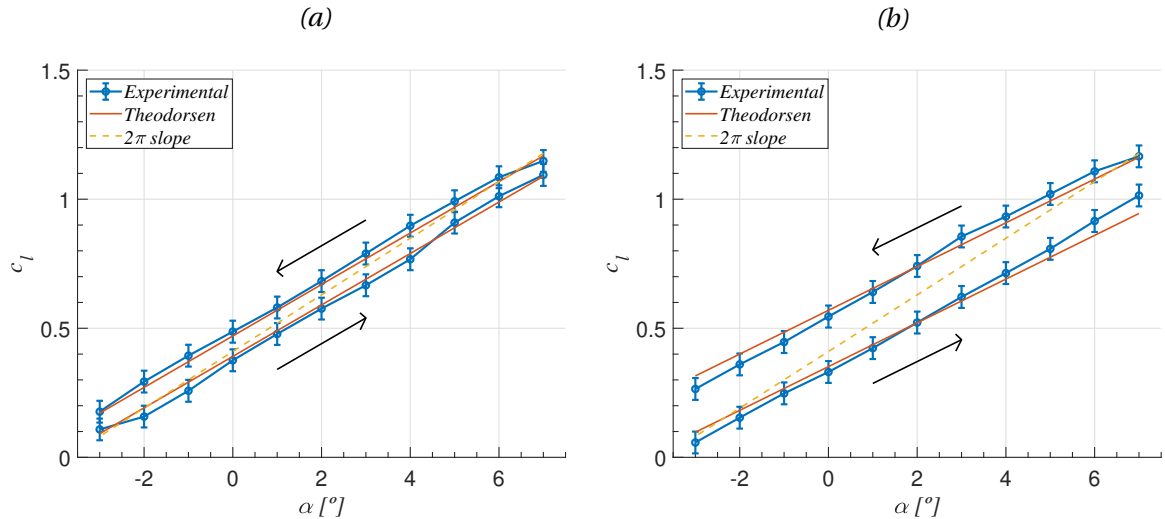


Figure 6.8: Unsteady lift coefficient for the pitching wing, with: (a)  $k = 0.05$  and (b)  $k = 0.15$ .

In the experiments, lift coefficient along the motion can be obtained from numerical integration of the phase-averaged  $c_p$  distributions. It should be noted that the fabrication process did not allow placing a pressure tap at the trailing edge. For integration purposes, interpolation is necessary in that region. An additional point is included at the trailing edge of the airfoil. Static pressure is estimated to be the mean between the measurements from the suction and pressure sides of the wing closest to that point. For  $k = 0.05$ , the unsteady lift coefficient obtained for the pitch up and pitch down motions is shown in Fig. 6.8(a). The experimental results are compared to the static

slope and also the prediction of the adapted Theodorsen's theory model, as described by equation (6.3). The linear theory, in good agreement with the experimental results, indicates a hysteresis in  $c_l$  between pitch up and pitch down of similar amplitude. In the experiments, at  $\alpha = 2^\circ$ , lift is lower during pitch up than the static value, while the opposite occurs during pitch down. This agrees with the phase lag predicted by Theodorsen for a sinusoidal change in angle of attack.

A similar behaviour is observed for  $k = 0.15$ , as shown in Fig. 6.8(b). The higher reduced frequency causes an increase of the hysteresis between pitch up and pitch down, but is still in good agreement with the linear theory.

The observed hysteresis does also extend to the LSB location. Fig. 6.9 shows phase-averaged static pressure coefficient distributions for the pitching wing at  $\alpha = 2^\circ$ , both during pitch up and pitch down. The hysteresis in bubble location is indicated by the transition location estimation, which is obtained following the same methodology as for the static investigation. Transition is observed to occur slightly upstream during pitch down, which is in agreement with the experimental results of Nati et al. [52] for a sinusoidally pitching airfoil, as reported in Fig. 2.2.

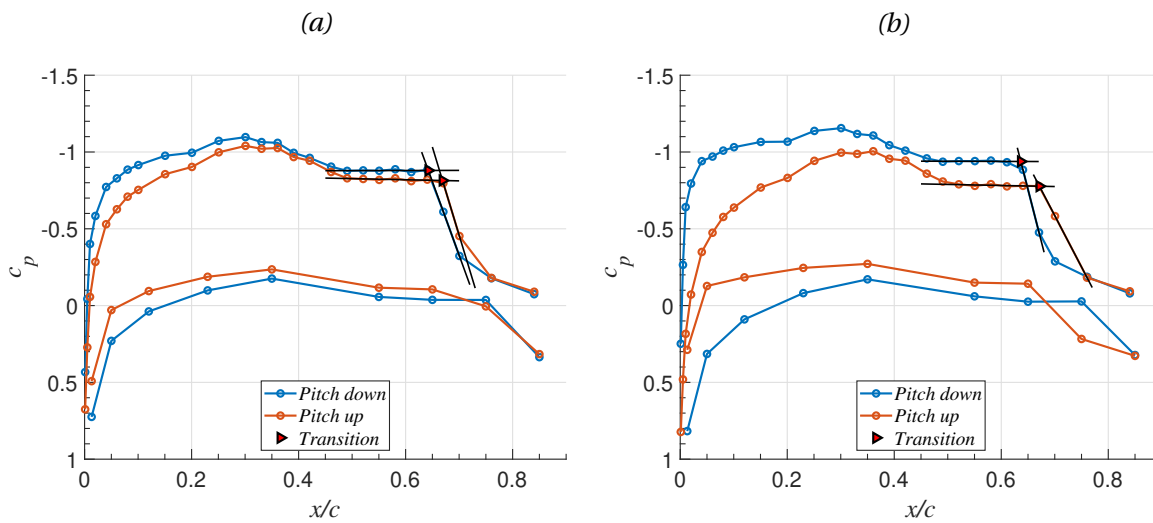


Figure 6.9: Phase-averaged  $c_p$  distributions for the pitching wing at  $\alpha = 2^\circ$ , both for pitch up and pitch down, with: (a)  $k = 0.05$  and (b)  $k = 0.15$ .

As for lift coefficient, increasing from  $k = 0.05$  (Fig. 6.9(a)) to  $k = 0.15$  (Fig. 6.9(b)) causes an increase in the hysteresis between pitch up and pitch down, now represented in terms of the unsteady transition location.

### 6.2.2. Phase-averaged PIV measurements

A deeper inspection into the effects that the unsteadiness has on the LSB can be done from the PIV measurements. Fig. 6.10 shows contours of phase-averaged velocity magnitude for the pitching wing at  $\alpha = 2^\circ$ , with  $k = 0.05$ . Streamwise velocity BL profiles are included at certain locations for a complete description of the bubble. While 6.10(a) includes the result during pitch up, 6.10(b) contains the pitch down measurement. The LSB characteristic locations are estimated as for the static situation, following the methodology described in §5.2. A close look at these locations confirms that the bubble appears slightly more upstream during pitch down, between 1% and 2% of the airfoil chord depending on the location. This is in agreement with the qualitative behaviour observed from the phase-averaged  $c_p$  distributions.

The results for  $k = 0.15$  are shown in Fig. 6.11. Fig. 6.11(a) includes the pitch up measurement and 6.11(b) the pitch down one. The hysteresis between pitch up and pitch down is now more evident, with PIV showing a difference between 3% and 4% of the chord depending on the charac-

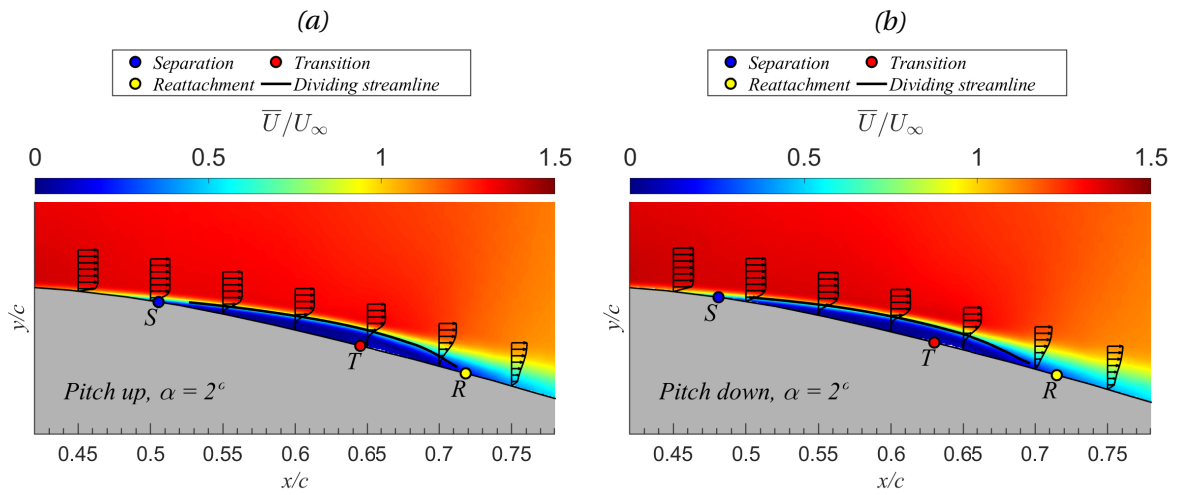


Figure 6.10: Phase-averaged velocity magnitude for the pitching wing at  $\alpha = 2^\circ$ , with  $k = 0.05$ , during (a) pitch up (b) pitch down.

teristic location.

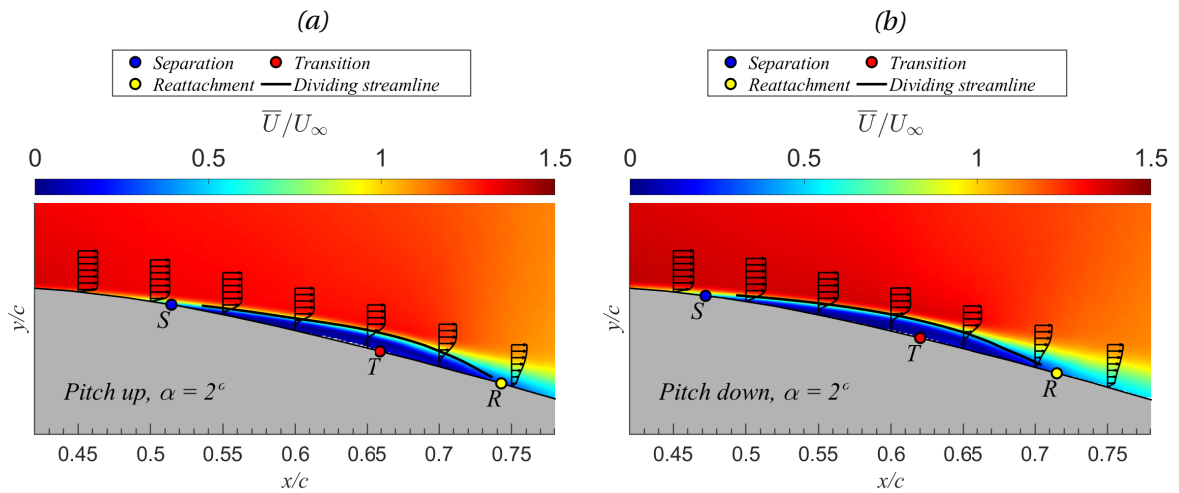


Figure 6.11: Phase-averaged velocity magnitude for the pitching wing at  $\alpha = 2^\circ$ , with  $k = 0.15$ , during (a) pitch up (b) pitch down.

### 6.2.3. Infrared Thermography

From an experimental perspective, the increase in reduced frequency is not something problematic for the pressure taps or PIV measurements. Using a phase-averaged approach, both techniques can easily deal with motion frequencies much higher than the ones considered here. However, this is not the case for infrared measurements. To illustrate the effect of reduced frequency on the infrared approach, this section is organized in terms of increasing aerodynamic complexity. The regimes studied cover from quasi-steady motions to fully unsteady ones.

#### Quasi-steady measurements

Infrared measurements were conducted for the quasi-steady pitching airfoil as a first step of the DIT method outside the static regime. This motion, characterized by  $k = 0.0002$ , has no effect on the LSB, such that it follows the static behaviour discussed in §6.1. Furthermore, only infrared results for the pitch up case are reported here, as these are identical for the pitch down situation. Fig. 6.12(a) shows

DIT curves at  $\alpha = 2^\circ$ , constructed using various separations between infrared frames (see equation (6.2b)). The DIT peaks (positive for separation and negative for transition, as  $\Delta\alpha > 0$ ) change in strength and location with the different DIT frames considered. As discussed by Gardner et al. [18] for unsteady transition on a pitching airfoil, increasing the time difference (or angle difference here) between the infrared frames used to construct the DIT curve causes an erroneous drift from the true location of interest. The suggested approach is to minimize this difference while the DIT peaks are still detectable. This is indicated in Fig. 6.12(a) by including the static transition location measured with IT at  $\alpha = 2^\circ$ .

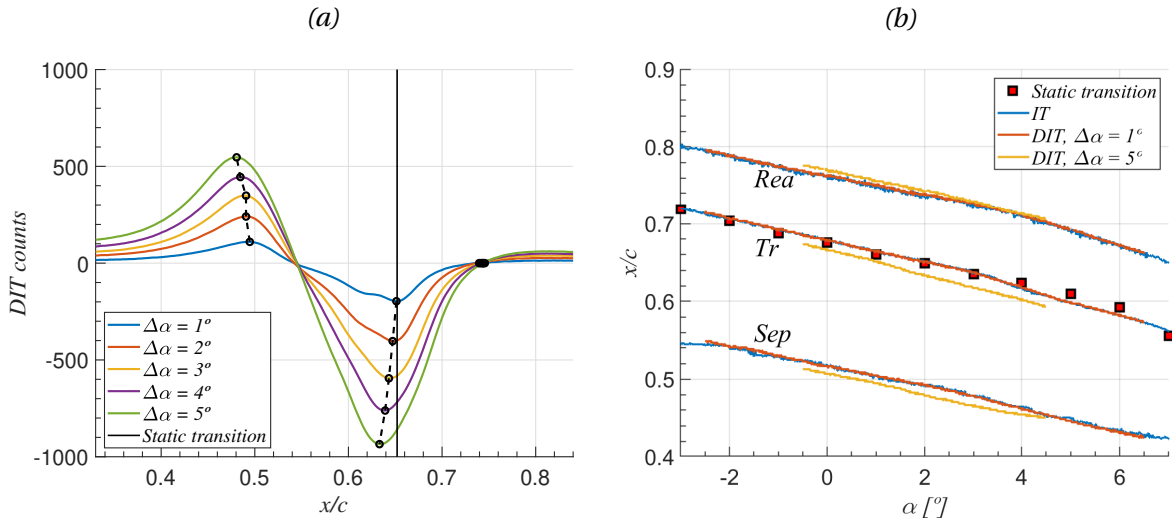


Figure 6.12: (a) DIT curves at  $\alpha = 2^\circ$  for the quasi-steady pitching wing, using various separations between infrared frames,  $\Delta\alpha$ . (b) LSB characteristic locations for the quasi-steady pitching wing, obtained from the static IT and DIT methods.

The figure does also indicate a stronger peak for transition compared to the separation one (approximately double the strength), which could be already observed in the static DIT investigation discussed earlier. This is in agreement with the DIT results extracted from the analytical thermal model presented in §5.3.4 (see for example Fig. 5.13), and suggests that the detection of transition will be much simpler than the others in the unsteady configurations.

The DIT approach can be extended to every instantaneous angle of attack measured along the quasi-steady motion. The DIT curves are constructed from the subtraction of two spanwise-averaged instantaneous infrared intensity distributions. The obtained LSB characteristic locations are shown in Fig. 6.12(b). As the motion is thermally quasi-steady, the static IT approach can still be used to estimate the characteristic locations directly from the instantaneous distributions. The agreement between IT and DIT confirms that the motion is indeed quasi-steady, and that it resembles well the static behaviour of the LSB, as indicated from the static transition measurements presented earlier. As suggested above, increasing the time difference between DIT frames, from  $\Delta\alpha = 1^\circ$  to  $\Delta\alpha = 5^\circ$ , causes a systematic error in the detection of the LSB.

The current thermally quasi-steady approach provides the best static characterization possible of the LSB. Both the IT and DIT methods have been shown to work for spanwise-averaged instantaneous infrared intensity distributions. This gives a continuous evolution of the LSB with varying incidence, which is virtually impossible to achieve with techniques that require time-averaging, such as the pressure taps or PIV, to provide a meaningful description of the bubble.

#### $k = 0.05$

For the unsteady measurements, the approach followed is to apply the DIT method. The DIT curves and the estimation of the LSB characteristic locations are done in an identical manner to the quasi-

steady case presented above. Fig. 6.13 shows DIT curves for the pitching wing at  $\alpha = 2^\circ$ , considering four different time separations between DIT frames. The results for the pitch up motion are given in Fig. 6.13(a). Again, as  $\Delta\alpha > 0$  for pitch up, laminar separation is linked to the positive DIT peak while transition is defined at the negative one. The DIT curves do show a clear negative peak linked to the transition process, but the positive peak is not visible. As argued for the quasi-steady results, the weaker separation peak may not be detectable in an unsteady situation. Similarly, the small temperature differences between frames cause the noise level to obscure the reattachment region. It can be seen how the shape of the DIT curve changes downstream of the transition peak when choosing different time separations, making it hard to find a robust estimation of the reattachment location. However, the DIT method does find the negative peak linked to the unsteady transition region. The strength of this peak improves with increasing time difference between frames, as expected, while a small change in location is observed for the time differences considered here. To provide a clear picture of the LSB hysteresis, the static transition location obtained from IT at  $\alpha = 2^\circ$  is included in the figure. The DIT peak does occur downstream of the static location, pointing towards the behaviour observed with the pressure taps and PIV.

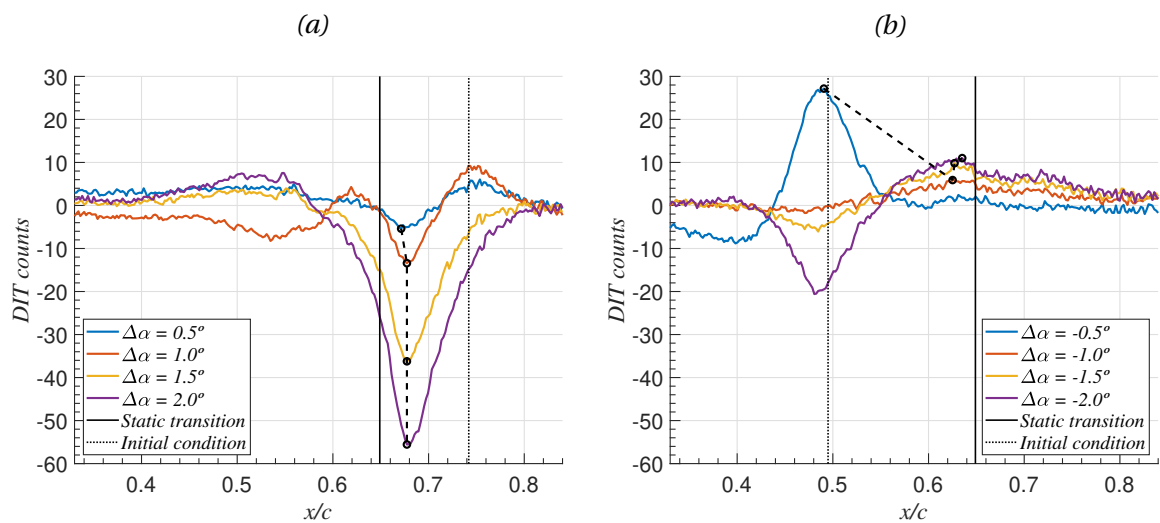


Figure 6.13: DIT curves for the pitching wing at  $\alpha = 2^\circ$ , with  $k = 0.05$ , during (a) pitch up (b) pitch down.

The analogous situation for the pitch down motion is shown in Fig. 6.13(b). As  $\Delta\alpha < 0$  for pitch down, laminar separation is linked to the negative DIT peak while transition occurs at the positive one. A prominent peak is observed in the region of separation,  $x/c \sim 0.5$ , but it changes from positive to negative for increasing time separation, so this is not linked to the unsteady separation location. This feature corrupts the DIT measurement in that region, thus making it impossible to detect laminar separation. Downstream of it, the positive DIT peak linked to the unsteady transition process can be observed. This can be detected when choosing sufficient time separation between DIT frames, but its strength is a lot weaker compared to the transition peak for the pitch up case shown in Fig. 6.13(a). This behaviour, indicating stronger DIT peaks for the pitch up case, was already suggested by the analytical thermal model, as illustrated in Fig. 5.13. For an equal change in heat transfer between laminar and turbulent BLs, a stronger DIT peak is expected to occur when the surface is warmer (laminar flow) and cools by the effect of transition to turbulence. The detected transition location does occur upstream of the static one, confirming that DIT can capture the hysteresis in transition location observed with the other techniques. Downstream of this, the DIT signal drops close to zero and no reliable estimation of reattachment can be made.

The erroneous DIT peak at  $x/c \sim 0.5$  is linked to the surface temperature distribution before the unsteady motion starts. The experimental procedure for the infrared acquisitions of the pitching

configuration, discussed in §4.5, was to study the pitch up and pitch down motions separately. The wing was first moved to an angle of attack outside of the motion range, and the measurement started only after a steady-state temperature distribution was reached for that condition. This was done to limit the change in bubble location to follow only one direction along the motion. The surface temperature distribution at this condition (different for pitch up and pitch down) is shown in Fig. 6.14(a). As expected, the bubble is clearly more downstream for the pitch up case, as the angle of attack is  $\alpha < -3^\circ$ , while  $\alpha > 7^\circ$  for the pitch down motion. The transition locations, estimated following the static IT approach, are included in Fig. 6.13 as dotted lines, and referred to as *initial condition*. For pitch up, Fig. 6.13(a), this location occurs downstream of transition, and explains the variable behaviour of the DIT signal when changing the time separation between frames. For the pitch down case, Fig. 6.13(b), it coincides with the erroneous feature at  $x/c \sim 0.5$ .

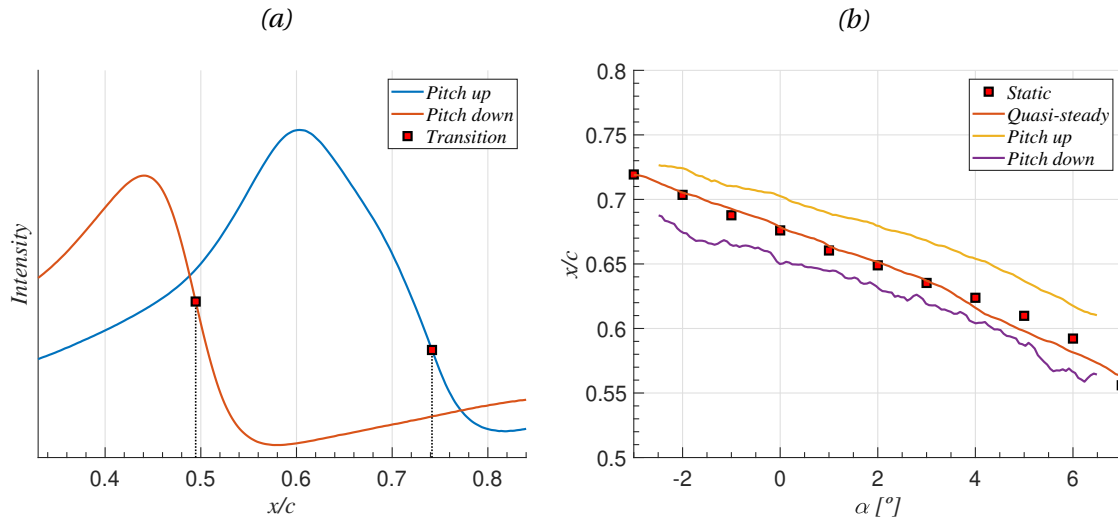


Figure 6.14: (a) Surface temperature distributions and transition location before the start of the pitching motion. (b) Unsteady transition location for the pitching wing, obtained from DIT, with  $k = 0.05$ , compared to static and quasi-steady situations.

This undesired behaviour appears as a result of the limited thermal response of the surface. For unsteady motions, the changes in surface temperature due to the change in aerodynamics are very limited, and the surface distribution remains almost constant. The location of the highest temperature gradient will still be linked to the situation before the start of the unsteady motion, and minor changes as those caused by variable external heating, camera viewing angle or camera noise appear enhanced around that location. These slight changes appear as erroneous DIT peaks and may compromise the DIT signal in that region.

As these initial conditions are outside of the measurement range,  $-3^\circ \leq \alpha \leq 7^\circ$ , the erroneous DIT peaks do not interfere with the true unsteady transition location at any point. The DIT approach detailed for  $\alpha = 2^\circ$  can be extended to the full measurement range to study the evolution of the transition location along the motion. The obtained trends, both for pitch up and pitch down, are shown in Fig. 6.14(b) and compared to the static and quasi-steady transition estimations. These curves are obtained using a time separation between DIT frames such that  $\Delta\alpha = 1^\circ$ . The results capture the hysteresis in transition location that was already observed with the other experimental techniques.

### $k = 0.15$

Already for the previous case where  $k = 0.05$ , the DIT method could only detect one of the three characteristic locations of the bubble along the pitching motion. The problem will be enhanced here, as the time difference (physical time) between DIT frames will have to decrease to keep a sim-

ilar value of  $\Delta\alpha$ . Starting with the pitch up motion, Fig. 6.15(a) shows the DIT curves for  $k = 0.15$  and the wing at  $\alpha = 2^\circ$ . The negative peak, indicative of transition, is still detectable when choosing enough time separation between DIT frames. The comparison with the previous result indicates that the DIT strength has dropped approximately 50%. The hysteresis in transition location with respect to the static value has also increased, which is in agreement with the other techniques employed.

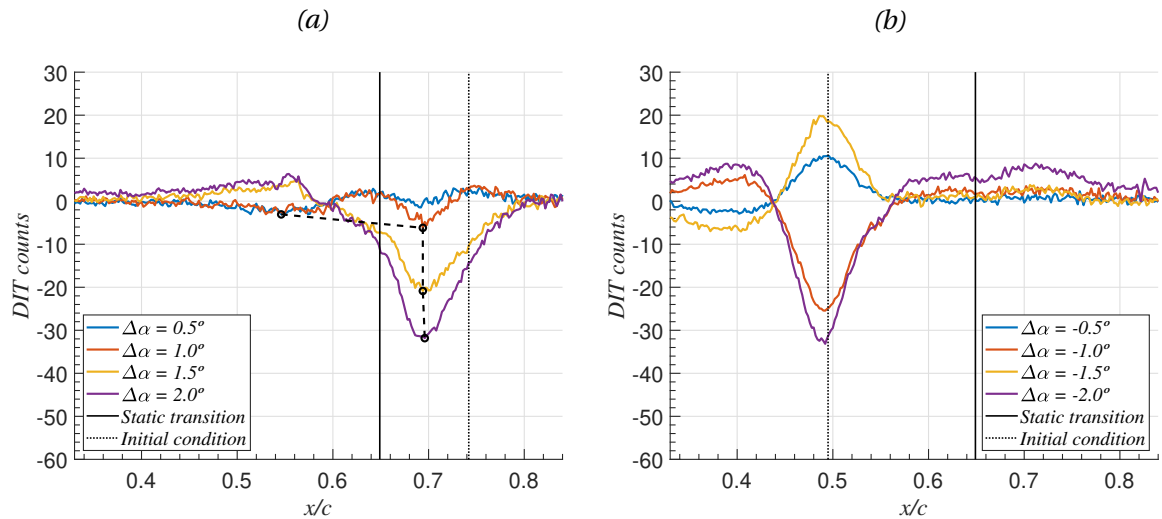


Figure 6.15: DIT curves for the pitching wing at  $\alpha = 2^\circ$ , for  $k = 0.15$ , during (a) pitch up (b) pitch down.

The pitch down situation is illustrated in Fig. 6.15(b). The figure is dominated by the erroneous DIT feature linked to the initial condition of the wing before the start of the motion. This time, for  $k = 0.15$ , no positive DIT peak associated with the unsteady transition location is visible. This suggests that the maximum reduced frequency for which the DIT method can detect the unsteady transition location is lower than  $k = 0.15$ , at least during pitch down. This value, which corresponds to a physical frequency of  $f = 1.69$  Hz (see Table 4.1), is lower than the one predicted by the analytical thermal model in comparison with the previous work from DLR, as discussed in §5.3.4 and illustrated by Fig. 5.14. This highlights the different behaviour of DIT between pitch up and pitch down conditions.

The behaviour discussed so far for the wing at  $\alpha = 2^\circ$  holds throughout the full pitching ramps. This means that, for  $k = 0.15$ , the unsteady transition curve is only obtained for the pitch up case. This is shown in Fig. 6.16 and compared to the static and quasi-steady transition measurements. The obtained transition location evolution is clearly downstream of the quasi-steady curve, showing more deviation than the previous case, for  $k = 0.05$ , presented in Fig. 6.14(b).

The two reduced frequencies discussed so far,  $k = 0.05$  and  $k = 0.15$ , have shown the effect of motion frequency on the DIT method. While the strength of the DIT signal dropped approximately 50% from one to another for pitch up, the method failed completely for pitch down in the latter case.

### Frequency effect on BL transition hysteresis

As the unsteady transition location has been the only characteristic location detectable with the DIT method, the other two will be neglected in this comparison. This section will incorporate every reduced frequency tested, as described by Table 4.1.

In the previous analysis, DIT curves were shown at a fixed motion frequency changing the time separation between DIT frames. Here, various frequencies will be shown together, with the time separation adjusted such that  $\Delta\alpha = \pm 1^\circ$  (positive for pitch up and negative for pitch down). Please note that, for the highest frequency tested,  $k = 0.25$ , the available number of frames (only 31 frames

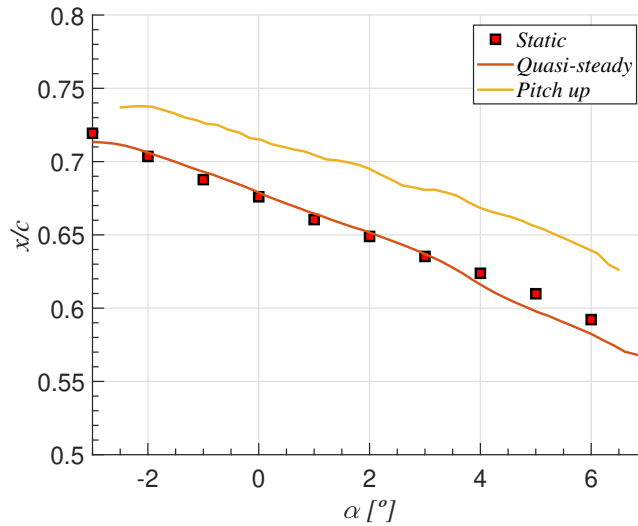


Figure 6.16: Unsteady transition location for the pitching wing, obtained from DIT, with  $k = 0.15$ , compared to static and quasi-steady situations.

acquired at 180 Hz for the full pitching ramp) means that the time separation between frames closest to the desired value, centred at  $\alpha = 2^\circ$ , gives  $\Delta\alpha = \pm 1.33^\circ$ , which is the value that will be used for the comparison.

DIT curves obtained at four different reduced frequencies are shown in Fig. 6.17(a) for the pitch up motion, with the wing at  $\alpha = 2^\circ$ . The negative DIT peak associated with the unsteady transition location is visible for every frequency. The location is always downstream of the static value, with the difference increasing with frequency as expected. The strength of the DIT peak generally decreases with increasing frequency, as the physical time between DIT frames reduces to keep  $\Delta\alpha$  constant. This result indicates that, for a pitch up situation, the DIT method may work beyond  $k = 0.25$ . According to the comparison with the DLR work discussed in §5.3.4, this situation is slightly more challenging than any other tested previously with DIT.

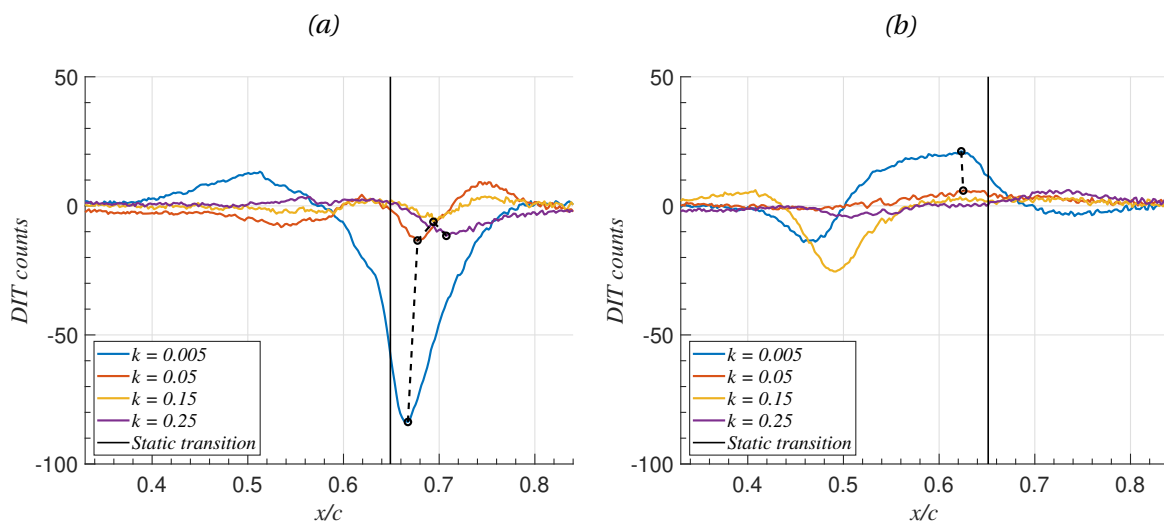


Figure 6.17: DIT curves for the pitching wing at  $\alpha = 2^\circ$ , for various motion reduced frequencies and using a time separation between DIT frames of  $\Delta\alpha = \pm 1^\circ$ , during (a) pitch up (b) pitch down.

A very different result is shown in Fig. 6.17(b) for the analogous pitch down case. The positive

DIT peak linked to transition, upstream of the static value, is not as distinct or strong as the pitch up one at the same frequency. The peak can only be detected for a couple of frequencies tested, and there is no increase in hysteresis observed. The comparison between Fig. 6.17(a) and 6.17(b) draws a huge difference between the two motions. While the maximum frequency is limited to a value around  $k = 0.05$  for pitch down, no limit was found for pitch up in this investigation. The shape and strength of the DIT peak at high frequencies suggests that the limit may not be very far from the values tested, but it could also be sufficient to increase the time difference between frames. This approach was not successful for the pitch down case. As indicated by Fig. 6.15(b), increasing the time difference may return a stronger DIT signal but not necessarily make a distinct peak appear.

The comparison between reduced frequencies can be extended beyond  $\alpha = 2^\circ$  to obtain the continuous transition location at every angle of attack along the motion. This is a big advantage of the infrared technique over the others. While the pressure taps and PIV involve the phase-averaging at discrete angles of attack that later need to be processed individually, the DIT approach provides a continuous evolution of the transition front. The results obtained for every reduced frequency tested are included in Fig. 6.18. The pitch up curves show transition downstream of the static value at the same incidence (represented by the quasi-steady measurement) while the pitch down curves show it upstream of it. For pitch up, hysteresis increases with reduced frequency, as measured with other techniques and in agreement with previous studies (see for example Pascazio et al. [56] or Lee and Basu [43]). The results during pitch down are inconclusive, being similar for every frequency available. This points again towards the difficulty encountered in the present investigation of applying the DIT method for a pitch down motion.

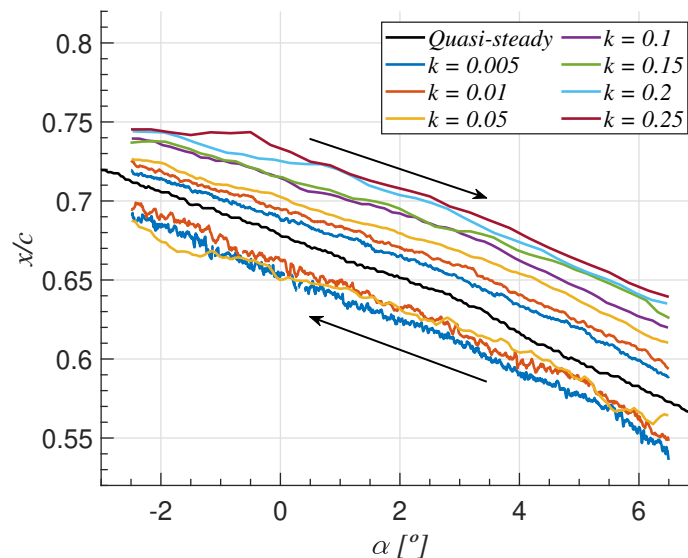


Figure 6.18: Unsteady transition location for the pitching wing, obtained from DIT, for every reduced frequency measured, both for pitch up and pitch down.

#### 6.2.4. Comparison of experimental techniques

Following the previous results, a comparison between the three flow measurement techniques considered is drawn here in terms of the transition hysteresis measured with each of them for the reduced frequencies tested. The hysteresis in transition location is typically defined as the difference between the pitch up and pitch down case. However, very limited information could be obtained from pitch down using DIT. To overcome this limitation, hysteresis will be defined here individually for each case, based on the static transition location. At  $\alpha = 2^\circ$ , hysteresis during pitch up is

obtained after subtracting the static value obtained with IT (see Fig. 6.5(b)) to the unsteady value obtained from DIT. A positive hysteresis value means that the unsteady location occurs downstream of the static one. This same procedure can be applied to the other techniques, using the static locations obtained with each of them (see Fig. 6.7 for the static comparison between techniques). This allows comparing the hysteresis in transition location measured with the three flow measurement techniques for every reduced frequency available. The obtained results are shown in Fig. 6.19, for the wing at  $\alpha = 2^\circ$ , in terms of the reduced frequency of the motion or constant pitch rate imposed. Please recall that, to simplify the experimental campaign, PIV measurements were conducted only for  $k = 0.05$  and  $k = 0.15$ . The experimental measurements are accompanied by a theoretical prediction, derived from linear unsteady theory. Given the good agreement between experimental lift coefficient and Theodorsen's theory shown in Fig. 6.8, the unsteady lift value predicted by the theory at  $\alpha = 2^\circ$  was matched to a different static angle of attack. The transition location at that incidence may be estimated from the quasi-steady IT measurements shown in Fig. 6.12(b).

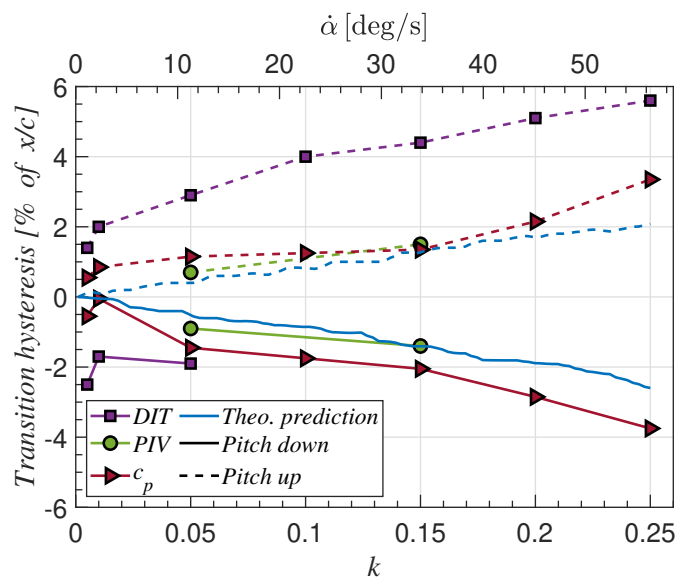


Figure 6.19: Hysteresis in transition location with respect to the static value obtained from the three experimental techniques for various pitching motion reduced frequencies. Theoretical prediction extracted from linear unsteady theory included for further comparison.

Fig. 6.19 shows a good agreement between pressure taps, PIV and theory, with all suggesting that hysteresis is approximately symmetric at this incidence. While all-three experimental techniques capture the expected increase in hysteresis with increasing motion frequency, the values measured with DIT are substantially higher. The obtained results show identical behaviour to those measured by DLR for the pitching airfoil. Richter et al. [65] measured a higher hysteresis in BL transition with DIT compared to hot-films and pressure transducers. The values reported there suggested an approximately constant difference between techniques for all frequencies tested. Later, Wolf et al. [84] extended the frequencies explored and captured the behaviour towards zero. The results point towards no difference with respect to other techniques for very small frequencies, but later this difference increases until reaching a nearly constant value, in agreement with the previous observations. The values shown here (for pitch up) also show a small difference between DIT and the pressure taps for the smallest frequencies tested, with the difference quickly increasing and later showing a constant offset. This offset is attributed to the thermal response of the surface. While this is inherent to the infrared approach, it could be mitigated by improving the surface properties of the wing.

The pitching experiment has demonstrated the applicability of DIT to study the unsteady tran-

sition location occurring in the separated shear layer for the presence of a LSB. The proposed extension of the method, to try and identify also the locations of laminar separation and turbulent reattachment, has only worked for a simple quasi-steady situation. In a more general unsteady case, the limited thermal response of the surface only allowed detecting the strongest DIT peak, which is linked to the transition process. A big discrepancy was also found between pitch up and pitch down situations. During pitch up, the transition front moves upstream, thus cooling regions that were previously under laminar flow. This is significantly more effective than the opposite situation, thus enhancing the DIT approach. Every pitching frequency tested could be analyzed during pitch up using DIT, while this was limited to  $k \leq 0.05$  for pitch down. The unsteady motion causes a hysteresis in bubble location that could be measured with the three techniques considered. During pitch up, the pressure gradient is more favourable than the static situation, thus delaying laminar separation, while the opposite occurs during pitch down. Good agreement was found between the pressure taps and PIV in the transition hysteresis measured, while DIT consistently measured greater values. This behaviour was already observed in previous experiments involving the use of DIT for unsteady BL transition detection and appears due to the thermal lag of the surface with respect to the aerodynamic unsteadiness.

### 6.3. Plunging investigation

The plunging experiment discussed in this thesis constitutes a more complex aerodynamic problem than the previous pitching investigation. The chord-based Reynolds number is kept at  $Re = 200k$  and the nominal angle of attack of the wing is set to  $\alpha_{nom} = 0^\circ$ . A sinusoidal plunging motion with an amplitude of  $h = 6\%$  of the airfoil chord and a reduced frequency of  $k = 0.67$  is imposed on the wing to study the effects that the aerodynamic unsteadiness has on the LSB that forms on the suction side of it. While this amplitude-frequency combination induces a range of effective angles of attack comparable to the amplitude of the pitching motion, the reduced frequency is nearly three times bigger than the maximum one tested for the other experiment. This complicates the infrared approach and may cause some deviation from linear unsteady theory. The plunging investigation is one of the main topics inside the research project at The University of Arizona. The WT experiments reviewed here have been compared with results from high-fidelity numerical simulations, as discussed recently by Grille Guerra et al. [28].

As there is only one plunging configuration studied, the section is organized in a similar manner to the static characterization of the LSB. First, §6.3.1 covers the experimental results from the static pressure taps and the high-bandwidth pressure transducer. As before, lift coefficient is extracted from the taps and compared with Theodorsen's theory for pure plunge. The location of the LSB along the cycle is detected from phase-averaged  $c_p$  distributions. Then, §6.3.2 presents the phase-averaged PIV measurements, showing the evolution of the LSB along the sinusoidal cycle. The obtained results are compared with those from the pressure taps before discussing the infrared measurements in §6.3.3. This includes phase-averaged surface temperature distributions along the plunging cycle and the application of the DIT method for a couple of different phases.

#### 6.3.1. Surface pressure measurements

Lift coefficient, extracted from numerical integration of the pressure taps, is obtained at 16 different phases along the plunging cycle in order to be compared with Theodorsen's theory prediction for a sinusoidal plunging motion. The general prediction for the unsteady lift, as described by equation (2.1), includes contributions from plunging and pitching motions. In this context, retaining only the terms linked to a sinusoidal plunge reduces the equation to:

$$c_l = \pi \frac{c}{2} \left[ -\frac{\ddot{y}_w}{U_\infty^2} \right] + 2\pi C(k) \left[ -\frac{\dot{y}_w}{U_\infty} \right], \quad (6.4)$$

where  $y_w$  is the non-dimensional wing position along the cycle, linked to the motion amplitude  $h$  through equation (4.1). Please note the sign change with respect to equation (2.1), as Leishman [44] defines positive plunge when the wing moves down, while this is changed in the current investigation. This result may be added to the static lift prediction of the wing to construct the lift coefficient evolution through the cycle. This, written in terms of the effective angle of attack induced by the motion (see equation (4.4)), is compared to the experimental measurements in Fig. 6.20(a). The experimental results show a deviation from the linear unsteady theory during most of the cycle. At this point, this behaviour could be caused by the high amplitude-frequency combination or by a change in the dynamics of the LSB. The shape of the lift curve does also reveal a hysteresis between upstroke (increasing  $y_w$ ) and downstroke (decreasing  $y_w$ ). Please note that the hysteresis shows an opposite trend to that observed in the pitching investigation. Here, for an equal effective angle of attack, a higher lift is measured when the effective incidence is increasing compared to the static situation, while the opposite occurs for decreasing incidence. This is in agreement with the linear theory, which predicts such behaviour for a sinusoidal plunge.

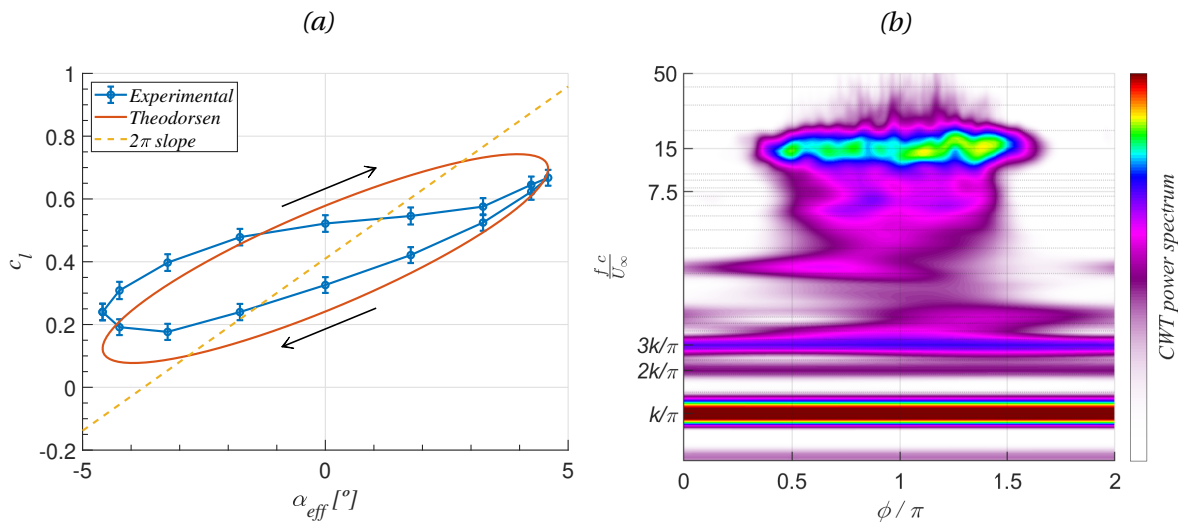


Figure 6.20: (a) Lift coefficient evolution along the plunging cycle, written in terms of the effective angle of attack of the wing. Comparison between experiments and Theodorsen's theory. (b) Phase-averaged power spectrum of the CWT of pressure fluctuations captured with the high-bandwidth pressure transducer at  $x/c = 0.65$ .

The nature of the LSB through the cycle is first investigated using the high-bandwidth pressure transducer placed at  $x/c = 0.65$ . In the static characterization, this device was used to reveal the amplification of disturbances in the separated shear layer, caused by an inviscid Kelvin-Helmholtz instability. As illustrated in Fig. 6.1(b), the amplification of disturbances was centered at a chord-based Strouhal number of  $f c / U_\infty \approx 15$  for all angles of attack tested. For the plunging investigation, the pressure signal is transformed using a CWT and then phase-averaged to the motion, as discussed in §4.3. The power spectrum of the phase-averaged CWT of pressure fluctuations is shown in Fig. 6.20(b). The figure illustrates the evolution of amplified disturbances along the cycle, represented in terms of the phase angle  $\phi$  (see Fig. 4.4). The low-frequency content resembles the imposed motion frequency and harmonics. A band of amplified frequencies is observed, centred at  $f c / U_\infty \approx 15$ , which is analogous to that found for the static wing. However, for this same region, a magnitude drop is observed during part of the cycle. This is argued not to be caused by a change in the transition process occurring in the shear layer but simply by the change in relative distance between the transducer and the transition region as the LSB evolves along the cycle. This behaviour was already observed in the static characterization of the wing. For small incidence, as the bubble moves downstream, the transducer is immersed inside the bubble far from the transition region.

If there are no major changes in the dynamics of the LSB, the evolution of its location along the

plunging cycle can be tracked directly from the phase-averaged  $c_p$  distributions, as done previously for the pitching case. Fig. 6.21(a) shows phase-averaged static pressure coefficient distributions over the suction side of the wing at four phases along the cycle. The LSB characteristic locations, estimated following the methodology described in §5.1, are also indicated in the figure. Please note that, due to the downstream location of the bubble for  $\phi/\pi = 0$ , no information about the transition and reattachment locations could be extracted.

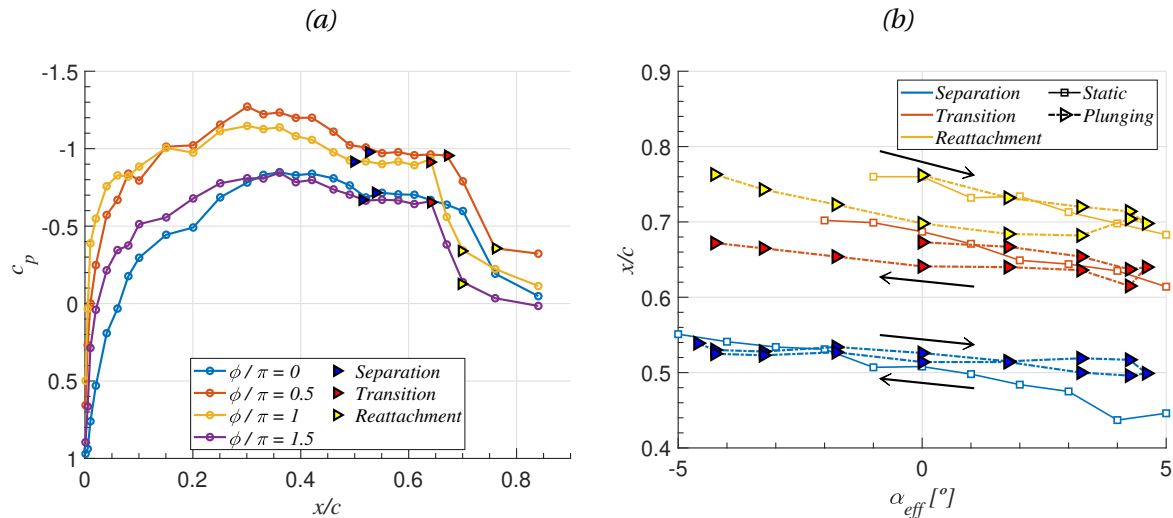


Figure 6.21: (a) Phase-averaged  $c_p$  distributions over the suction side of the wing at four phases along the sinusoidal plunging cycle. (b) LSB characteristic locations along the plunging cycle, extracted from the phase-averaged  $c_p$  distributions, compared to the static situation.

The  $c_p$  distributions reveal again a hysteresis in bubble location. For  $\phi/\pi = 0.5$  and  $\phi/\pi = 1.5$  (beginning of the downstroke and upstroke respectively, see Fig. 4.4), the wing has no vertical velocity and the effective angle of attack coincides with the nominal one,  $\alpha_{nom} = 0^\circ$ . The comparison of the detected characteristic locations reveals an upstream shift of the bubble for  $\phi/\pi = 1.5$ , where the effective incidence is decreasing. Qualitatively, this is a similar behaviour to that found for the pitching investigation, as illustrated, in Fig. 6.9. It is interesting to note that, while the hysteresis in lift coefficient with varying incidence changes from pitching (at least for the constant pitching rate studied here) to plunging configurations, the hysteresis in bubble location follows a similar trend. This suggests that the LSB dynamics are mainly driven by the relative change in incidence and the effect that this has on the adverse pressure gradient, as discussed by Ericsson and Reding [15].

The LSB characteristic locations extracted from the phase-averaged  $c_p$  distributions, at the 16 phases used to construct the experimental  $c_l$  presented earlier, are shown in Fig. 6.21(b). The locations extracted from the pressure taps in the static characterization of the LSB are also included for comparison. This gives a more clear picture of the hysteresis in bubble location between the upstroke and downstroke parts of the motion. The obtained results indicate very little change in separation location through the cycle, while transition and reattachment (where available) show a stronger hysteresis approximately around the static values. As for previous investigations, the lower distribution of pressure taps in the rear part of the wing limits the applicability of the method when the bubble moves downstream, as is the case for approximately one quarter of the sinusoidal cycle studied here.

### 6.3.2. Phase-averaged PIV measurements

For a better understanding of the evolution of the LSB, phase-averaged PIV is captured at the same 16 phases along the cycle. Contours of velocity magnitude are shown in Fig. 6.22(a) for the four phases discussed earlier using  $c_p$  distributions. As in the static characterization, the dividing stream-

line is used to estimate the separation and reattachment locations. To obtain the dividing streamline, the vertical velocity of the wing, as described by equation (4.3), needs to be subtracted from the measured velocity, to obtain the streamline in the frame of reference that moves with the wing. Transition is estimated from the maximum boundary layer shape factor inside the bubble.

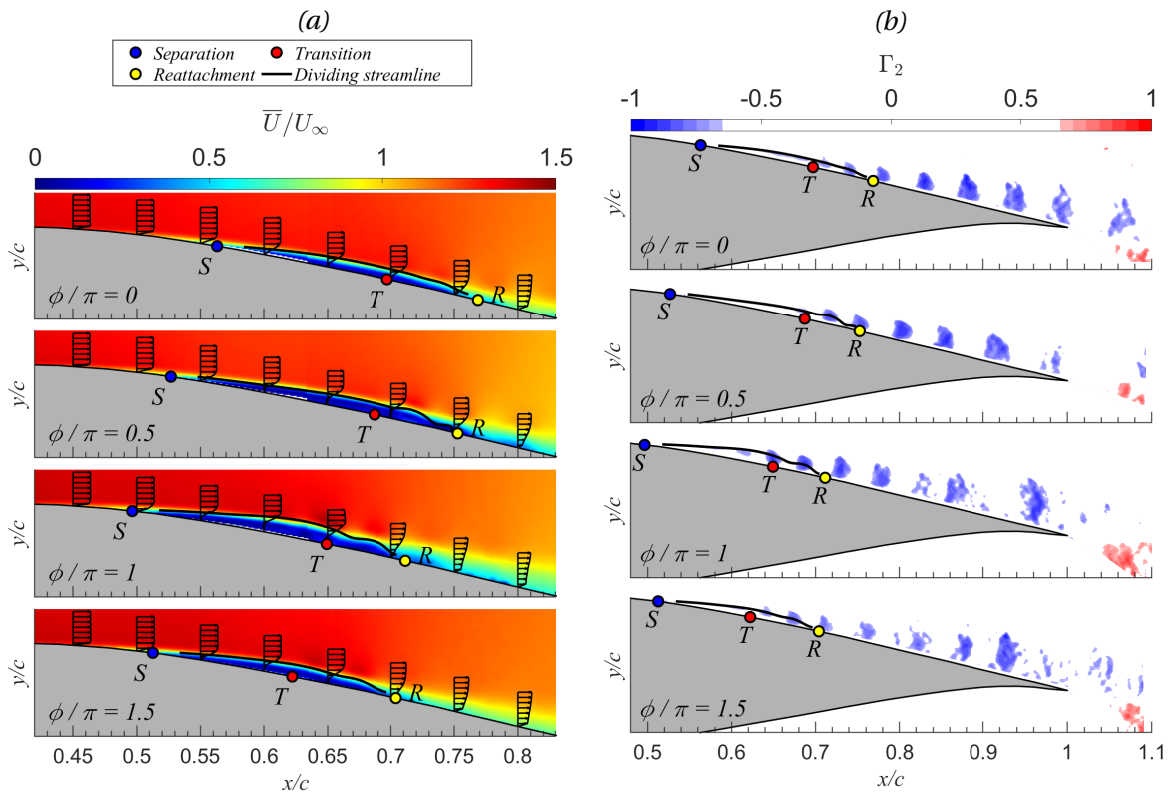


Figure 6.22: Contours of phase-averaged velocity magnitude with streamwise velocity boundary layer profiles (a), and visualization of coherent structures using the  $\Gamma_2$  vortex identification criterion (b), for four phases along the plunging cycle.

The LSB is observed to change in size and location along the cycle, as discussed for the static pressure coefficient. However, no bubble bursting (Gaster [23]) or major modification of the flow condition is found. In fact, the coherent structures shed in the separated shear layer as a result of the amplification of the Kelvin-Helmholtz instability are still visible during the plunging motion. These are visualized, from the phase-averaged PIV measurements, using the  $\Gamma_2$  vortex identification criterion. This method, first introduced by Graftieaux et al. [26], is a non-local, Galilean-invariant scheme. It is especially suited for two-dimensional experimental data, as it avoids the numerical differentiation involved with other more common criteria. The method is applied to the four phases along the cycle, as shown in Fig. 6.22(b). It helps to visualize how the coherent structures form in the shear layer, grow as they advect downstream due to viscous diffusion and finally break down into smaller turbulent scales.

Extending the methodology to the 16 phases measured returns the LSB characteristic locations shown in Fig. 6.23, in terms of the effective angle of attack of the wing induced by the plunging motion. The static locations obtained from the time-averaged PIV measurements are included for reference. The obtained locations describe a hysteresis cycle very similar to that obtained from the pressure taps, as shown in Fig. 6.21(b). Laminar separation shows a smaller hysteresis between the upstroke and downstroke motions than the other two locations. For transition and reattachment, the bubble generally moves downstream of the static location when the effective incidence is increasing, while the opposite occurs for decreasing incidence. This is analogous to the hysteresis

behaviour observed in the pitching investigation.

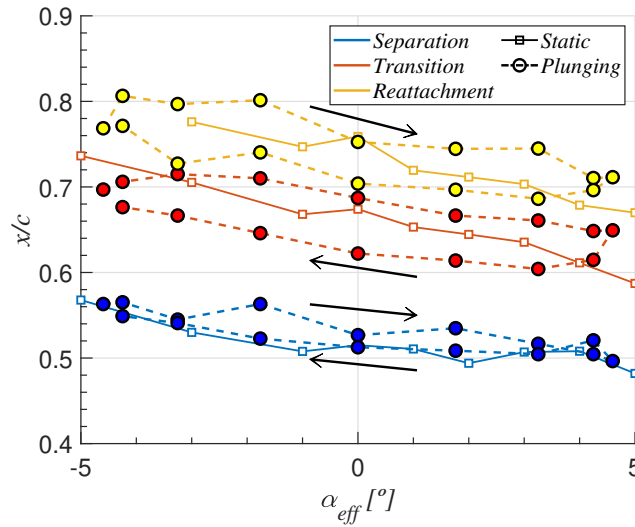


Figure 6.23: LSB characteristic locations along the sinusoidal plunging cycle extracted from phase-averaged PIV measurements, compared with the static characterization.

The comparison between the characteristic locations obtained along the plunging cycle using the  $c_p$  distributions and PIV is given in Fig. 6.24. As for the pitching investigation, a theoretical prediction is included in the comparison, based on the Theodorsen lift curve shown in Fig. 6.20(a) and quasi-steady IT measurements. In this case, the method was applied to all-three characteristic locations of the bubble, which are separated in the figure for improved visualization. As for lift coefficient, some deviation between theory and experiments is observed.

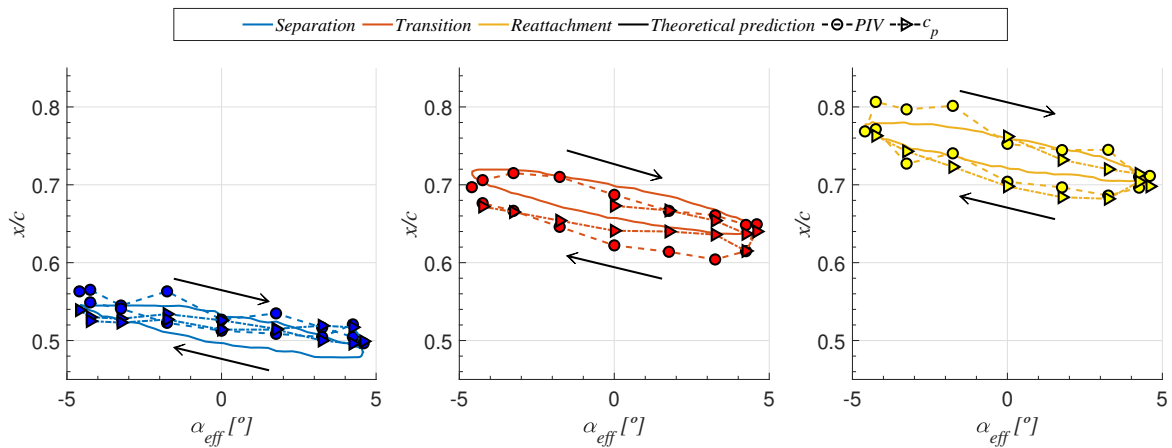


Figure 6.24: LSB characteristic locations along the sinusoidal plunging cycle extracted from phase-averaged PIV measurements,  $c_p$  distributions and theoretical prediction from linear unsteady theory.

There is reasonable agreement between the two experimental techniques for all-three locations measured. This confirms that both techniques are still suitable to study such an unsteady aerodynamic regime. The weak and smooth changes in bubble size and location cannot be responsible for the lift coefficient evolution along the cycle. Instead, it is postulated that the deviations from Theodorsen's theory are due to the non-linearities introduced by the thickness of the airfoil and the high combination of amplitude and frequency in the chosen plunging configuration.

### 6.3.3. Differential Infrared Thermography

So far, the characteristic locations of the LSB along the plunging cycle have been detected successfully using the pressure taps and the PIV measurements. This confirms that these techniques are not really affected by moderate levels of aerodynamic unsteadiness, as the same methodology was applied to static and unsteady situations. However, this may not be the case for the infrared approach. The ability to detect surface temperature changes with the infrared camera is directly related to the oscillating frequency imposed. The higher the aerodynamic unsteadiness, the smaller the temperature changes will be. For a given surface, there will be a certain frequency above which no temperature changes caused by the unsteady BL will be observed, and this will establish the maximum operating frequency for the infrared technique. As seen in the pitching investigation, this may not be as straightforward for the case of a LSB. The detection of the LSB characteristic locations involves three different processes, linked to very different levels of convective heat transfer. Furthermore, a strong effect of the direction of the motion could be observed, with pitch up promoting temperature changes. For the sinusoidal plunging motion considered in this section, incidence variation is a continuous process along the cycle. All things considered, the plunging experiment is clearly more complex for the infrared approach than the static or pitching investigations.

As discussed in §4.5, the infrared acquisition was started in the experiments after the surface temperature distribution had achieved a steady-state situation for the wing at the nominal angle of attack,  $\alpha_{nom} = 0^\circ$ , and the plunging mechanism had reached a uniform and smooth operation. Due to the high reduced frequency imposed, temperature changes are very small along the cycle, and thus the surface temperature distribution does not differ much from the steady-state version. The instantaneous infrared intensity distributions measured during the acquisition can also be phase-averaged (and spanwise-averaged, as for previous investigations) to the imposed motion to reduce camera noise. Fig. 6.25 shows phase-averaged infrared intensity distributions at the four phases discussed in detail with the other experimental techniques. The figure confirms the small changes between the different phases of the motion. The methodology employed to extract the location of laminar separation and transition from static distributions is applied, and represented by black lines in the figure, to indicate that these locations agree well with those measured for the static wing at  $\alpha = 0^\circ$  (see Fig. 6.5).

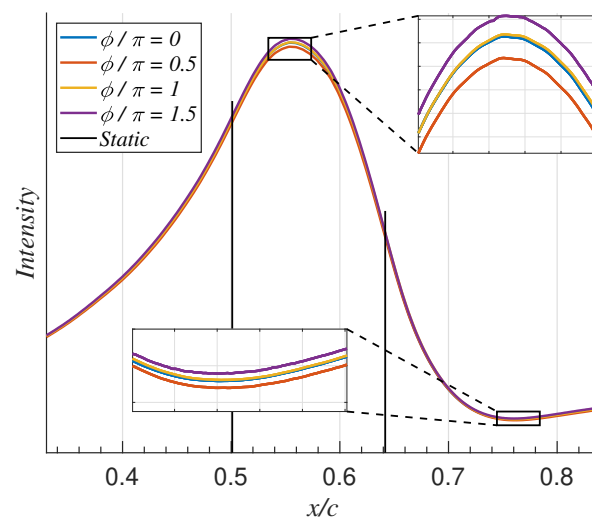


Figure 6.25: Phase-averaged infrared intensity distributions for the plunging wing at four phases along the cycle.

The slight temperature changes observed between phases, detailed in two different regions for improved visualization, do not follow the expected behaviour caused by the LSB moving upstream

and downstream along the cycle, as measured with the other techniques. For example, a hysteresis in bubble location was previously observed between  $\phi/\pi = 0.5$  and  $\phi/\pi = 1.5$ , for which  $\alpha_{eff} = 0^\circ$ , as indicated by Fig. 4.4. The bubble was further upstream for  $\phi/\pi = 1.5$ , where effective incidence is decreasing. With sufficient thermal response, the surface temperature distribution should indicate this upstream shift. Instead, Fig. 6.25 shows higher intensity at  $\phi/\pi = 1.5$  at every location along the wing, while the opposite occurs for  $\phi/\pi = 0.5$ . This is argued to be caused by the change in distance between the wing and the infrared camera along the plunging motion. The argument is supported by the fact that the infrared intensity distributions are nearly identical for  $\phi/\pi = 0$  and  $\phi/\pi = 1$ , when the wing is at the same physical location (mid-upstroke and mid-downstroke respectively).

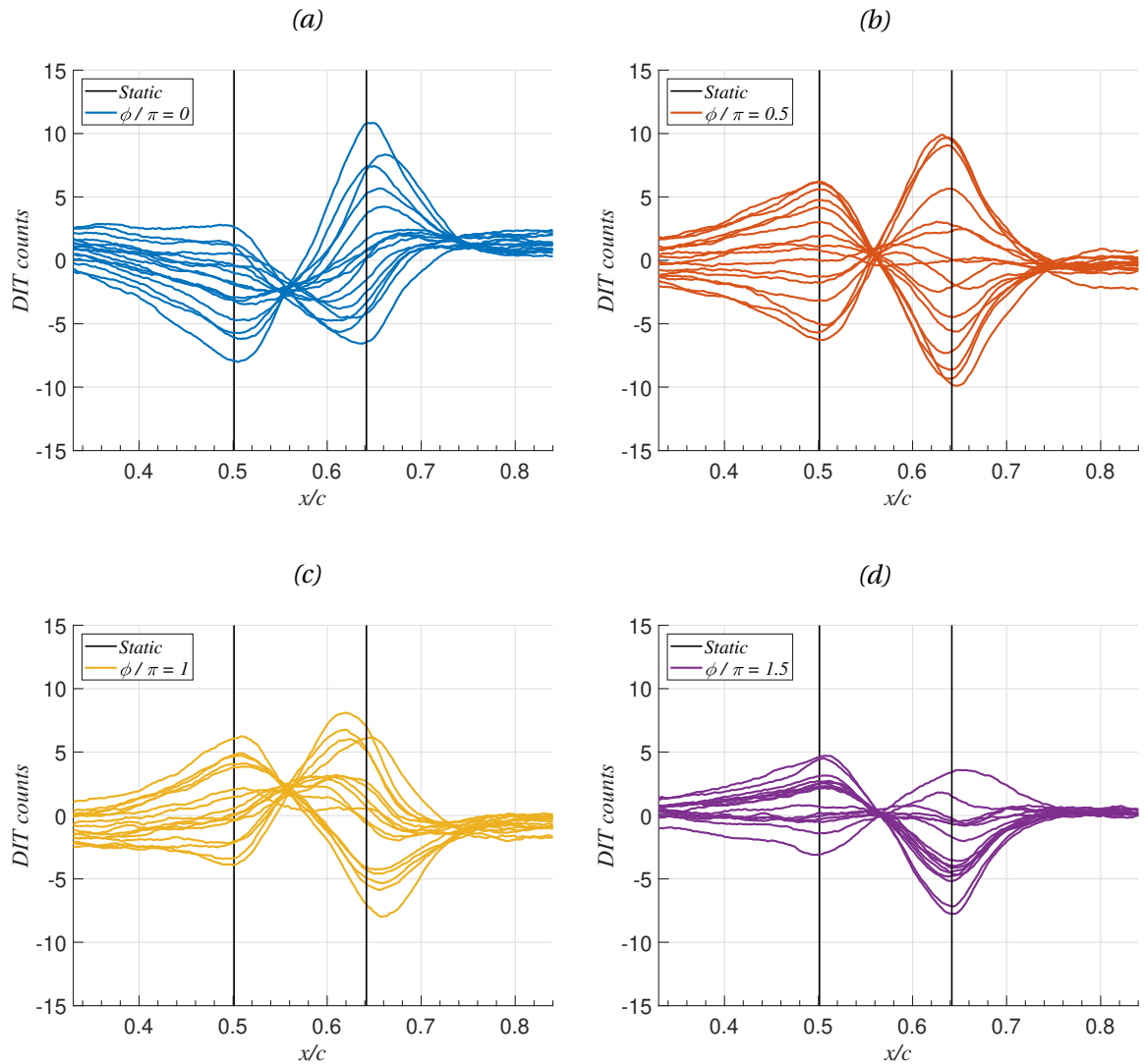


Figure 6.26: DIT curves for the plunging wing at: (a)  $\phi/\pi = 0$ , (b)  $\phi/\pi = 0.5$ , (c)  $\phi/\pi = 1$  and (d)  $\phi/\pi = 1.5$ .

As expected, no meaningful information about the instantaneous BL state may be derived directly from the infrared intensity distributions. Instead, the DIT approach is considered in the following. The methodology needs to be adapted slightly to this experiment. While the time separation between DIT frames was chosen in the pitching investigation based on the change in incidence, now this represents a change in phase angle or effective incidence. For the plunging configuration studied here, constructing DIT curves from consecutive frames is sufficient to detect changes. The phase of the DIT solution is considered to be the mean of that of the two frames considered, in an analogous manner to the previous approach. Following this description, Fig. 6.26 contains 16 different

DIT curves constructed from the infrared acquisition for each of the four phases along the plunging cycle discussed above. A similar pattern is observed for the four phases considered, containing DIT peaks around the locations extracted from the static IT approach applied to the phase-averaged infrared intensity distributions in Fig. 6.25. For a DIT curve governed by the unsteady movement of the LSB, all-sixteen curves of each phase should collapse, or at least describe a similar behaviour. The changes observed between analogous curves indicate that these DIT peaks are linked to the separation and transition processes for the wing at the nominal angle of attack. This behaviour was already observed in the pitching investigation, especially during pitch down, as indicated for example in Fig. 6.15(b).

These erroneous DIT features obscure the possible temperature changes caused by the unsteady LSB, making it impossible to detect its evolution along the cycle. This confirms that the current plunging configuration contains a level of aerodynamic unsteadiness that cannot be studied with DIT, given the surface properties of the wing. The same conclusion could be already made from the analytical thermal model discussed in §5.3.4. The comparison between the experiments conducted by DLR and the present study, as illustrated by Fig. 5.14, suggests that, for similar motion frequencies, the lower convective heat transfer associated with the presence of a LSB may compromise the applicability of the DIT method. The plunging configuration studied here, characterized by  $k = 0.67$ , corresponds to a dimensional frequency of 7.52 Hz. This value is close to the maximum one tested by Richter et al. [65], but for a much higher Reynolds number environment. The only way of improving the current results and considering the DIT method to detect an unsteady LSB is to modify the surface properties of the aerodynamic surface. As indicated by equation (5.27) and the simulations of Gardner et al. [18], the thermal capacity of the surface may be reduced for an improved thermal response. However, the current investigation already tried to make use of materials with appropriate thermal properties, and significant improvements would only be possible when considering more exotic ones, which are hard to conceive for aerospace structural applications.

In summary, the unsteady evolution of the LSB along the plunging cycle could only be detected from the pressure taps and the PIV measurements. Both techniques indicate a hysteresis in the characteristic locations of the LSB between the upstroke and downstroke parts of the motion, especially for transition and turbulent reattachment. While the methodology applied for these techniques is not severely influenced by the aerodynamic unsteadiness imposed by the structural motion, the rapid plunging configuration studied compromised the infrared approach entirely. The application of the DIT method, designed to overcome the thermal limitations of the aerodynamic surface, only shows erroneous features associated with the static bubble. No temperature changes caused by the unsteady LSB could be detected, making it impossible to track its evolution along the sinusoidal cycle.



# 7

## Conclusion

The final chapter of the thesis summarizes the main outcomes of the experimental research project. The LSB that forms on the suction side of a modified NACA 6-series airfoil at a chord-based Reynolds number of  $Re = 200k$  has been studied in a series of WT experiments conducted at The University of Arizona. In the experiments, three different flow measurement techniques have been used to study the LSB: surface pressure measurements (pressure taps and a high-bandwidth pressure transducer), two-dimensional PIV and Infrared Thermography. The presence and nature of the bubble may be addressed from the identification of three characteristic locations that define this flow feature: the separation of a laminar BL, a transition-to-turbulence process in the separated shear layer formed after flow separation and the subsequent reattachment of a turbulent BL. The three techniques considered here have been used to detect the characteristic locations of the LSB in a time-averaged sense. Their suitability for this purpose is directly linked to the research objective of the thesis, as introduced in section §1.1 and reproduced below for simplicity:

“Investigate the strengths and weaknesses of three different flow measurement techniques—surface pressure measurements, Particle Image Velocimetry and Infrared Thermography—to detect the location of an unsteady Laminar Separation Bubble”.

As mentioned in the research objective, the aim of the project is to study the effects that aerodynamic unsteadiness have on the behaviour of the bubble. This problem was first simplified to a static characterization of the LSB. This has been widely studied, both using experiments and numerical simulations, thus giving a perfect reference to validate the capabilities of the experimental techniques considered here. The main outcomes of this investigation are summarized in section §7.1.

The effects of aerodynamic unsteadiness have been explored in two different experiments, by imposing two types of structural motion to the wing inside the WT. A first, simpler situation, was to study a pitching-type motion, considering a constant pitching rate. This enables to modify the unsteadiness of the aerodynamic problem by simply changing the pitching rate of the motion. The experiment was used to study various levels of unsteadiness, to understand the effects on the bubble and also the influence on the experimental measurements. The approach was then extended to study a sinusoidal plunging-type motion, of increased frequency, in the context of a research project at The University of Arizona involving also flight tests and high-fidelity numerical simulations. The methodologies applied to the pitching case were also considered for this investigation, providing information about the location of the LSB along the plunging cycle. Section §7.2 summarizes the unsteady investigations, covering the behaviour of the LSB and the performance of the experimental techniques employed.

Successful WT experiments clearly benefit from past experiences involving the use of similar techniques or the study of related flow phenomena. The knowledge acquired during the experimental campaigns related to the work of this thesis served to provide some recommendations for future experiments, as discussed in section §7.3.

### 7.1. Static characterization of a LSB

The LSB was first characterized over a range of static angles of attack, using one-degree increments, between  $-5^\circ \leq \alpha \leq 7^\circ$ . Regarding the pressure taps and PIV, methodologies extracted from the available literature were used to identify the three characteristic locations of interest. Both techniques indicated an upstream shift of the bubble with increasing incidence, while the size was kept approximately constant. The pressure taps approach was partially unsuccessful at negative incidences due to the limited availability of taps in the region of the bubble, whereas PIV showed higher uncertainty in the detection of laminar separation due to laser reflections at the surface and limited spatial resolution in that region. Apart from this, there was excellent agreement in the locations detected with both techniques, showing deviations of less than 2% of the airfoil chord.

Regarding the infrared approach, two different methodologies were employed in the static characterization of the bubble. The first, based directly on the time-averaged infrared measurements, was a slight modification of a recently-explored method. This method links the surface temperature that can be measured with an infrared camera to the BL state around the bubble following results from a DNS. The novel approach considered here was to eliminate the need for temperature calibration of the camera, relying only on the infrared intensity collected with the sensor. In the experiments, the wing was heated with an external source to enhance convection with the flow. The small amount of heating used causes only minor temperature changes, and therefore the assumption of a linear relation between infrared intensity and surface temperature holds. The characteristic locations obtained from this method show excellent agreement with those from the pressure taps and PIV, thus validating the simplified approach.

The second option considered was to explore the use of Differential Infrared Thermography (DIT). This technique has been recently proposed by DLR to study unsteady phenomena, such as BL transition over a pitching wing, with an infrared camera. To overcome the limited thermal response of the aerodynamic surface, the method identifies unsteady features from the subtraction of closely-obtained thermograms. This can be applied to study static phenomena by choosing thermograms corresponding to different static incidences. The DIT method has been extended in this thesis to the case of a LSB, detecting the three characteristic locations in excellent agreement with the other techniques.

Of the three techniques employed, IT can be considered the ideal choice for the static characterization of the bubble. The technique provides direct information at the surface, is simpler to prepare and operate than PIV, has greater spatial resolution than the taps and could be easily extended to study a three-dimensional bubble.

### 7.2. Unsteady behaviour of a LSB subjected to wing structural motion

The methodology employed to detect the LSB characteristic locations from the pressure taps and PIV can be equally applied to the unsteady cases studied here. Both for the pitching and plunging investigations, a hysteresis in bubble location could be measured with these techniques. For increasing (decreasing) incidence, the bubble was observed to move downstream (upstream) with respect to the static case at the same angle of attack. This behaviour is argued to be caused by the effect of the unsteadiness on the adverse pressure gradient, which can promote or delay the separation of the laminar BL. For the pitching case, both techniques found a similar increase in hysteresis when increasing the reduced frequency of the structural motion imposed.

The DIT method is more heavily affected by aerodynamic unsteadiness. Temperature changes

at the surface are governed not only by the unsteady convective heat transfer but also by the thermal capacity of the surface material. Furthermore, the low Reynolds number of the present investigation is associated with low levels of convection with the flow, thus establishing the most complicated scenario for DIT studied so far. The extension of the DIT method, which could detect the three characteristic locations in the static characterization, was only successful in the pitching experiment for extremely low levels of unsteadiness, such that the surface temperature behaved in a quasi-steady manner. For true unsteady regimes, only the effects of the unsteady transition location could be detected. The hysteresis in transition location was also observed with DIT, but showed greater values than with the other techniques considered. This is in agreement with previous studies involving the use of DIT for unsteady transition detection, and is argued to be caused by the thermal lag of the aerodynamic surface.

A different behaviour was observed between the pitch up and pitch down parts of the pitching motion. A stronger DIT signal was measured during pitch up, caused by the surface cooling of the turbulent BL as the bubble moved upstream. This made it possible to apply DIT for all reduced frequencies tested, up to  $k = 0.25$ . However, during pitch down transition moves downstream causing that region to slightly warm up as it gets inside the bubble. This was seen to be less efficient, and the applicability of the method was limited to  $k \leq 0.05$ .

For the plunging investigation, of higher aerodynamic unsteadiness than the pitching one ( $k = 0.67$ ), the DIT method could not even detect the unsteady transition location. The DIT signal was dominated by erroneous features linked to the steady-state temperature distribution, which obscured the effects of the unsteady bubble. This confirms that the applicability of the DIT method is compromised in highly unsteady situations and/or those with low levels of convective heat transfer.

The limitations of the DIT technique for the current investigation could already be partially predicted from a simple analysis of the thermal response of an unsteady surface. An analytical model was built to compare existing results, from a higher convective heat transfer environment, with the case of a LSB. This allowed expressing the thermal response in terms of a non-dimensional group,  $FoBi$ , that involves surface properties, convective heat transfer level and aerodynamic unsteadiness.

Going back to the research objective, it is clear that the infrared technique suffered the biggest change when switching from static to unsteady LSBs. While the accuracy of the surface pressure measurements and PIV remained comparable between investigations, the applicability of the DIT method dropped for the unsteady regime. The method could only detect one of the three unsteady characteristic locations of the bubble, and for very limited levels of aerodynamic unsteadiness. The low heat transfer associated with the presence of a LSB compromised the approach, at least when considering the thermal response of common materials used for aerospace manufacturing.

### 7.3. Recommendations for future work

Lastly, a couple of basic recommendations for future experiments on a similar topic are given in this section. Regarding the use of pressure taps, the methodology employed to detect the characteristic locations of the LSB requires a thin distribution of taps in the region of the bubble. This is especially true for the transition region, due to the strong pressure change that follows this process. For static investigations, Xfoil predictions can give a good estimation of the location of the bubble that can help place the pressure taps in the experimental models.

With respect to PIV, the recommendation given here is a popular one for this technique. As the accurate location of the bubble involves the calculation of a streamline that intersects with the surface, this requires special attention. Surface preparation is key to minimize laser reflections that may corrupt the results in this region. In the experiments, the wing surface was continuously damaged by the laser light, and the effects could be clearly observed by comparing the first and last frames of every acquisition. A black marker was used to slightly repaint the surface in between acquisitions,

but the search for a better method is something worth considering.

The possible improvement of the results obtained with the infrared technique is very much linked to the use of a better thermal insulator at the surface. The thin foil added to the skin of the wing made a big improvement but could not prevent the existence of some heat transfer by conduction into the inner structure. It may be worth exploring the use of stronger insulators, such as foams (see for example the recent experiments of Jagerhofer et al. [38]), to study the thermal response of the surface to the aerodynamic unsteadiness. The pitching-type experiment is a good candidate to quickly try a couple of different options, as it enables a fast change of the unsteady situation.

# Bibliography

- [1] M. A. Agate, J. Little, H. Fasel, and A. Gross. Oscillatory plunging motion applied to an airfoil near stall. *AIAA SciTech Forum - 55th AIAA Aerospace Sciences Meeting*, 2017. doi: 10.2514/6.2017-0998.
- [2] M. A. Agate, A. Pande, J. C. Little, H. F. Fasel, and A. Gross. Active flow control of the laminar separation bubble on an oscillating airfoil near stall. *AIAA Aerospace Sciences Meeting*, 2018. doi: 10.2514/6.2018-2049.
- [3] T. Astarita and G. M. Carlomagno. *Infrared Thermography for Thermo-Fluid-Dynamics*. Springer-Verlag Berlin Heidelberg, 2013. ISBN 9783642295072. doi: 10.1007/978-3-642-29508-9.
- [4] W. Balzer and H. F. Fasel. Numerical investigation of the role of free-stream turbulence in boundary-layer separation. *Journal of Fluid Mechanics*, 801:289–321, 2016. ISSN 14697645. doi: 10.1017/jfm.2016.424.
- [5] T. L. Bergman and A. S. Lavine. *Fundamentals of Heat and Mass Transfer*. John Wiley & Sons, Inc., 8 edition, 2017. ISBN 9781119320425.
- [6] H. Blasius. Grenzschichten in Flüssigkeiten mit kleiner Reibung. *Zeitschrift für Mathematik und Physik*, 56(1):1–37, 1908.
- [7] D. Borgmann, S. Hosseinverdi, J. Little, and H. Fasel. Investigation of low-speed boundary-layer instability and transition using experiments, theory and DNS. *AIAA Aviation Forum*, 2020. doi: 10.2514/6.2020-2948.
- [8] D. Borgmann, S. Hosseinverdi, J. Little, and H. F. Fasel. Active control of boundary-layer transition in laminar separation bubbles. In *AIAA SciTech 2022 Forum*, 2022.
- [9] M. S. Boutilier and S. Yarusevych. Parametric study of separation and transition characteristics over an airfoil at low Reynolds numbers. *Experiments in Fluids*, 52(6):1491–1506, 2012. ISSN 07234864. doi: 10.1007/s00348-012-1270-z.
- [10] J. M. Brandon, G. S. Manuel, R. E. Wright Jr., and B. J. Holmes. In-Flight Flow Visualization Using Infrared Imaging. *Journal of Aircraft*, 27(6):612–618, 1990. ISSN 26883627. doi: 10.4271/911006.
- [11] S. Burgmann and W. Schröder. Investigation of the vortex induced unsteadiness of a separation bubble via time-resolved and scanning PIV measurements. *Experiments in Fluids*, 45(4):675–691, 2008. ISSN 07234864. doi: 10.1007/s00348-008-0548-7.
- [12] S. Burgmann, J. Dannemann, and W. Schröder. Time-resolved and volumetric PIV measurements of a transitional separation bubble on an SD7003 airfoil. *Experiments in Fluids*, 44(4):609–622, 2008. ISSN 07234864. doi: 10.1007/s00348-007-0421-0.
- [13] L. de Luca, G. M. Carlomagno, and G. Buresti. Boundary layer diagnostics by means of an infrared scanning radiometer. *Experiments in Fluids*, 9:121 – 128, 1990.

- [14] C. Dollinger, M. Sorg, N. Balaresque, and A. Fischer. Measurement uncertainty of IR thermographic flow visualization measurements for transition detection on wind turbines in operation. *Experimental Thermal and Fluid Science*, 97:279–289, 2018. ISSN 0894-1777. doi: 10.1016/j.expthermflusci.2018.04.025.
- [15] L. E. Ericsson and J. P. Reding. Fluid mechanics of dynamic stall part I. Unsteady flow concepts. *Journal of Fluids and Structures*, 2(1):1–33, 1988. ISSN 10958622. doi: 10.1016/S0889-9746(88)90116-8.
- [16] N. Fujisawa, Y. Oguma, and T. Nakano. Measurements of wall-shear-stress distribution on an NACA0018 airfoil by liquid-crystal coating and near-wall particle image velocimetry (PIV). *Measurement Science and Technology*, 20(6), 2009. ISSN 13616501. doi: 10.1088/0957-0233/20/6/065403.
- [17] A. D. Gardner, C. C. Wolf, and M. Raffel. A new method of dynamic and static stall detection using infrared thermography. *Experiments in Fluids*, 57(9):1–13, 2016. ISSN 07234864. doi: 10.1007/s00348-016-2235-4.
- [18] A. D. Gardner, C. Eder, C. C. Wolf, and M. Raffel. Analysis of differential infrared thermography for boundary layer transition detection. *Experiments in Fluids*, 58(9):1–14, 2017. ISSN 07234864. doi: 10.1007/s00348-017-2405-z.
- [19] A. D. Gardner, C. B. Merz, and C. C. Wolf. Effect of sweep on a pitching finite wing. *Journal of the American Helicopter Society*, 64(3):1–13, 2019. ISSN 00028711. doi: 10.4050/JAHS.64.032007.
- [20] A. D. Gardner, C. C. Wolf, and M. Raffel. Review of measurement techniques for unsteady helicopter rotor flows. *Progress in Aerospace Sciences*, 111(June), 2019. ISSN 03760421. doi: 10.1016/j.paerosci.2019.100566.
- [21] A. D. Gardner, C. C. Wolf, J. T. Heineck, M. Barnett, and M. Raffel. Helicopter rotor boundary layer transition measurement in forward flight using an infrared camera. *The Vertical Flight Society - Forum 75: The Future of Vertical Flight - Proceedings of the 75th Annual Forum and Technology Display*, 012002:1–13, 2020. ISSN 2161-6027. doi: 10.4050/jahs.65.012002.
- [22] E. Gartenberg and A. S. Roberts. Twenty-five years of aerodynamic research with infrared imaging. *Journal of Aircraft*, 29(2):161–171, 1992. ISSN 00218669. doi: 10.2514/3.46140.
- [23] M. Gaster. The Structure and Behaviour of Laminar Separation Bubbles. *Aeronautical Research Council Reports and Memoranda*, 3595:1–31, 1967.
- [24] R. Gerakopoulos, M. S. H. Boutilier, and S. Yarusevych. Aerodynamic Characterization of a NACA 0018 Airfoil at Low Reynolds Numbers. *Fluid Dynamics Conference and Exhibit*, 40th(July):1–13, 2010.
- [25] F. Ghorbanishohrat and D. Johnson. Evaluating airfoil behaviour such as laminar separation bubbles with visualization and IR thermography methods. *Journal of Physics: Conference Series PAPER*, 1037, 2018.
- [26] L. Graftieaux, M. Michard, and G. Nathalie. Combining PIV, POD and vortex identification algorithms for the study of unsteady turbulent swirling flows. *Measurement Science and Technology*, 12(9):1422–1429, 2001. ISSN 09570233. doi: 10.1088/0957-0233/12/9/307.
- [27] A. Grille Guerra, S. Hosseinverdi, A. Singh, J. Little, and H. Fasel. Unsteady Evolution of a Laminar Separation Bubble Subjected to Structural Motion. *AIAA Aviation Forum*, pages 1–18, 2021. doi: 10.2514/6.2021-2949.

- [28] A. Grille Guerra, S. Hosseinverdi, J. Little, and H. F. Fasel. Unsteady Behavior of a Laminar Separation Bubble Subjected to Wing Structural Motion. *AIAA SciTech Forum*, pages 1–17, 2022. doi: 10.2514/6.2022-2331.
- [29] T. Hetsch and U. Rist. Accuracy of local and nonlocal linear stability theory in swept separation bubbles. *AIAA Journal*, 47(5):1116–1122, 2009.
- [30] K. H. Horstmann, A. Quast, and G. Redeker. Flight and wind-tunnel investigations on boundary-layer transition. *Journal of Aircraft*, 27(2):146–150, 1990. ISSN 00218669. doi: 10.2514/3.45910.
- [31] H. Horton. *Laminar Separation Bubbles in Two and Three Dimensional Incompressible Flow*. PhD thesis, University of London, 1968.
- [32] S. Hosseinverdi and H. F. Fasel. Direct numerical simulations of laminar-to-turbulent transition in laminar separation bubbles in three-dimensional boundary-layer. In *46th AIAA Fluid Dynamics Conference, AIAA 2016-3793*, 2016.
- [33] S. Hosseinverdi and H. F. Fasel. Role of Klebanoff modes in active flow control of separation: direct numerical simulations. *J. Fluid Mech.*, 850:954–983, 2018.
- [34] S. Hosseinverdi and H. F. Fasel. Numerical investigation of laminar-turbulent transition in laminar separation bubbles: the effect of free-stream turbulence. *J. Fluid Mech.*, 858:714–759, 2019.
- [35] S. Hosseinverdi and H. F. Fasel. High-Order Accurate Incompressible Navier-Stokes Solver Based on Vorticity-Velocity Formulation for Orthogonal Curvilinear Grids. *AIAA Aviation Forum*, 2021. doi: 10.2514/6.2021-2741.
- [36] S. Hosseinverdi, W. Balzer, and H. F. Fasel. Direct numerical simulations of the effect of free-stream turbulence on ‘long’ laminar separation bubbles. In *42th AIAA Fluid Dynamics Conference and Exhibit, AIAA 2012-2972*, 2012.
- [37] S. Hosseinverdi, A. Grille Guerra, H. F. Fasel, and J. Little. Investigation of Transition and its Active Control in Separation Bubbles for a Wing Section at Re=200k: DNS, Theory, and Experiments. *AIAA SciTech Forum*, pages 1–21, 2022. doi: 10.2514/6.2022-2329.
- [38] P. Jagerhofer, J. Woisetschläger, G. Erlacher, and E. Göttlich. Heat transfer and film cooling measurements on aerodynamic geometries relevant for turbomachinery. *SN Applied Sciences*, 3(12), 2021. ISSN 25233971. doi: 10.1007/s42452-021-04845-5.
- [39] L. A. Joseph, A. Borgoltz, and W. Devenport. Infrared thermography for detection of laminar-turbulent transition in low-speed wind tunnel testing. *Experiments in Fluids*, 57(5):1–13, 2016. ISSN 07234864. doi: 10.1007/s00348-016-2162-4.
- [40] D. H. Kim and J. W. Chang. Unsteady boundary layer for a pitching airfoil at low Reynolds numbers. *Journal of Mechanical Science and Technology*, 24(1):429–440, 2010. ISSN 1738494X. doi: 10.1007/s12206-009-1105-x.
- [41] J. W. Kurelek, B. A. Tuna, S. Yarusevych, and M. Kotsonis. Three-Dimensional Development of Coherent Structures in a Two-Dimensional Laminar Separation Bubble. *AIAA Journal*, 59(2): 1–13, 2020. ISSN 0001-1452. doi: 10.2514/1.j059700.
- [42] M. Lang, U. Rist, and S. Wagner. Investigations on controlled transition development in a laminar separation bubble by means of LDA and PIV. *Experiments in Fluids*, 36(1):43–52, 2004. ISSN 07234864. doi: 10.1007/s00348-003-0625-x.

- [43] T. Lee and S. Basu. Measurement of unsteady boundary layer developed on an oscillating airfoil using multiple hot-film sensors. *Experiments in Fluids*, 25(June 1997):108–117, 1998.
- [44] J. G. Leishman. *Principles of Helicopter Aerodynamics*. Cambridge University Press, second edition, 2006.
- [45] J. M. Lilly. Element analysis: A wavelet-based method for analysing time-localized events in noisy time series. *Proceedings of the Royal Society A: Mathematical, Physical and Engineering Sciences*, 473(2200), 2017. ISSN 14712946. doi: 10.1098/rspa.2016.0776.
- [46] L. M. Mack. Transition and laminar instability. *JPL Publication 77-15*, 1977.
- [47] W. J. McCroskey. The Phenomenon of Dynamic Stall. *NASA Technical Memorandum*, 81264: 1–28, 1981.
- [48] C. Mertens, C. C. Wolf, A. D. Gardner, F. F. Schrijer, and B. W. Van Oudheusden. Advanced infrared thermography data analysis for unsteady boundary layer transition detection. *Measurement Science and Technology*, 31(1), 2020. ISSN 13616501. doi: 10.1088/1361-6501/ab3ae2.
- [49] T. Michelis, S. Yarusevych, and M. Kotsonis. Response of a laminar separation bubble to impulsive forcing. *Journal of Fluid Mechanics*, 820:633–666, 2017. ISSN 14697645. doi: 10.1017/jfm.2017.217.
- [50] M. Miozzi, A. Capone, M. Costantini, L. Fratto, C. Klein, and F. Di Felice. Skin friction and coherent structures within a laminar separation bubble. *Experiments in Fluids*, 60(1):1–25, 2019. ISSN 07234864. doi: 10.1007/s00348-018-2651-8.
- [51] R. J. Moffat. Describing the uncertainties in experimental results. *Experimental Thermal and Fluid Science*, 1(1):3–17, 1988. ISSN 08941777. doi: 10.1016/0894-1777(88)90043-X.
- [52] A. Nati, R. de Kat, F. Scarano, and B. W. van Oudheusden. Dynamic pitching effect on a laminar separation bubble. *Experiments in Fluids*, 56(9):1–17, 2015. ISSN 07234864. doi: 10.1007/s00348-015-2031-6.
- [53] M. M. O’Meara and T. J. Mueller. Experimental Determination of the Laminar Separation Bubble Characteristics of an Airfoil At Low Reynolds Numbers. *AIAA Paper*, 25(8), 1986. ISSN 01463705. doi: 10.2514/6.1986-1065.
- [54] A. D. Overmeyer and P. B. Martin. Measured boundary layer transition and rotor Hover performance at model scale. *AIAA SciTech Forum - 55th AIAA Aerospace Sciences Meeting*, 2017. doi: 10.2514/6.2017-1872.
- [55] P. R. Owen and L. Klanfer. On the Laminar Boundary Layer Separation from the Leading edge of a Thin Aerofoil. *ARC Technical Report 220*, 1955.
- [56] M. Pascazio, J. M. Autric, D. Favier, and C. Maresca. Unsteady boundary-layer measurement on oscillating airfoils: Transition and separation phenomena in pitching motion. *34th Aerospace Sciences Meeting and Exhibit*, 1996. doi: 10.2514/6.1996-35.
- [57] D. J. Peake, A. J. Bowker, S. J. Lockyear, and E. A. Ellis. Non-Obtrusive Detection of Transition Region Using an Infra-Red Camera. *AGARD ConfProc*, 224, 1977.
- [58] L. Prandtl. Über Flüssigkeitsbewegung bei sehr kleiner Reibung. *III. Internationaler Mathematiker-Kongress*, pages 575–584, 1904. doi: 10.1007/978-3-662-11836-8\_43.

- [59] A. W. Quast. Detection of Transition By Infrared Image Techniques. *ICIASF Record, International Congress on Instrumentation in Aerospace Simulation Facilities*, 3(1):125–134, 1987. ISSN 07302010.
- [60] M. Raffel and C. B. Merz. Differential infrared thermography for unsteady boundary-layer transition measurements. *AIAA Journal*, 52(9):2090–2093, 2014. ISSN 00011452. doi: 10.2514/1.J053235.
- [61] M. Raffel, C. B. Merz, T. Schwermer, and K. Richter. Differential infrared thermography for boundary layer transition detection on pitching rotor blade models. *Experiments in Fluids*, 56(2):1–13, 2015. ISSN 07234864. doi: 10.1007/s00348-015-1905-y.
- [62] M. Raffel, A. D. Gardner, T. Schwermer, C. B. Merz, A. Weiss, J. Braukmann, C. C. Wolf, and B. Ewers. Differential Infrared Thermography ( DIT ) for Dynamic Stall Detection. In *18th International Symposium on the Application of Laser and Imaging Techniques to Fluid Mechanics*, 2016.
- [63] R. Ricci and S. Montelpare. A quantitative IR thermographic method to study the laminar separation bubble phenomenon. *International Journal of Thermal Sciences*, 44:709–719, 2005. doi: 10.1016/j.ijthermalsci.2005.02.013.
- [64] K. Richter, E. Schiilein, B. Ewers, J. Raddatz, and A. Klein. Boundary layer transition characteristics of a full-scale helicopter rotor in hover. *Annual Forum Proceedings - AHS International*, 1(December):482–486, 2016. ISSN 15522938.
- [65] K. Richter, C. C. Wolf, A. D. Gardner, and C. B. Merz. Detection of unsteady boundary layer transition using three experimental methods. *54th AIAA Aerospace Sciences Meeting*, 0(January): 1–22, 2016. doi: 10.2514/6.2016-1072.
- [66] D. Rudmin, A. Benaissa, and D. Poirel. Detection of laminar flow separation and transition on a NACA-0012 airfoil using surface hot-films. *Journal of Fluids Engineering, Transactions of the ASME*, 135(10):1–6, 2013. ISSN 00982202. doi: 10.1115/1.4024807.
- [67] H. Schlichting and K. Gersten. *Boundary Layer Theory*. Springer Berlin Heidelberg, 9 edition, 2017. ISBN 9783662529171.
- [68] J. Shi and C. Tomasi. Good features to track. *1994 Proceedings of IEEE Conference on Computer Vision and Pattern Recognition*, pages 593–600, 1994. ISSN 10643745. doi: 10.1385/1-59259-240-6:255.
- [69] B. Simon, A. Filius, C. Tropea, S. Grundmann, and B. Simon. IR thermography for dynamic detection of laminar turbulent transition. *Experiments in Fluids*, 57(5):1–12, 2016. ISSN 1432-1114. doi: 10.1007/s00348-016-2178-9.
- [70] P. R. Spalart and M. K. Strelets. Mechanisms of transition and heat transfer in a separation bubble. *Journal of Fluid Mechanics*, 403:329–349, 2000. ISSN 00221120. doi: 10.1017/S0022112099007077.
- [71] P. W. Stallings and D. B. Carver. Infrared and Phase-Change Paint Measurements of Heat Transfer on the Space Shuttle Orbiter. AEDC-TSR-78-V13. Technical report, Arnold Engineering Development Center, 1978.
- [72] I. Tani. Low-speed flows involving bubble separations. *Progress in Aerospace Sciences*, 5(C): 70–103, 1964. ISSN 03760421. doi: 10.1016/0376-0421(64)90004-1.

- [73] T. Theodorsen. General Theory of Aerodynamic Instability and the Mechanism of Flutter. Technical Report 496, NASA RP-1050, 1949.
- [74] A. Uranga, P. O. Persson, M. Drela, and J. Peraire. Implicit Large Eddy Simulation of transition to turbulence at low Reynolds numbers using a Discontinuous Galerkin method. *International Journal for Numerical Methods in Engineering*, 87(1-5):232–261, 2011. ISSN 00295981. doi: 10.1002/nme.3036.
- [75] J. L. Van Ingen. The eN method for transition prediction. Historical review of work at TU Delft. *38th AIAA Fluid Dynamics Conference and Exhibit*, pages 1–49, 2008. doi: 10.2514/6.2008-3830.
- [76] M. R. Visbal, R. E. Gordnier, and M. C. Galbraith. High-fidelity simulations of moving and flexible airfoils at low Reynolds numbers. *Experiments in Fluids*, 46(5):903–922, 2009. ISSN 07234864. doi: 10.1007/s00348-009-0635-4.
- [77] S. von Hoesslin, M. Stadlbauer, J. Gruendmayer, and C. J. Kähler. Temperature decline thermography for laminarturbulent transition detection in aerodynamics. *Experiments in Fluids*, 58(9):1–10, 2017. ISSN 07234864. doi: 10.1007/s00348-017-2411-1.
- [78] S. von Hoesslin, J. Gruendmayer, A. Zeisberger, M. S. Sommer, J. Klimesch, S. Behre, H. Brandies, and C. J. Kähler. Visualization of laminarturbulent transition on rotating turbine blades. *Experiments in Fluids*, 61(6):1–10, 2020. ISSN 14321114. doi: 10.1007/s00348-020-02985-9.
- [79] T. Von Karman and W. R. Sears. Airfoil Theory for Non-Uniform Motion. *Journal of the Aeronautical Sciences*, 5(10), 1938.
- [80] J. H. Watmuff. Evolution of a wave packet into vortex loops in a laminar separation bubble. *Journal of Fluid Mechanics*, 397:119–169, 1999.
- [81] A. Weiss, C. C. Wolf, K. Kaufmann, J. N. Braukmann, J. T. Heineck, and M. Raffel. Unsteady boundary-layer transition measurements and computations on a rotating blade under cyclic pitch conditions. *Experiments in Fluids*, 61(2):1–16, 2020. ISSN 14321114. doi: 10.1007/s00348-020-2899-7.
- [82] F. M. White. *Viscous Fluid Flow*. McGraw-Hill Book Company, 3 edition, 2006.
- [83] B. Wieneke. *PIV Uncertainty Quantification and Beyond*. PhD thesis, TU Delft University, 2017.
- [84] C. C. Wolf, C. Mertens, A. D. Gardner, C. Dollinger, and A. Fischer. Optimization of differential infrared thermography for unsteady boundary layer transition measurement. *Experiments in Fluids*, 60(1):1–13, 2019. ISSN 07234864. doi: 10.1007/s00348-018-2667-0.
- [85] C. C. Wolf, A. D. Gardner, and M. Raffel. Infrared thermography for boundary layer transition measurements. *Measurement Science and Technology*, 2020.
- [86] D. W. Wynnchuk and S. Yarusevych. Characterization of laminar separation bubbles using infrared thermography. *AIAA Journal*, 58(7):2831–2843, 2020. ISSN 00011452. doi: 10.2514/1.J059160.
- [87] S. Yarusevych, P. E. Sullivan, and J. G. Kawall. On vortex shedding from an airfoil in low-Reynolds-number flows. *Journal of Fluid Mechanics*, 632:245–271, 2009. ISSN 00221120. doi: 10.1017/S0022112009007058.

- 
- [88] S. Zhong. Detection of flow separation and reattachment using shear-sensitive liquid crystals. *Experiments in Fluids*, 32:667–673, 2002. doi: 10.1007/s00348-002-0409-8.
- [89] S. Zuccher and W. S. Saric. Infrared thermography investigations in transitional supersonic boundary layers. *Experiments in Fluids*, 44(1):145–157, 2008. ISSN 07234864. doi: 10.1007/s00348-007-0384-1.